



Dissertation

Beam Loss Calibration Studies for High Energy Proton Accelerators

ausgeführt zum Zwecke der Erlangung des akademischen Grades eines Doktors der
technischen Wissenschaften unter der Leitung von

Univ.Doz. Univ.Prof. Dr. Dipl.-Ing. Christian W. Fabjan
Atominstitut der Österreichischen Universitäten (E141)

eingereicht an der Technischen Universität Wien
Technisch-Naturwissenschaftliche Fakultät

von

Dipl.-Ing. Markus Stockner

Matrikelnummer 9625285
Schwarzenberg 50
3341 Ybbsitz

Diese Arbeit wurde unterstützt vom Österreichischen Bundesministerium für
Wissenschaft und Forschung.

Genf, Oktober 2007

Begutachter

Technische Universität Wien, Atominstitut der Österreichischen Universitäten (E 141)

Univ.Doz. Univ.Prof. Dr. Dipl.-Ing. Christian W. Fabjan

Technische Universität Wien, Institut für Festkörperphysik (E 138)

Ao.Univ.Prof. Dipl.-Ing. Dr.techn. Michael Mantler

Kurzfassung

CERN's nächster Beschleuniger ist der Large Hadron Collider (LHC) mit einer Injektionsenergie von 450 GeV und einer Kollisionsenergie von 7 TeV. Die Teilchen werden von supraleitenden Magneten auf zwei gegenläufigen Umlaufbahnen gehalten, welche sich in den Interaktionspunkten kreuzen. Die komplexen Magneten beinhalten beide Strahlrohre in einem Joch, innerhalb eines Kryostaten. Eine noch nie dagewesene Energie wird in den umlaufenden Strahlen und im Magnetsystem gespeichert. Der LHC übertrifft existierende Beschleuniger in seiner maximalen Strahlenergie um den Faktor 7 und in der Strahlintensität um den Faktor 23.

Bereits ein kleiner Teil verloren gegangener Strahlteilchen kann zum Verlust der Supraleitung in den Spulen der Magneten oder zur Beschädigung von Komponenten führen. Die einzigartige Kombination von extremen Strahlparametern und die hoch entwickelte, supraleitende Technologie machen es notwendig im Hinblick auf existierende Beschleuniger, ein effizienteres Strahlkonservierungssystem und ein empfindlicheres Strahlverlustmesssystem einzusetzen. Es gibt deshalb mehrere Sicherheitssysteme um den Beschleuniger vor Schaden zu schützen.

Eines dieser Systeme ist das Beam Loss Monitoring System, welches verloren gegangene Teilchen detektiert und ihre Anzahl bestimmt. Bei überschreiten voreingestellter Verlustschwellen generiert das System ein Signal, damit der Strahl aus dem Beschleuniger extrahiert wird. Die in erster Linie verwendeten Detektoren sind Ionisationskammern. Etwa 4000 Stück werden im gesamten Beschleuniger installiert, die meisten davon im Bereich von Quadrupolmagneten. Die Detektoren messen außerhalb der Kryostate die Ausläufer von transversalen, hadronischen Schauern, welche von verloren gegangenen Strahlteilchen induziert werden. Die Anfangskalibrierung des Strahlverlustmesssystems soll gewährleisten, dass der systematische Fehler des Systems kleiner als 5 ist. Zur Kalibrierung des Systems und der Bestimmung der Verlustschwellen der Detektoren werden verschiedene Simulationen kombiniert:

Die Trajektorien von Strahlteilchen werden simuliert, um die wahrscheinlichsten Verlustpositionen zu bestimmen. An diesen Positionen werden die hadronischen Schauer in den Magneten simuliert, um die Energiedeposition in den Spulen der Magneten und die Energiedeposition in den Detektoren zu bestimmen.

Um bei Teilchenverlusten in einem kurzen Zeitintervall die maximal erlaubte Temperaturerhöhung der Magnetspulen zu bestimmen, bei welcher diese die Supraleitung verlieren, wird die Enthalpie der Kabel, das B-Feld und die Stromdichte in den Kabeln berücksichtigt. Für länger andauernde Teilchenverluste ist die maximal erlaubte Temperaturerhöhung durch den Wärmefluss im Helium und im Kupfer der Kabel bestimmt.

Diese Arbeit beschäftigt sich mit der Wirkungsweise und der Beschreibung von Strahlverlusten und dem korrespondierenden Signal in den Strahlverlust-Monitoren. Dieses Verständnis wurde mit dem Simulieren der Signale und dem Vergleich zu Messserien erzielt. Dabei wurden die Detektoransprechfunktionen simuliert, welche einen grundlegenden Bestandteil der Systemkalibrierung

darstellen. Ein weiterer wichtiger Punkt war die Bestimmung von auftretenden Ungenauigkeiten beim Simulieren von transversalen hadronischen Schauern, welche Teil des Systemkalibrierungsfehlers sind.

Die Detektoransprechfunktionen wurden mit dem Monte Carlo Programm Geant4 für verschiedene Teilchenarten bei verschiedenen Teilchenenergien simuliert. Validierungsmessungen wurden am CERN mit Protonen, Gamma Strahlen und in gemischten Strahlungsfeldern durchgeführt. Mit Neutronen wurden die Ionisationskammern im "The Svedberg Laboratory" kalibriert. Der interne Protonen "Beam Dump" von HERA diente als Teststand für das gesamte LHC BLM System. Über einen Zeitraum von zwei Jahren wurde das gesamte System unter realen Beschleunigerbedingungen getestet. Dies führte zu mehreren Verbesserungen der Hard- und Software. Die parasitischen Messungen von Protonen indizierten transversalen, hadronischen Schauern, wurden mit Geant4 Simulationen verglichen.

Im abschließenden Teil wurden die entwickelten Methoden verwendet, um eine Verlustschwelle eines LHC BLM Detektors zu bestimmen. Die berechneten Werte wurden mit früher bestimmten Werten verglichen.

Abstract

CERN's Large Hadron Collider (LHC) is a proton collider with injection energy of 450 GeV and collision energy of 7 TeV. Superconducting magnets keep the particles circulating in two counter rotating beams, which cross each other at the Interaction Points (IP). Those complex magnets have been designed to contain both beams in one yoke within a cryostat. An unprecedented amount of energy will be stored in the circulating beams and in the magnet system. The LHC outperforms other existing accelerators in its maximum beam energy by a factor of 7 and in its beam intensity by a factor of 23.

Even a loss of a small fraction of the beam particles may cause the transition from the superconducting to the normal conducting state of the coil or cause physical damage to machine components. The unique combination of these extreme beam parameters and the highly advanced superconducting technology has the consequence that the LHC needs a more efficient beam cleaning and beam loss measurement system than previous accelerators. There are several safety systems to protect the accelerator components from damage.

One of them is the Beam Loss Monitoring (BLM) system that detects and quantifies the amount of lost beam particles. It generates a beam abort trigger when the losses exceed predetermined threshold values. The principal detector type is an ionisation chamber. About 4000 detectors are being installed, mostly around the quadrupole magnets. The detectors probe the transverse tails of the hadronic showers emerging from the cryostat, which are induced by lost beam particles. The initial calibration of the BLM system should ensure that the systematic error of the system is smaller than 5. For the calibration and threshold determination several simulations are combined:

Beam particles are tracked to find the most probable loss locations. At these locations hadronic showers through the machine components are simulated to determine the energy distribution in the coil of the magnet and the total energy deposition in the BLM detectors.

To calculate the quench limits for short duration losses the enthalpy, the B-field and the current density in the cables is taken into account to estimate the maximal possible temperature increase. For steady state losses a possible temperature increase is mainly determined by the heat flow in the helium and in the copper of the cable.

This work focuses on the effectiveness and the characterisation of the particle losses and the corresponding detector signals. Simulating the signals and comparing those to several irradiation scenarios obtained this understanding. In the process the detector response simulations were performed, which form part of the system calibration, and the uncertainty estimation of transverse hadronic shower tail simulations were conducted, which contributes to the system calibration error.

The ionisation detector response functions were simulated utilising the Monte Carlo program Geant4 for different particle types at various kinetic energies. Validation measurements have

been performed at CERN with proton beams, gamma sources as well as in mixed radiation fields and at The Svedberg Laboratory (Sweden) the detector was calibrated with neutrons. The HERA internal proton beam dump served as a test bed for the LHC BLM system. Over a period of two years the whole BLM system was tested under real accelerator conditions, which resulted in several updates and upgrades of the hardware and software. The parasitic measurements of the tails of the hadronic showers induced by the impacting protons were compared to Geant4 simulations.

The final task was to utilise the gained methods to calculate an LHC BLM detector threshold, which was compared to previously, estimated thresholds.

Acknowledgements

First of all I would like to thank my doctoral thesis advisor Prof. Christian Fabjan for providing me with the unique opportunity to undertake my PhD at CERN and for his wise guidance and experience throughout these past three years.

Sincere thanks to my CERN supervisors, Eva Barbara Holzer and Bernd Dehning for their help and commitment during my time at CERN. Their support and guidance was invaluable.

Many thanks to the beam loss monitoring team, Bernd, Barbara, Christos, Claudine, Ewald, Gianfranco, Gianluca, Jan, Jonathan, Laurette, Michael, Raymond, Roman, Stian and Virginia for making me feel welcome in their midst and for their continuous support whilst carrying out my work and of course for the fruitful discussions during coffee.

Special thanks to my office colleagues, Daniel Kramer, Dariusz Bocian and Mariusz Sapinski for their huge support and encouragement.

I am pleased to have the opportunity here to thank my colleagues from DESY, firstly Kay Wittenburg for his support during the past two years while carrying out the experiments at HERA's proton beam dump. In this spirit I would also like to thank Ferdinand Willeke, Michael Bieler, Philip Duval, Bernhard Holzer, Peter Schmid, Michael Schmitz, Ruediger Schmitz, and Josef Wilgen.

I would also like to thank Roderik Bruce for his assistance in providing me simulation results.

For checking most of my English a great "thanks" to Richard Ecclestone and James Lamb who sacrificed their spare time.

The past three years have been an amazing experience. I am very grateful to have met so many interesting people, from the people in the Austrian community with whom I never felt very far away from home, to the climbers coaching me to overcome the steepest of rock faces.

Last but not least, a very special thanks and gratitude go to my parents and my brothers for always believing in me and for their moral encouragement.

Abbreviations

ADC Analog Digital Converter

BLM Beam Loss Monitoring

CERF CERN-EU High Energy Reference Field Facility

CERN European Organisation for Nuclear Research

CFC Current to Frequency Converter

DAB Data Acquisition Board

DESY Deutsche Elektronen-Synchrotron (Hamburg)

FPGA Field Programmable Gate Array

FTFP Fritiof + Precompound (Geant4 physics list)

GEANT4 GEometry ANd Tracking (Monte Carlo code)

HERA DESY's former hadron lepton collider

H6 CERF target area at the North Area (CERN)

KEK High energy accelerator research organization (Japan)

KERMA Kinetic Energy Released in MAtter

LHC Large Hadron Collider

LHEP Low High Energy Parametrised (Geant4 physics list)

PIC Ionisation chamber at CERF for beam intensity measurements

QGSP-BERT-HP Quark Gluon String + Precompound + Bertini-type cascade + High Precision Neutron (Geant4 physics list)

SC-RP Calibration Laboratory for Radiation Protection Instruments (CERN)

SPS Super Proton Synchrotron (CERN)

TSL The Svedberg Laboratory, at Uppsala University (Sweden)

T2 SPS extraction line to the North Area (CERN)

Contents

Abstract	v
Acknowledgements	vii
Introduction	1
1 CERN - European Organisation for Nuclear Research	3
1.1 The Accelerator Complex	4
1.2 The Large Hadron Collider	5
1.3 Machine Protection	6
1.3.1 Beam Loss Monitoring System	7
2 LHC Beam Loss Monitoring System	9
2.1 Beam Loss Detectors	10
2.2 Overview of the BLM Electronics	12
2.2.1 Successive Running Sums	14
2.3 Parameters for the HERA Dump Experiment	14
3 Principles of Ionisation Detectors	15
3.1 Gaseous Detectors	15
3.2 Ionisation Chamber	16
3.3 Ionisation by Charged Particles	17
3.3.1 Energy Loss by Heavy Charged Particles	17
3.3.2 Average Energy Required to Produce an Electron-Ion Pair	18
3.3.3 Detector Gas	18
3.3.4 Diffusion and Recombination	19
3.3.5 Charge Mobility	20
4 Monte Carlo Simulation Methods	21
4.1 Geant4	22
4.1.1 Application Development	22
4.1.2 Geant4 - Hadronic Models	22

4.1.3	Geant4 - Physics Lists	23
4.1.4	Production Thresholds - Range Cut-Off Value	24
5	Ionisation Chamber Response Simulations and Measurements	25
5.1	Introduction	25
5.2	Simulation Details	25
5.2.1	Detector Geometry and Sensitive Volume	26
5.2.2	Readout and Analysis	27
5.2.3	Statistical Error Calculation	27
5.2.4	Estimation of Systematic Errors	27
5.3	Detector Response	32
5.3.1	Response Functions for various Particle Types	32
5.4	Validation Measurements	37
5.4.1	400 GeV Proton Beam Measurement	37
5.4.2	662 keV Gamma Ray Measurement	42
5.4.3	174 MeV Neutron Measurement	44
5.4.4	Mixed Radiation Field Measurement	54
5.5	Summary	65
6	Error Estimation on Hadronic Shower Tail Simulations and Measurements	66
6.1	Introduction	66
6.2	The HERA Proton Beam Dump	67
6.3	HERA Proton Beam Dump Measurements	69
6.3.1	Beam Parameter and Impact Position	70
6.3.2	Data Acquisition System	72
6.3.3	Calibration of the Electronics	72
6.3.4	Data Acquisition and Data Analysis	73
6.3.5	First-order Recombination Loss Correction	75
6.3.6	Space Charge Effect Correction	77
6.3.7	Measurement Results	78
6.4	HERA Proton Beam Dump Simulations	81
6.4.1	Description of the Simulation	82
6.4.2	Estimation of Required Primary Proton Number	84
6.4.3	Comparison of Spectra	84
6.4.4	Escape Angle and Longitudinal Secondary Shower Profile	88
6.4.5	Energy Deposition per Primary Proton	89
6.4.6	Simulation Results	90
6.4.7	Validation with the Combined-Simulation	93
6.4.8	Validation with Folding-Method	93

6.5	Comparison of Measurements and Simulations	95
6.6	Summary	98
7	Estimation of an LHC BLM Detector Threshold	100
7.1	Long Straight Section Magnet Simulation	101
7.2	Detector Response Generation	103
7.3	Quench Limits	105
7.4	Calculation of the Detector Threshold	107
7.5	Summary	109
8	Conclusions	110
	Bibliography	114
A	Explanatory Notes	118
A.1	(Nuclear) Interaction Length	118
A.2	SPS Electronics - Charge Integrator	119
A.3	Dose Rate to Fluence Conversion	119
A.4	Binning of a Spectrum	121
A.5	Numbers and Conversion Factors for the SPS BLM Detector	122
A.6	Simulated HERA Dump Spectra	122
B	Statistics and the Treatment of Experimental Data	129
B.1	Distribution Moments. The Mean and Variance	129
B.2	Measurement Errors: Systematic and Random Errors	130
B.2.1	Systematic Errors	130
B.2.2	Random Error	130
B.3	Sampling	131
B.3.1	Sample Moments	131
	Appendices	118
C	LHC BLM Detector Layout	133
D	SPS BLM Detector Layout	135

Introduction

The Large Hadron Collider (LHC) is the next circular accelerator currently under construction at the European Organisation for Nuclear Research (CERN). The collider will accelerate protons and ions up to unique 7 TeV per charge in two circulating beams which cross each other in the four main LHC experiments. The head-on collisions will provide a deeper understanding and new discoveries in high-energy particle physics. The LHC is being installed in the 27 km long LEP tunnel. In order to obtain the required magnetic field strength to guide the particles, superconducting magnets, cooled with superfluid helium, are utilised.

The energy stored in the LHC has the potential to damage or even destroy machine components. In the magnet system up to 10 GJ are stored. This energy has to be dissipated in a safe way if a magnet undergoes a transition from the superconducting to the normal conducting state. This transition is usually referred to as magnet quench. Furthermore, each circulating beam stores more than 360 MJ. Even a loss of only a very small fraction of the circulating particles can cause quenches or damage by depositing energy in the equipment. This will either warm the magnet's coil resulting in a down time of the accelerator for a few hours to cool and refill the machine, or cause a severe failure which leads to several months of repair. To prevent and protect the accelerator, safety systems like the beam loss monitoring system have been provisioned.

The aim of this thesis is the calibration the beam loss detectors, the verification of hadronic shower tail simulations and the estimation of a beam loss monitor threshold. The work was performed within CERN's beam instrumentation group and more specifically in the section providing the protection and monitoring system from beam losses.

The thesis starts with a general introduction to LHC and its protection systems.

In chapter two the beam loss monitoring system is presented and the parts covered and included in this thesis are pointed out.

An introduction to gaseous detectors and more specific to ionisation chambers is given in the third chapter. It includes a short introduction to the interaction of particles with matter.

The simulations presented in this work were performed with the Geant4 software package. An overview of Geant4 and the utilised physics lists is conducted in chapter four.

The beam loss monitors in the LHC are mounted mainly outside of the magnet's cryostates. There, they measure the secondary particle showers generated by the lost beam particles passing through the magnets. If the detector signal exceeds specified thresholds, the system inhibits the beam permit signal, which triggers a beam extraction. The generated particle showers vary strongly in particle composition and energies, which points out the importance of calibrating the BLM detectors to different particle types at various energies.

The detector response simulations performed with Geant4, the verification calculations and validation measurements conducted at several institutes are presented in chapter five. Systematic uncertainties deriving from the simulations are estimated. The final results from the detector calibration are the so-called detector response functions for different particle types at various energies.

The sixth part is dedicated to the error estimation of hadronic shower tail measurements and simulations. A full LHC BLM system was installed at the HERA proton beam dump. The system was continuously acquiring data in the past 2 years without any major interruption. This long-term test led to several updates and upgrades of the hardware and software. Six ionisation chambers of SPS type beam loss monitors were installed on the absorber with a spacing of about 1 m in beam direction to measure the lateral shower profile along the dump. Monte Carlo simulations are performed and compared to the measurements. Different physics lists are applied and the differences in their spectra and detector signals are discussed. There will be about 4000 BLM ionisation detectors installed around the LHC, each one with its individually adjusted threshold. The introduced Folding-Method, to simplify and accelerate the calculation of these thresholds, is presented and compared to two equivalent, but more time-consuming, approaches. The Folding-Method convolutes the detector response functions with particle fluence spectra to generate a relative detector signal. Finally, a recommendation for a physics list in Geant4 to simulate the hadronic showers is given.

Chapter seven is devoted to the estimation of an LHC Beam Loss Monitoring detector threshold. Simulations of an MQY LHC quadrupole magnet were performed by members of the BLM section to score the energy deposition in the magnet's coil and to derive the particle spectra outside the magnet. From the maximum energy deposition in the coils per cubic centimetre and the magnet specific quench limit the maximum allowed number of lost beam protons is derived. Utilising the Folding-Method, the relative detector signal is generated which is scaled with the derived maximum allowed number of lost protons to obtain a first LHC BLM detector threshold.

In the appendix, the reader can find conversion calculations from dose to particle flux, a table of conversion factors between several units, a description of the plotting of particle fluence spectra in lethargy utilised in this work and a short introduction to statistical error calculation.

Chapter 1

CERN - European Organisation for Nuclear Research

CERN, the European Organisation for Nuclear Research, is the world's largest and most influential particle physics centre. The laboratory was founded in 1954 and is one of Europe's first joint ventures. It has become a shining example of international collaboration. From the original 12 signatories of the CERN convention, membership has grown to the present 20 Member States. The research centre sits astride the Franco-Swiss border near Geneva at the foot of the Jura mountains.

CERN is a laboratory where scientists unite to study the building blocks of matter and the forces that hold them together. CERN primarily exists to provide research facilities with the necessary tools to the scientists. These are accelerators, which accelerate particles to almost the speed of light and detectors that make the particles visible.

The history of CERN is strongly connected to the construction of accelerators. In 1957 the Synchro-Cyclotron (SC) and in 1959 the Proton Synchrotron (PS) were built. These were followed by, the Intersecting Storage Rings (ISR) in 1971, the Proton Synchrotron Booster (PSB) in 1972 and the Super Proton Synchrotron (SPS) in 1976. Running the SPS as a proton-antiproton collider allowed in 1983 the Noble prize worthy discovery of the W-bosons and the Z-boson. These are the carriers of the weak nuclear force, thus confirming the electro-weak theory, which unifies weak and electromagnetic forces. In 1989 the Large Electron-Positron storage ring (LEP), installed in a 27 km long tunnel 100 m below the surface, started operation. Until LEP stopped running end of 2000 several fundamental parameters of the Standard Model were confirmed to an extraordinary degree of precision. In 1994 the construction of the Large Hadron Collider (LHC) was approved by the council. CERN's Antiproton Decelerator (AD) facility announced the first controlled production of large quantities of antihydrogen atoms at low energies in 2002. The installation start of the LHC in 2005 is marked by lowering the first of the 1232 superconducting dipole magnets into the emptied LEP tunnel. The LHC represents the next step in high-energy physics research in a worldwide collaboration. It will be the first storage ring in which quarks and gluons collide in the TeV energy range.

CERN Accelerator Complex

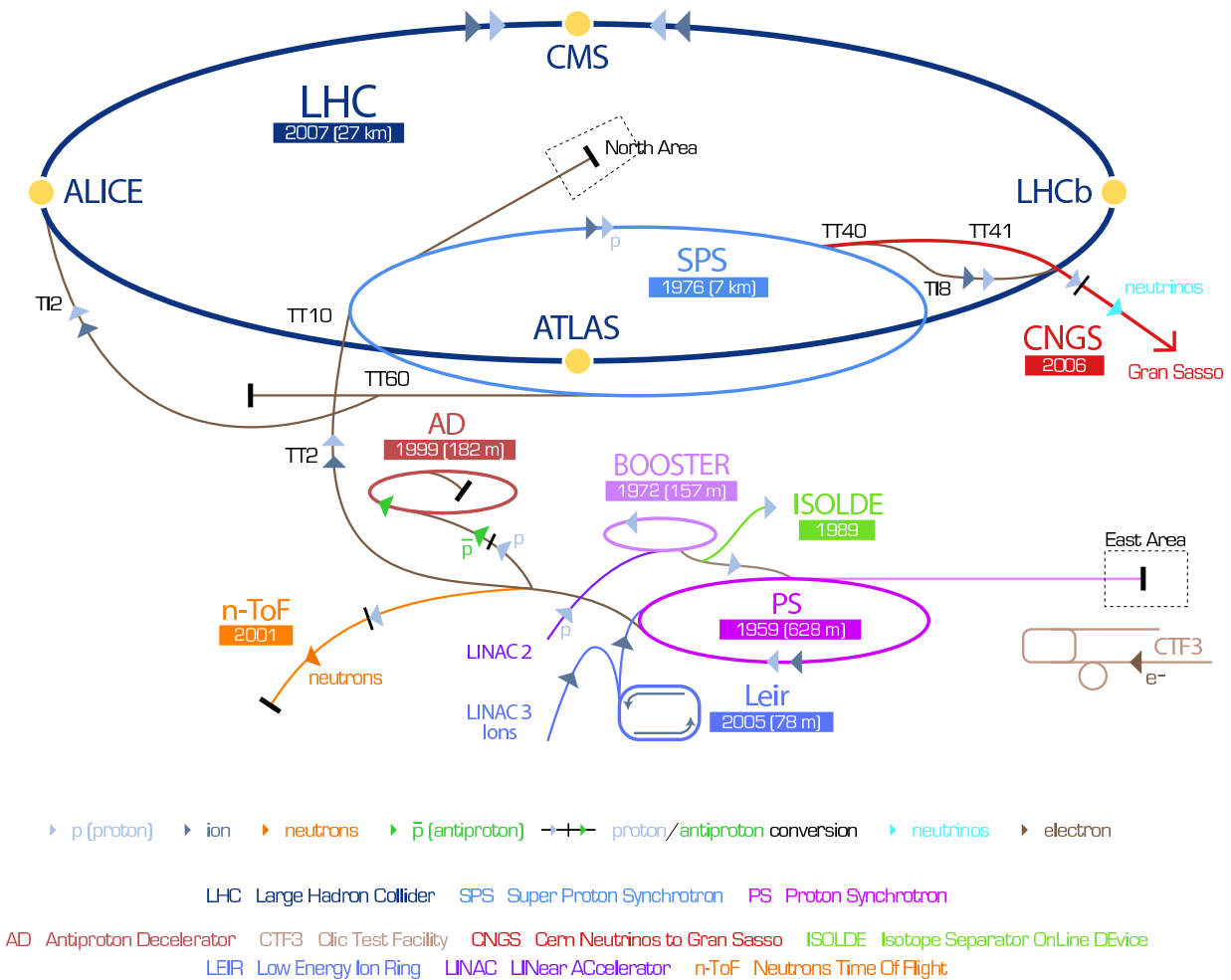


Figure 1.1: CERN’s accelerator complex with the four main LHC experiments, ATLAS, CMS, ALICE and LHCb [1].

1.1 The Accelerator Complex

CERN’s accelerator complex is versatile, including accelerators and colliders for various energies and particle types which are electrons, protons, antiprotons, ”heavy ions” (oxygen, sulphur, lead) and even neutrino production is conducted. Figure 1.1 provides an overview of the existing accelerators and the locations of the experimental areas. The two counter rotating beams in LHC [2] cross each other at the Interaction Points (IP) at which enormous high performance experiments are located in underground caverns tracking debris from collisions. There are two general-purpose proton-proton experiments, ATLAS (A Toroidal LHC ApparatuS, IP1)[3] and CMS (Compact Muon Solenoid, IP5)[4] and two specialised experiments, ALICE (A Large Ion Collider Experiment, IP2)[5] and LHCb (IP8)[6]. ATLAS and CMS are designed to accomplish the Higgs search for any predicted Higgs mass. ALICE is dedicated to study physics of strongly interacting matter at extreme energy densities by heavy-ion collisions (Pb-Pb). LHCb is designed to fully exploit the B-physics potential of the LHC.

The accelerator chain leading to LHC starts at the ion sources in-front of LINAC 2 (LINear

ACcelerator), which is dedicated to protons, and LINAC 3, dedicated to ions. The roughly 80 m long LINACs accelerate the particles to 50 MeV per charge and inject them to either PSB (Proton Synchrotron Booster) or LEIR (Low Energy Ions Ring). The protons or ions are consecutively accelerated and injected to the next larger accelerator. The PSB with a circumference of about 157 m increases the energy of the protons up to 1.4 GeV and injects them into the the PS (Proton Synchrotron). The PS with a circumference of 628 m increases the energy up to 26 GeV and creates the final LHC bunch structure of 25 ns. The further acceleration is performed with the SPS (Super Proton Synchrotron, circumference of 7 km) up to the injection energy of 450 GeV for LHC. Both rings of the LHC are filled from the SPS via the injection lines TI2 and TI8 with each three bunch trains corresponding to a total of 2808 bunches. The LHC with a circumference of 27 km accelerates the particles up to 7 TeV per charge. The start-up of LHC is foreseen in spring 2008.

1.2 The Large Hadron Collider

The main actual project at CERN is the Large Hadron Collider. It will provide proton-proton collisions at 7 TeV. At nominal conditions the protons have a revolution frequency of 11.246 kHz which corresponds to the revolution time of $88.9 \mu\text{s}$. The bunches are spaced by 25 ns and have a length of 1.12 ns (4σ). Each ring is filled with 2808 bunches with an intensity per bunch of $1.1 \cdot 10^{11}$ protons. The potential to discover new physics with a collider is proportional to the event rate R at which particles are produced. It results from the multiplication of the particle cross section σ_{int} which is a measure for the interaction probability, with the accelerator parameter, luminosity \mathcal{L} :

$$R = \mathcal{L} \cdot \sigma_{int} \quad (1.1)$$

The luminosity describes the particle beam characteristics and is approximated as:

$$\mathcal{L} = f \frac{n_1 \cdot n_2}{4\pi \cdot \sigma_x \cdot \sigma_y} \quad (1.2)$$

where n_1 is the number of particles in a bunch of beam 1 and n_2 is the number of particles in a bunch of beam 2, f is the bunch crossing frequency and σ_x and σ_y characterise the Gaussian transverse beam profile [7].

The luminosity of the LHC will reach at nominal conditions $10^{34} \text{ cm}^{-2}\text{s}^{-1}$. LHC will surpass comparable machines in energy by a factor of 7, in luminosity by a factor of 100 and in beam intensity by a factor of 23.

To keep the beam particles on their orbit in the 27 km long accelerator magnets, made from superconducting NbTi are needed to generate a magnetic field strength of up to 8.3 Tesla. This corresponds to a magnet current of about 12 kA. The magnets are cooled with liquid Helium at 1.9 K and 4.5 K, depending on the type. The total amount of energy stored in the magnetic system is about 10 GJ [8].

Critical procedures in the operation of the LHC are the injection and the ramping of the beam energy. Losses of beam particles within one revolution period are likely in these stages which introduce additional damage risk to the equipment. At high energy and stable beam conditions the two beams are brought into collision. While the bunches are inside the experiments their constituents are influenced by bunch-bunch effects, some are deflected and a small amount of the particles collides head-on and generates the wanted events in the detectors. All these effects

and non-linearities in the machine may add up after several revolutions and particles gain such large motion amplitudes that they reach an aperture limit. A large number of these particles ($4 \cdot 10^9$ protons per second, at nominal conditions) are absorbed at foreseen aperture limits, the collimators. Losses at other machine parts cannot be avoided in ideal operation, which can lead to severe damage of machine components. And equipment failure may result in dangerous, possibly fast enduring losses.

A most probable loss location is the range between the beginning to the middle of a quadrupole magnet. Here, the beam pipe diameter changes and the beam size increases. The lost beam particles lead to an energy deposition in the cold magnets and heat up the coil. At a certain limit a quench occurs, parts of the superconducting coil will undergo a transition from the superconducting state to the normal conducting state. An energy deposition in the order of a few mJ/cm^3 is sufficient to initiate a quench [9]. A quench will lead to an interruption of the accelerator operation and in the worst case to a destruction of a magnet, which results to a down time from a few hours to several months. To prevent this, the LHC needs a more efficient beam cleaning system and a more precise beam loss measurement system than existing accelerators.

1.3 Machine Protection

The LHC combines large beam currents at high energy with a most advanced superconducting magnet technology. As a consequence, the need for a comprehensive protection system arises.

Depending on the loss duration different protection measures become operative. There are beam loss related protection systems; the quench protection, the beam interlock system and the beam dump system. Further information to all systems can be found in [10].

Losses occurring within a single revolution, $89 \mu\text{s}$, are referred to as ultra fast losses. The protection relies on the collimator system and beam absorbers. Very fast losses or multi-turn losses occur in less than 5 ms. Here, only the BLM system can provide active machine protection at LHC start-up. Other systems with similar reaction time, like some monitors of the beam position monitoring system and the fast beam current decay monitoring system will most probably not be operational for this purpose at the LHC start-up. Losses over more than 5 ms are called fast losses. In this regime the beam loss detectors around the machine, signals from equipment in case of hardware failure, fast beam current decay monitors and beam position monitors will be utilised to inhibit the beam permit signal resulting in a beam extraction. For loss durations longer than 10 ms the Quench Protection System (QPS) provides additional protection. Steady loss durations are in the order of seconds (one second or more). In the range of steady losses the measurement of the cryogenic temperature or the observed heat load at the collimators can trigger a beam abort [11].

Directly related to this work is the Beam Loss Monitoring (BLM) system. An overview of the BLM system is presented in the next sections and a more detailed description of the components follows in chapter 2.



Figure 1.2: Installation of the LHC BLM system detectors outside a quadrupole magnet.

1.3.1 Beam Loss Monitoring System

The LHC beam loss monitoring (BLM) system must provide the necessary information to prevent the super conducting magnets from quenching and to protect the machine components from damage [12].

The objective of the BLM system is to detect dangerous losses and generate a beam dump signal, which leads to a safe extraction of the beam onto the dedicated LHC beam dump. The system must not ignore dangerous losses and at the same time guarantee that no false alarms are generated. No beam should be injected to the LHC if the BLM system is not operational.

The system utilises two monitor types, the main type is an ionisation chamber. About 4000 of them will be installed around the ring. Figure 1.2 show the tunnel installation of three ionisation chambers outside a quadrupole cryostat. At special locations (e.g. collimator) a few hundred secondary emission monitors are installed. The lost beam particles initiate hadronic showers through the magnets and other machine components. These shower particles are measured by the monitors installed at the most probable loss locations on the outside of the accelerator equipment. The detector signal is proportional to the intensity of the lost beam particles. This signal is digitised by a special radiation tolerant electronics located in the LHC tunnel. The transmission of the data is performed via a redundant fibre optical link to the surface. The measured detector signal is compared by a Data Acquisition Board (DAB) to predefined thresholds values, which are depend on the beam energy and the loss duration. If the signal exceeds the threshold, the DAB card revokes the beam permit signal given to the combiner card. The combiner card forwards the beam dump request to the LHC Beam Interlock System.

The start-up calibration of the BLM system is required to have an accuracy within a factor of 5, and a final accuracy within a factor of 2. For the calibration and threshold determination a number

of simulations are combined. Tracking studies to derive the most probable loss locations are conducted. At these locations hadronic showers through the machine components are simulated. The shower simulations generate the particle spectra outside the magnet at the detector locations and score the deposited energy in the magnet's coil. Different simulations of the detector yield the detector response functions. The quench levels of the superconducting magnets, according to loss duration and beam energy, are simulated separately. Whenever possible, cross-checks with measurements have been performed or are planned before the start-up of the LHC, e.g. beam tests with the BLM detectors, real LHC magnet quench tests, irradiation of the radiation tolerant electronics, reliability investigations of the whole system.

Chapter 2

LHC Beam Loss Monitoring System

The Beam Loss Monitors are utilised to measure and localise beam losses around the accelerator. In case of the detection of a seriously dangerous loss the Beam Loss Monitoring (BLM) system will inhibit the beam permit, which results in a beam dump. During a beam dump a safe extraction of the beam particles to the designated location, the LHC beam dump, occurs.

The system can be divided regionally into an installation in the underground tunnel and in the surface buildings. An overview of the separate parts is shown in Figure 2.1.

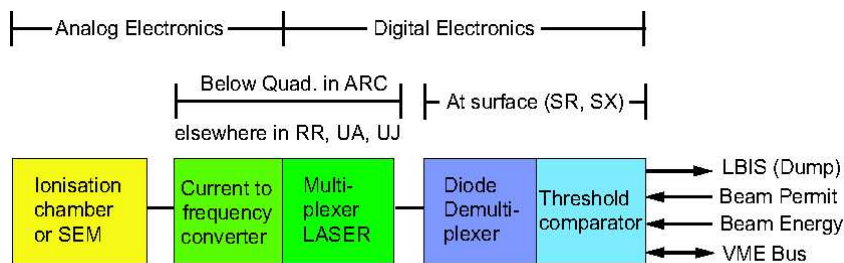


Figure 2.1: Layout of the LHC BLM electronic.

About 4000 ionisation chambers will be installed around the ring. A set of eight detectors can be connected to one of the tunnel cards. The tunnel cards (BLMCFCs) utilise a Current to Frequency Converter (CFC) [13] and an Analogue to Digital Converter (ADC) to digitise the detector signal. The digitised data is acquired by a Field Programmable Gate Array (FPGA) device, which forwards the data by an fibre optical link to the surface. The data analysis modules (BLMTC) at the surface receive the data.

The BLMTC card comprises also a FPGA, which analyses the data by keeping a history of those in memory. It compares the digitised detector signals to predefined threshold values and requests a beam dump if they are exceeded. Each surface card receives data from two BLMCFC cards and is therefore able to treat 16 channels simultaneously. VME crates that include a combiner card house the BLMTC cards. The combiner cards manage the transmission of the beam dump requests and distribute the information of the actual beam energy level to the BLMTC cards [14].

2.1 Beam Loss Detectors

At the end of 2004 the design of the LHC BLM detector was finalised and the production started in 2005. Therefore, most of the measurements performed within this work are conducted with SPS ionisation chambers. These ionisation detectors are similar in design to the LHC detector. The detectors are shown in Figure 2.2. A comparison of the detector properties is shown in Table 2.1.



Figure 2.2: Picture of the LHC and the SPS BLM detectors without the cover tube. Left: LHC BLM detector. Right: SPS BLM detector.

The main detector type for the LHC BLM system is a parallel plate ionisation chambers. In regions with higher beam loss additional Secondary Emission Monitors (SEM) are foreseen.

Both ionisation detectors are made of a stainless steel tube with a wall thickness of 2 mm. They include a pile of 61 and 31 parallel aluminium electrodes for the LHC and the SPS BLM, respectively. The LHC BLM electrodes have a thickness of 0.5 mm, a diameter of 75 mm and are equally spaced by 5.75 mm. The SPS BLM electrodes have a diameter of 93 mm and have, the same thickness of 0.5 mm and, the same spacing of 5.75 mm. The cover plate on the side to the electrical connections has a thickness of 4 mm, the opposite plate is 5 mm thick in the case of the LHC BLM detector. The cover plate towards the electronics box in the SPS BLM detector has as thickness of 8 mm and the opposite plate is 5 mm thick. Six stainless steel rods, which are only in the SPS BLM detector covered by aluminium spacers, hold the electrodes in place. These rods are fixed by insulating ceramic pieces to the outer shell. A detailed drawing of the LHC BLM detector and the SPS BLM detector can be found in the appendix C.1 and appendix D.1, respectively. Both detectors are filled with nitrogen (N_2) at an overpressure of 100 mbar. This allows the detection of a leak during the planned annual inspection with a portable radiation source. The electrodes are alternately utilised as high voltage electrodes and signal electrodes. A bias voltage of up to 1.5 kV is applied to the electrodes. The only passive electronic components mounted to the feed-through of the detector are a resistor and a capacitor of a low pass filter. The filter smoothes bias voltage fluctuations and keeps the drift voltage nearly constant at the electrodes in case of a break down of the voltage power supply. Therefore, the operation of the detector is ensured for minutes after a switch off.

Table 2.1: Comparison of the design and standard operation parameters of the LHC and the SPS BLM detector. ^{a)} plate towards the electronics box.

detector properties	LHC BLM	SPS BLM
length	50 cm	26 cm
diameter	9 cm	11.4 cm
detector gas	N_2	N_2
pressure	1.1 bar	1.1 bar
sensitive volume length	38 cm	19 cm
number of electrodes	61	31
electrode spacing	5.75 mm	5.75 mm
electrode diameter	75 mm	93 mm
standard bias voltage	1500 V	800 V
wall thickness		
tube	2 mm	2 mm
bottom plate ^{a)}	4 mm	8 mm
top plate	5 mm	5 mm

On the same design as the ionisation chamber is the SEM detector based on. Instead of a gas filling the SEM vessel is under vacuum. Only three titanium electrodes are inside the stainless steel tube from which charged particles are liberated and measured [15]. The physical principle of particle detection is different to the ionisation chamber, which leads to a factor of approximately 20,000 less in sensitivity. A picture of the SEM detector is shown in Figure 2.3.

The LHC BLM ionisation detectors will be mounted in the horizontal plane of the two beam pipes outside of the LHC magnet cryostats. The LHC BLM SEM detectors are mounted additionally at special location, where high particle flux occurs, e.g. collimators. At this position the secondary particle flux is highest and the cross talk between the two beams is minimised.



Figure 2.3: Picture of the LHC BLM SEM detector without the cover tube.

From Monte Carlo simulations of the particle shower through the magnet the detector locations were determined [16]. It was shown that six detectors localised around a quadrupole magnet are sufficient to measure the beam losses and to distinguish the two beams. The interconnection of the detectors is shown in Figure 2.4. In Figure 1.2, LHC BLM detectors mounted outside of a quadrupole magnet, can be seen.

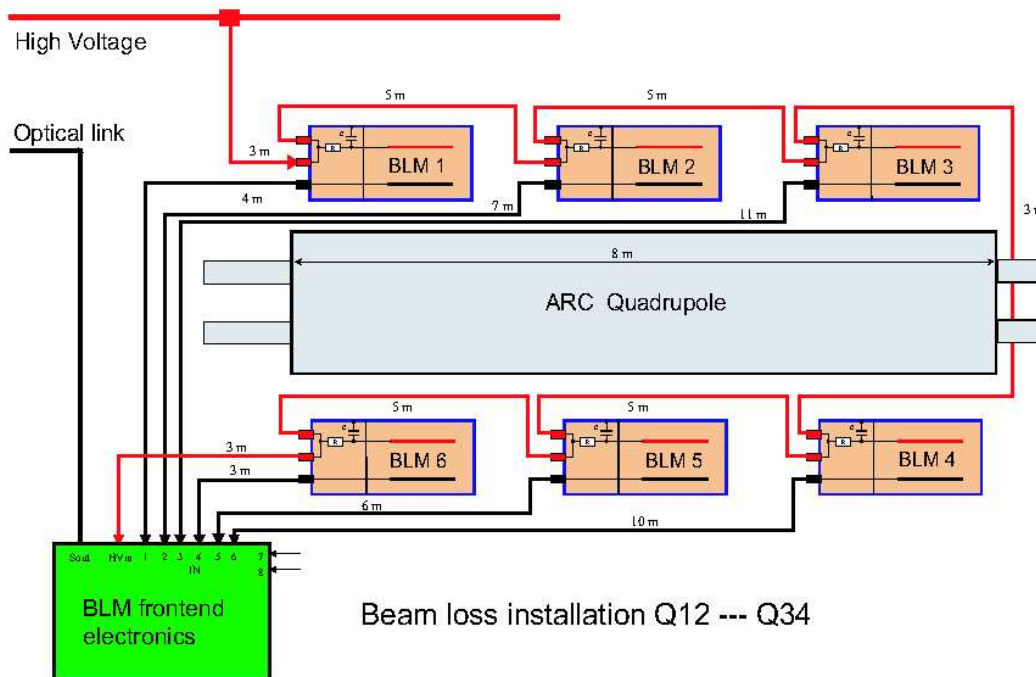


Figure 2.4: Schematic of the BLM detector installation. Six ionisation chambers are placed around a quadrupole magnet [12].

2.2 Overview of the BLM Electronics

The particle losses are measured in the analogue part of the front-end card, which is located in the LHC tunnel and are transmitted to the surface, where the final analysis is conducted. The measured detector signal is converted by a Current to Frequency Converter (CFC) which was designed to work on the principle of balanced charge and is shown in Figure 2.5 [14][17].

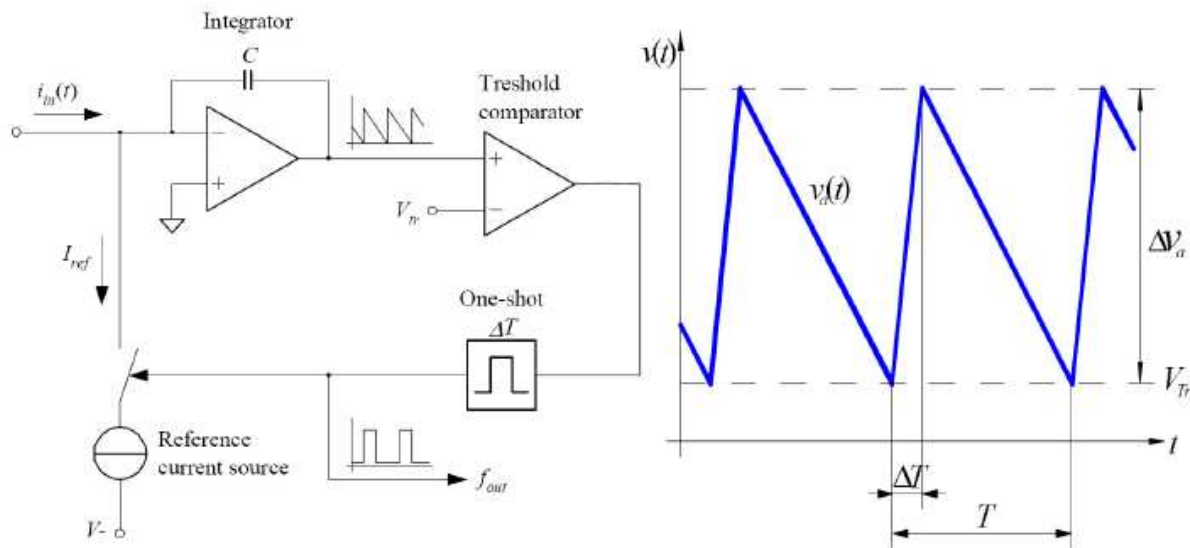


Figure 2.5: Working principle of the Current to Frequency Converter (CFC) [14].

During the period T , the current, induced by radiation, from the detector is integrated. If a constant signal is applied the integrator output ramps down with a constant slope. At the threshold level V_{Tr} the reference current I_{ref} is induced into the summing node of the operation amplifier for a fixed time period ΔT which resets the integrator output. The relation between the output frequency and the detector current is derived as: $f = \frac{i_{in}}{I_{ref}\Delta T}$. The CFC properties are plotted in Table 2.2.

Table 2.2: Properties of the Current to Frequency Converter (CFC).

Frequency	0.01- 5.0e6	Hz
Current	2.5 - 1.0e6	pA
Dynamic	5.00e8	
Resolution	200	pC/clock
Clock max	500	clock/ 0.1 ms

To extend the dynamic range of the CFC an ADC is implemented in the BLMCFC card with the intention to cover the range below one CFC count. This is needed to detect slow losses.

As mentioned, the signal processing is performed at the surface. The BLMTTC processing module is a VME card that provides the necessary processing power and includes the components for the optical link. The data sent from the tunnel includes an ADC and a counter value, which are merged in the BLMTTC card. The combined values are fed every $40 \mu\text{s}$ to the Successive Running Sums (SRS 2.2.1) which allows to keep a history of the detector data. Those sums are compared to the predefined threshold values in respect to the time interval and the beam energy. Once more if a threshold is exceeded the BLM system requests a beam dump. The analysed data is also transmitted to the LHC control room and to the logging system. The whole electronics design and the data analysis procedure is description in [14].

2.2.1 Successive Running Sums

A constantly updated window is kept by adding the newest incoming value to a register and subsequently subtracting the oldest value. The number of values kept in the window which correspond to a certain period in time define the integration time of the window. This window is called running sum.

Additionally are multiple moving windows cascaded to generate longer integration periods. This procedure minimises the utilised resources [14].

2.3 Parameters for the HERA Dump Experiment

Table 2.3 shows the running sums which were available for the measurement performed at the HERA proton beam dump. For each running sum the maximum of the last second is logged every second. The detector signal has due to filters in the acquisition chain a decay time of about 40 ms (τ). To integrate all charges produced in the detector one has to integrate over 5τ . Therefore, running sum number 9 which integrates over a period of 1.3s was chosen for the data analysis.

Table 2.3: Available Running Sums.

	Time windows		Refreshing	
	$40\mu\text{s}$ steps	ms	$40\mu\text{s}$ steps	ms
1	1	0.04	1	0.04
2	2	0.08	1	0.04
3	8	0.32	1	0.04
4	16	0.64	1	0.04
5	64	2.56	2	0.08
6	256	10.24	2	0.08
7	1024	40.96	64	2.56
8	4096	163.84	64	2.56
9	16384	655.36	1024	40.96
10	32768	1310.72	1024	40.96
11	65536	2621.44	1024	40.96
12	81920	3276.8	1024	40.96

Chapter 3

Principles of Ionisation Detectors

3.1 Gaseous Detectors

The main LHC Beam Loss Monitor (BLM) type is an ionisation chamber. The ionisation chambers are utilised to measure the fluence of charged particles. The charged particles ionise the nitrogen gas within the chamber. The liberated electrons and ions are collected at the electrodes due to an applied electric field. The induced current is proportional to the particle flux. It is important to operate the detector in its linear region. In chapter 6 measurements at the HERA proton dump are described. The ionisation rate for these measurements are at such high levels that non-linear effects start to develop. One of the effects was identified as space-charge effect, which builds up due to slow moving ions in the ionisation chamber. A theoretical description from literature is utilised to compensate for this non-trivial signal behaviour.

This chapter introduces the basic operation of ionisation chambers and gives a basic introduction to energy loss of charged particles in matter [18].

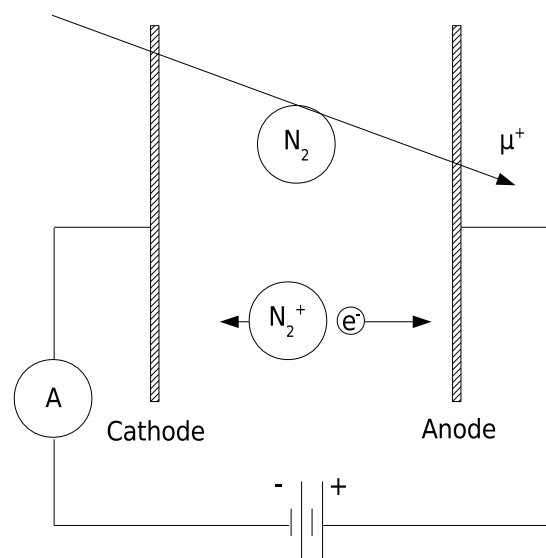


Figure 3.1: Schematic of an ionisation chamber.

3.2 Ionisation Chamber

In Figure 3.1 a parallel-plate ionisation chamber is illustrated. Between the electrodes an adjustable bias voltage is applied. The moving ionisation charges induce a signal current on the two electrodes. In the ideal ionisation chamber this would result in a measured current, which is proportional to the amount of charges liberated by energy deposition from a passing particle. A high-energy particle ionises per traversed length similar amounts of charges. Simply counting the charges liberated gives a measure of the number of traversing particles. However, different particle species may ionise different amount of charges per particle, which complicates the measurements. In section 3.3.1 the process by which the heavy charged particles produce charges in the chamber is described.

The electric field applied between the electrodes causes the electrons and ions to drift to the corresponding electrode as described in section 3.3.5. A conceptual plot of the ionisation chamber response variation with applied electric field is shown in Figure 3.2. The gain is defined as the ratio between measured charge to initially ionised charge. At low electric fields the charge drift will be slower and not all of the liberated charges will arrive at the electrodes, some of them will recombine in the gas or attach to gas molecules. The standard operation of an ionisation chamber is in the plateau region. All initially liberated charges are collected on the electrodes and variations of the applied field do not influence the level of detected charges. At higher fields the detector enters the proportional mode. The drift electrons gain enough kinetic energy from the electric field to ionise further neutral atoms in the gas. This leads to charge multiplication. The collected charge is proportional to the originally created number of electron-ion pairs. Increasing the applied voltage further can introduce non-linear effects. These effects mark the beginning of the limited proportional region. The induced current still increases with increasing number of initial electron-ion pairs, but no longer in a proportional way. At even higher bias voltages the detector enters the Geiger-Mueller area. In this area the proportionality between the number of originally created electron-ion pairs and the number of collected charges is no longer valid.

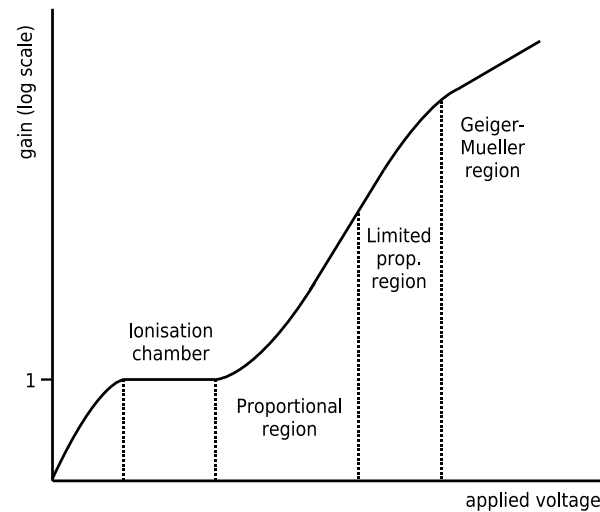


Figure 3.2: Different regions of operation of gas-filled detectors.

3.3 Ionisation by Charged Particles

This section gives a short introduction to the most relevant physics processes in gaseous detectors. The response of gaseous detectors is mainly based on the electromagnetic interaction. If a charged particle traverses matter it ionises the medium along its track. Secondary charged particles are generated, which can be measured within the gaseous detector. Depending on the particle also other processes are possible due to the strong and the weak interaction.

High-energy electrons mainly lose energy by bremsstrahlung. At low energies electrons primarily lose energy by ionisation.

Photons and neutrons cannot directly ionise the medium, as they do not carry charge. These particle types have to generate secondary charges by other processes to be measured. For photons physical processes like the photoelectric effect, Compton scattering and pair production can produce detectable charged particles. Neutrons undergo different interactions depending on their energy, e.g. elastic or inelastic nuclear collisions.

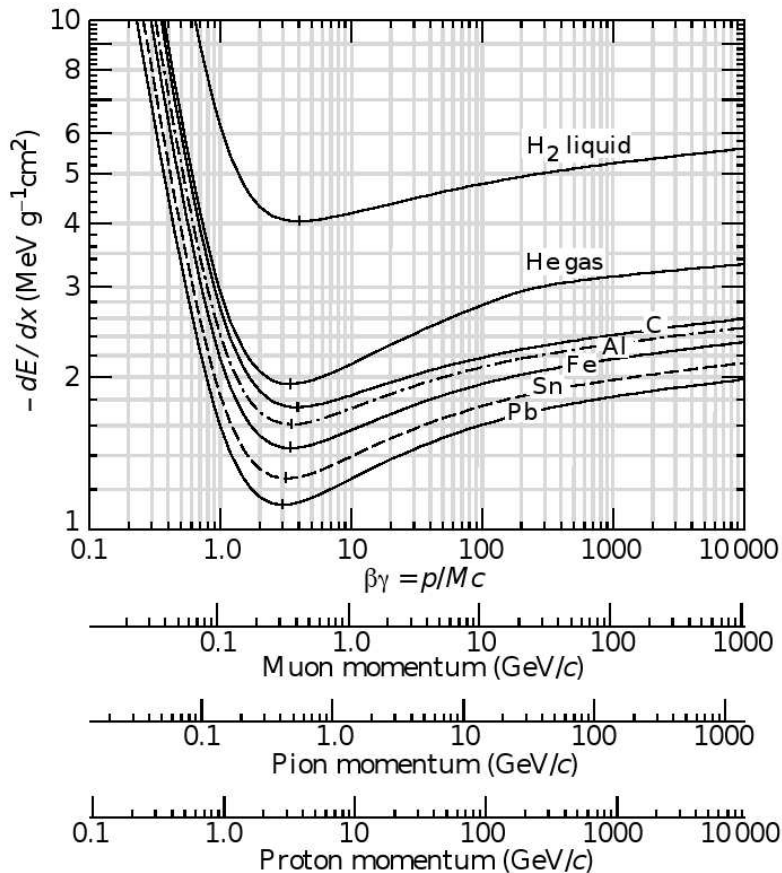


Figure 3.3: Average energy loss in different absorber materials [7].

3.3.1 Energy Loss by Heavy Charged Particles

Heavy ($m > m_e$) charged particles traversing matter lose energy by electromagnetic interaction which is a statistical process resulting from many discrete interactions. The particles are thereby

inelastically scattered on the atomic shell or the nuclei. Ionisation takes place if the transfer energy exceeds the binding energy of a shell electron. Otherwise, the energy deposition results in an excitation of the atoms. For heavy charged particles the Bethe-Bloch equation describes the average differential energy loss (or stopping power) per unit length as follows:

$$-\frac{dE}{dx} = Kz^2 \frac{Z}{A} \frac{1}{\beta^2} \left[\frac{1}{2} \ln \frac{2m_e c^2 \beta^2 \gamma^2 T_{max}}{I^2} - \beta^2 - \frac{\delta}{2} \right]. \quad (3.1)$$

In equation 3.1, Z and A are the atomic number and atomic mass of the medium, respectively and z is the charge of the incident particle. The parameter β is the velocity of the charged particle in units of the speed of light c , and δ is the density effect correction. K is defined as $K = 4\pi N_A r_e^2 m_e c^2$ with r_e being the classical electron radius and N_A Avogadro's number. The maximum transferable kinetic energy in a single collisions to a free electron is defined in a low energy approximation as $T_{max} = 2m_e c^2 \beta^2 \gamma^2$. The mean excitation energy of the medium is I .

Figure 3.3 shows the mean energy loss rate in different absorber materials for muons, pions and protons depending on their kinetic energy. At lower energies (not shown) additional corrections (shell correction) have to be applied. Up to about 1 to 2 $\beta\gamma$ the differential energy loss is dominated by the β^{-2} term. After this steep decrease the differential energy loss reaches a minimum at about a $\beta\gamma \approx 3$. For larger $\beta\gamma$ the differential energy loss increases logarithmically (relativistic rise) until the Fermi Plateau.

3.3.2 Average Energy Required to Produce an Electron-Ion Pair

A particle must transfer a minimum amount of energy equal to the ionisation energy of the gas molecule to permit the ionisation process. For nitrogen gas (N_2) the first ionisation potential is at about 15.5 eV. There are other mechanisms by which a particle can lose energy without creating ions. For example in the excitation processes a shell electron is elevated to a higher bounding state but does not leave the molecule. Therefore, the average energy needed to produce an electron-ion pair (defined as the W-factor) is larger than the ionisation energy. The W-factor is a function of the gas type involved, the type of radiation and its energy. One observes however that the W-factor depends only weakly of these variables and is notably constant for many gases and radiation types. In Table 3.1 some parameters of commonly utilised gases are shown. The typical W-factor is between 25 and 35 eV/e⁻-ion pair. An incident particle with an energy of 1 MeV will produce about $3 \cdot 10^4$ electron-ion pairs if it is fully stopped within a gas. By assuming that the W-factor is constant for a given type of radiation, the number of produced electron-ion pairs is proportional to the deposited energy. Therefore, the energy deposited by radiation can be determined by measuring the number of produced electron-ion pairs [18].

3.3.3 Detector Gas

The specific requirements of the detectors restrict the choice of the detector gas. The LHC BLM detectors are exposed to large dose rates. Therefore, the utilised gas should not induce ageing effects. In order to operate the detector efficiently it is important that electrons do not attach to the gas molecules. Therefore, electronegative gases, like oxygen, should be avoided. Noble gases allow the onset of the proportional counter region at lower bias fields compared to complex molecules (e.g. N_2), which is an unwanted effect, if this occurs near the detector's operational

Table 3.1: Values of the W-factor for different gases [19].

Gas	first ionisation potential	W-factor [eV/e ⁻ -ion pair]	
		fast electrons	α particles
Ar	15.7	26.4	26.3
He	24.5	41.3	42.7
H ₂	15.6	36.5	36.4
N ₂	15.5	34.8	36.4
Air		33.8	35.1
O ₂	12.5	30.8	32.2
CH ₄	14.5	27.3	29.1

region. The LHC BLM system needs a fast reaction time, which implies a detector gas with high ion mobility.

In the design investigation of the LHC BLM detector different detector gases were utilised. The studies showed that the best choice is nitrogen at 1.1 bar. N₂ has a fast ion mobility which allows to collect 100% of the induced charge within 100 μ s. Should a leak occur and air enter the chamber, the detection properties would not change severely as air contains approximately 78% of nitrogen. However, in the annual system test with a radioactive source, the lower signal due to the lower gas pressure would be detected.

3.3.4 Diffusion and Recombination

The molecules and neutral atoms in a gas are in constant thermal motion. The free electrons and ions liberated within the gas will also take part in this random thermal motion and will diffuse away from their original place of creation. For electrons this diffusion is much more distinct, as their average thermal velocity is larger. σ being the standard deviation of the diffusion distribution, t the elapsed time and D the diffusion coefficient it can be shown that

$$\sigma = \sqrt{2Dt}. \quad (3.2)$$

In simple cases, the value of the diffusion coefficient ([m²/s]) can be predicted from the kinetic gas theory, but in general a more complex transport model is required.

During the movement many types of collisions will occur, mainly between the free electrons, ions, and neutral gas molecules. For example, in such collisions charges can be transferred from neutral molecules to ions. Collisions of free electrons and positive ions may result in recombination where the electron is captured by the positive ion. As the collisions frequency is proportional to the product of the number density of the positive and negative species, the recombination rate can be expressed as:

$$\frac{dn^+}{dt} = \frac{dn^-}{dt} = -\alpha n^+ n^- \quad (3.3)$$

where n^+ is the number density of the positive species, n^- is the number density of the negative species and α is the recombination coefficient. There are two general types of recombination losses, which are the columnar recombination and the volume recombination. The columnar recombination occurs close to the track of the ionising particle and is more severe for densely ionising particles such as alpha particles or fission products. It does not depend on the ionisation rate. Volume recombination in contrast is due to collisions between ions and/or electrons from different tracks. Therefore, volume recombination increases with irradiation rate. Hence, charge separation, and collection at the electrodes should be performed as fast as possible in order to minimize recombination, which can be achieved by utilising high bias voltages.

3.3.5 Charge Mobility

By applying an external electric field (bias voltage on the electrodes) to the region in which the electrons and ions are generated in the gas, the electrostatic forces will move the charges away from their point of creation. The net motion of the charges comprises the random thermal motion and the drift due to the applied electrical field. The drift velocity of ions in gas can be predicted quite accurately from the following relation:

$$v = \frac{\mu\xi}{p} \quad (3.4)$$

where v is the drift velocity, μ is the mobility ($[\text{m}^2 \text{ atm}/\text{V s}]$), ξ represents the electric field strength and p is the gas pressure. The mobility μ stays quite constant over a wide range of the electric field and gas pressure and is similar for negative and positive ions in the same gas. Typical values are between 1 and $1.5 \cdot 10^{-4} \text{ m}^2 \text{ atm}/\text{V s}$ for detector gases of medium atomic number. At a pressure of 1 atm, a typical field strength of 10^4 V/m and an electrode spacing of a centimetre will result in an ion collection time in the order of milliseconds.

Free electrons behave quite differently due to their much lower mass compared to ions. The acceleration in the electrical field results in larger drift velocities between the collisions with neutral gas molecules. The value of the mobility described in equation 3.4 is for free electrons typically about a factor of 1000 greater. Therefore, typical collection times for electrons are in the order of microseconds, taking the parameters mentioned for ions into account.

Chapter 4

Monte Carlo Simulation Methods

During the past decades particle shower simulations, in radiation physics and high-energy physics considerably increased in importance. In parallel, major advancements in computer technology, resulting in a rapid increase in computing power, took place. Projects in high energy physics, like accelerators and detectors, increase in complexity and financial aspects. In the same time the steady decrease of the safety limits for radio protection and the protection limits of the more advanced equipment, e.g. superconducting magnets, demands more accurate calculations which are now part of design studies and operation of new facilities. In particular, Monte Carlo simulation codes to transport particles through matter while simulating their interaction with the medium are now quasi standard for these applications.

Facilities like the LHC and its experiments (i.e. ATLAS, CMS, etc.) utilise such codes in their design studies. These codes are very complex and need to describe the underlying physics processes in a very careful and detailed way. The simulation codes must describe the interactions of low energetic neutrons as well as hadronic interactions at energies beyond the limits of existing accelerators. The codes should provide user friendly interfaces, to model the often complex geometries, to set the required physics processes and to score important quantities like energy deposition or particle fluence at any specified location. It is also required that the code delivers statistically significant results within reasonable consumption of CPU performance and despite complex geometries.

In 1993 independent studies on these subjects were conducted at CERN and KEK. In the fall of 1994 the activities were merged which resulted in a proposal, RD44, to construct an entirely new program based on object-oriented technology. The objective was to write a detector simulation program, which meets the requirements for the next generation of high-energy physics experiments. The initial coverage quickly widened when individuals from other communities like the nuclear, accelerator, space and medical physics societies joined. After the first production release in 1998 was the collaboration subsequently renamed to Geant4.

The studies in this thesis are performed within the LHC beam loss monitoring section. Due to historical reasons and the need of specific physics implementations, the group choose to utilise Geant4.

4.1 Geant4

Geant4 is a tool-kit to simulate the passage of particles through matter. Its areas of application include high energy, nuclear and accelerator physics, as well as studies in medical and space science [20][21][22].

The free software package is written in C++ and exploits advanced software-engineering techniques and object-oriented technology to achieve transparency. It is composed of tools, which can be utilised to accurately simulate the passage of particles through matter. All aspects of the simulation process have been included in the tool-kit [22]. Complex geometries can be modelled including the involved materials. The fundamental particles of interest, the generation of primary events and the tracking of particles through materials and electromagnetic fields are implemented. Included are also the physics processes governing particle interactions, the response of sensitive detector components, the generation of event data, the storage of events and tracks, the visualization of the detector and particle trajectories, and the capture and analysis of simulation data at different stages of the simulation.

4.1.1 Application Development

The user can construct stand-alone applications or applications built upon another object-oriented frameworks (e.g. ROOT). In both cases the tool-kit will support the user from the initial problem definition to the production of results and graphics for publication. The tool-kit includes user interfaces, built-in steering routines and command interpreters, which operate at every stage of the simulation.

There is a large set of physics models in Geant4 to handle the interactions of particles with matter across a very wide energy range. Data and expertise were taken from many sources around the world and therefore Geant4 acts as a repository, which incorporates a large part of the principles about particle interactions.

For a specific application the user-physicist has to choose from these options and implement the adequate description for the problem made consideration.

4.1.2 Geant4 - Hadronic Models

In Geant4, cross-sections and physics models for hadronic interactions with energies ranging from thermal energies (for neutrons) to hundreds of GeV are included (see Figure 4.1). The user can choose from many available physics models, depending on energy range, precision required and CPU performance available.

At high energies, above about 20 GeV, the Quark-Gluon String (QGS) model and the Fritiof-like String model (FTF) provide theory-driven interaction models of the initial projectile-nucleon collisions. At energies below about 10 GeV two cascade models are provided. One is following the “Bertini approach” and the other one is the more theory-driven Binary cascade. The initial interaction within the nucleus is simulated by each of these models, by generating high energetic secondaries, leaving the nucleus in a highly excited state. There are a number of models available to describe the de-excitation. The Geant4 precompound model is one of them which starts by

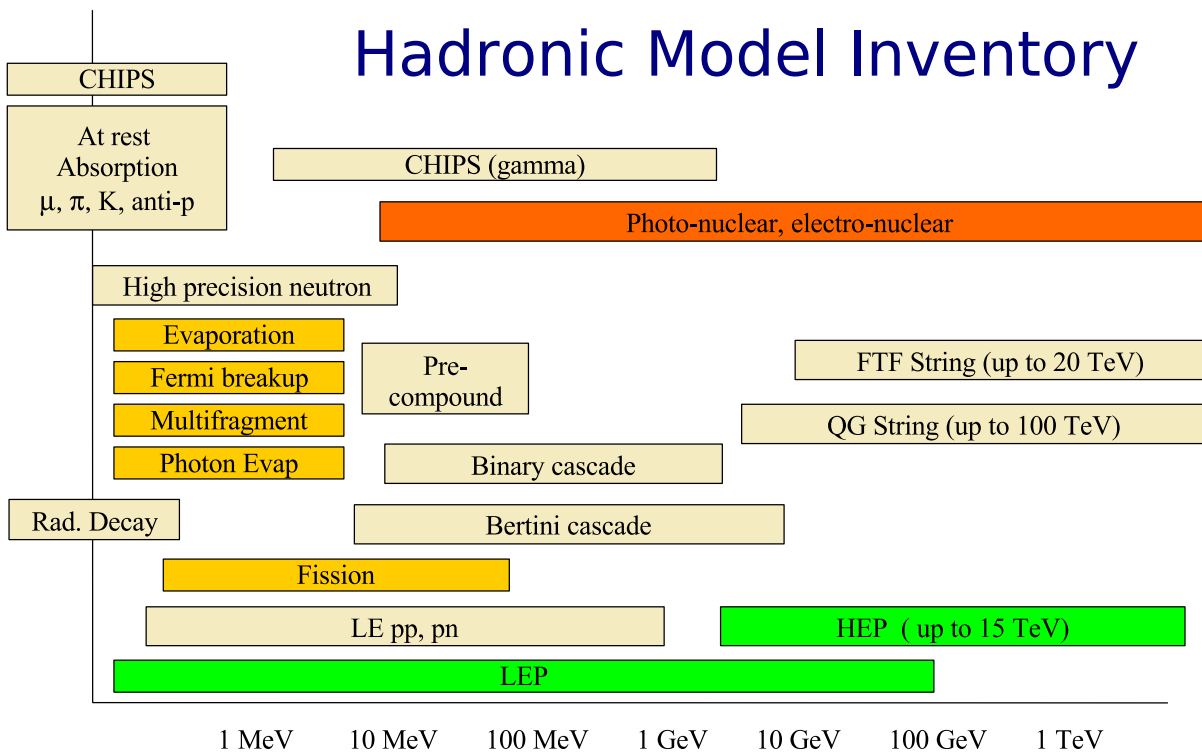


Figure 4.1: Overview of the Geant4 hadronic model inventory [23].

decaying the excitations formed during the high energy interactions or cascades and calls then one or more of the available fission, Fermi break-up, multi-fragmentation and evaporation routines. For the QGS and Binary cascade model the currently utilised back-end is the precompound model. The Bertini-type cascade model has its own evaporation model. At energies below 20 MeV high precision neutron processes and photo-evaporation codes are available.

The Low Energy Parameterised (LEP) and the High Energy Parameterised (HEP) models cover all long-lived particles at all energies. They are also designed to describe hadronic showers reasonably well. The LEP and HEP models are a fast alternative to the mentioned theory-driven models. The LEP models are especially important as they cover the transition region, from 10 GeV to 20 GeV, between the cascade models and the string models, because some particles are not covered in this region by the theory-driven models. Other models shown in Figure 4.1 and not mentioned are described in more detail in [24].

4.1.3 Geant4 - Physics Lists

Geant4 provides several predefined physics lists. The physics lists comprise sets of the mentioned physics models that cover all materials, beam particle types and beam energies. They are defined to meet the different levels of physics accuracy, and CPU performances needed for the different fields of application.

Physics lists utilised in this work are LHEP, QGSP, QGSP-BERT-HP and FTFP. The LHEP list comprises of the LEP and the HEP models mentioned, QGSP comprise QGS and the precompound model, QGSP-BERT-HP utilised QGS, the “Bertini approach” and the high precision neutron extension and the Fritiof-like string model and the precompound model are combined to

the FTFP physics list.

Investigations on the hadronic showers described in [24] show that the LHEP physics list describes the shower shape well at high energies. The best description of the shower shape was found for QGSP-BERT-HP.

The Geant4 developers recommend to utilise in applications which need a good simulation of shower shapes either the LHEP physics list, or, if in general more precise physics is needed, the QGSP-BERT physics list [24].

The precise transportation of low energy neutrons, with kinetic energies below 20 MeV, can be activated by utilising the -HP extension of physics lists. As neutrons propagate further than charged particles through a material they can influence the shower shape and can deposit energy in the tails of hadronic showers.

For the simulations described in this thesis of the final LHC BLM and the SPS BLM detector response functions and the simulations conducted for the HERA proton beam dump, the QGSP-BERT-HP physics list was applied, as recommended.

4.1.4 Production Thresholds - Range Cut-Off Value

The production of secondary particles has to be stopped below a certain energy threshold because some electromagnetic processes have infrared divergence and cause a large increase of the CPU time. But the energy threshold has to be low enough to derive the physics results one is interested in.

The traditional solution for this problem in Monte Carlo methods is to impose an absolute cut-off in energy. Below this cut-off particles are stopped and the remaining energy is dumped at the actual particle location. But this may cause an imprecise stopping location and deposition of energy.

Therefore, a production threshold for secondaries is imposed in Geant4. This threshold is defined as a distance, not as energy. This distance is in Geant4 internally converted to an energy cut-off for individual materials. The primary particle loses energy by producing secondary electrons or gammas. If the primary no longer has enough energy to produce secondaries, which can travel at least the specified distance, two things happen. First, the particle undergoes only discrete energy loss and no secondaries are produced and second, the primary particle is tracked down to zero energy. This results in a correct stopping location. Only one value of the secondary production threshold distance for all materials is needed. A recommendation of Geant4 is 1 mm. The user needs to decide the best value, which will depend on the size of the sensitive elements within the simulation and the available CPU power. For more convenience, "secondary production threshold distance" will be referred to as range cut-off value.

Exceptionally, a process can produce secondaries below the specified threshold. For example, by taking the geometry into account one may realise that a produced particle, even below the threshold, is able to reach the sensitive part of the detector. One other example is the gamma conversion, which will always produces positrons, even at zero energy, for further annihilation.

Chapter 5

Ionisation Chamber Response Simulations and Measurements

5.1 Introduction

The main beam loss monitor of CERN's Large Hadron Collider (LHC) is a parallel plate ionisation chamber. The LHC Beam Loss Monitoring (BLM) system is utilised to protect the superconducting magnets from quenching and to protect the machine's components from damage. Around 4000 of these monitors will be installed in the LHC. The particles that are lost from the beam initiate hadronic showers through the magnets, which are measured by the monitors installed outside of the cryostat around each quadrupole magnet. The monitors probe the far transverse tail of the hadronic shower. Depending on the loss location the monitor will be exposed to different radiation fields. In order to determine the number of lost beam particles it is necessary to calibrate the monitor under controlled conditions. To achieve this goal, Geant4 [22] simulations and test measurements were performed [20][21]. This chapter covers the simulation of detector response functions, the estimation of systematic errors in the simulations and the validation of the simulations by measurements. Different measurements have been performed at T2-SPS transfer line (CERN), at the SC-RP Calibration Laboratory for Radiation Protection Instruments (CERN), at the The Svedberg Laboratory (Uppsala, Sweden) and at the CERF target area (CERN-EU High Energy Reference Field Facility) and are compared to the simulations.

5.2 Simulation Details

The Monte Carlo simulation code Geant4 8.0 - released 10 February 2006 (patch-01) and the Monte Carlo simulation code Geant4 8.1 - released 27 July 2006 (patch-01) [22] are utilised to simulate the deposited energy in the Super Proton Synchrotron (SPS) beam loss detector which is an ionisation chamber. The energy deposition simulation is performed for different particle types and energies. The predefined physics lists QGSP and the QGSP-BERT-HP are utilised to simulate the electromagnetic and hadronic interactions [25]. The results obtained in the following studies are also valid for the LHC BLM monitor due to similar design. At the beginning of this work the final production phase of the LHC BLM monitor had not yet been started.

5.2.1 Detector Geometry and Sensitive Volume

The SPS ionisation chamber geometry is modelled in great detail in Geant4. In Figure 5.1 the layout of the simulated detector is shown. All main parts of the detector are modelled, except small components such as the screws in order to reduce the complexity of the model. The materials utilised are selected from typical material property tables and specified by only their main chemical constituents (no impurities). The outside walls of the detector are fabricated from stainless steel. The inner electrodes are produced from aluminium. The outer portion of the connecting rods (spacers) is made from aluminium tube, the inner of stainless steel bar. The insulator rods that connect the electrodes to the outer part of the detector are made of a ceramic material. The exact composition of the ceramic is unknown, therefore it is defined as SiO_2 . The detector is pressurised with nitrogen at 1.1 bar at room temperature (20°C). The electronics housing is constructed of aluminium.

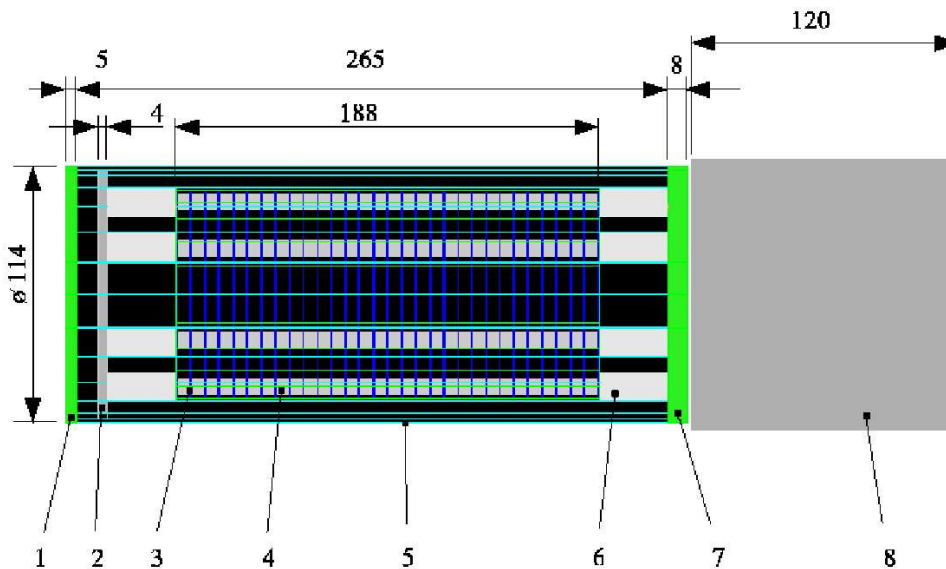


Figure 5.1: SPS beam loss ionisation chamber layout. 1) Top plate 2) Aluminium plate 3) Aluminium electrode 4) Connecting rods (spacer) 5) Outer tube 6) Insulator 7) Bottom plate 8) Electronic box

To determine the number of electrical charges that can contribute to the detector signal, the sensitive gas volume of the detector has to be estimated:

Each particle that passes through the detector deposits some energy within the nitrogen gas. This energy deposition causes mainly excitation and ionisation of the gas molecules. The charges produced are proportional to the deposited energy. This proportionality factor or W-factor is in principal a function of the material (gas), the type of the radiation and the energy of the particles. Empirical observations have shown that the W-factor does not show a strong dependence on the energy and the particle type and can therefore be approximated in most cases by a constant value for the respective gas ([19]). For nitrogen a value of 34.8 ± 0.2 eV per produced electron-ion pair is found. Not all the charges produced in the detector gas will be collected by the signal electrodes. Only the ones that are transported by the electric field between the electrodes generate a signal. Therefore, the sensitive volume mainly consists of the volume between the electrodes. In the following section this topic is discussed in more detail.

5.2.2 Readout and Analysis

During the run time of the simulations the data for each event (corresponding to one primary particle) are recorded as a “ntuple” by utilising ROOT classes ([26]). By utilising the sensitive detector class of Geant4 the energy deposition in each step the particle performs in the corresponding gas volume is recorded. The data analysis was performed with ROOT macro files.

5.2.3 Statistical Error Calculation

The energy deposition of charged particles in matter is of a statistical nature. In thin layers for any given primary particle type, the energy deposition is described by the Landau distribution [27].

The mean value of the energy deposition corresponds to the mean value of the Landau distribution. This value is larger than the most probable energy loss, because the Landau distribution is skewed; it has a large high-energy tail. An example for the energy deposition of a 1 GeV μ^+ in the SPS detector is shown in Figure 5.2. The distribution is fitted with the Landau function [28].

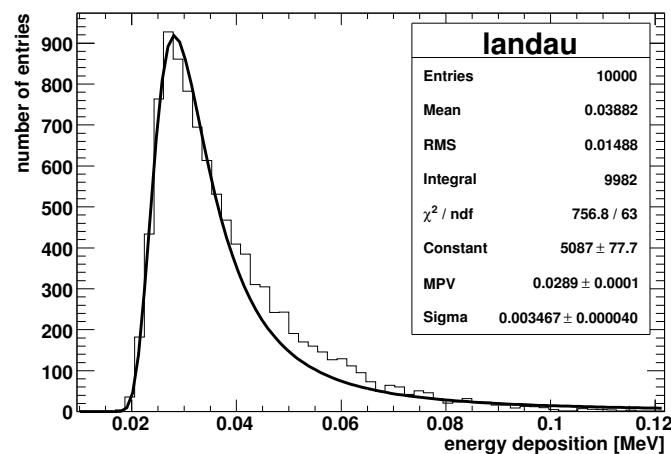


Figure 5.2: Landau distribution. The deposited energy in the SPS detector for a 1 GeV μ^+ is fitted with the landau function.

The statistical error of the detector response was determined by calculating the mean value of the energy deposition and the corresponding standard error of the mean (see section B).

5.2.4 Estimation of Systematic Errors

In the simulation different types of systematic errors are estimated as follows:

Sensitive Volume

The appraisal of the sensitive volume is a source of systematic uncertainty. It is considered to include the volume of the gas between the charge collecting electrodes. For collecting the charges an electric field is created between the electrodes. This electric field is homogeneous in the centre

region and at the edge of the electrodes it develops a strong inhomogeneity. The region of the fringe field is considered by increasing the diameter of the sensitive volume. Figure 5.3 shows the electric flux lines and the equipotential lines between two electrodes and the detector wall simulated with Superfish ([29]). In the area enclosed by the drawn triangle the charges will propagate towards the electrodes. The height of the triangle is approximately 2.5 mm. The actual electrode diameter is 93 mm and the sensitive volume diameter from the simulation was determined to be 95 mm. The difference in volume is about 4%. Compared to the total gas volume of the detector the sensitive volume comprises about 50%.

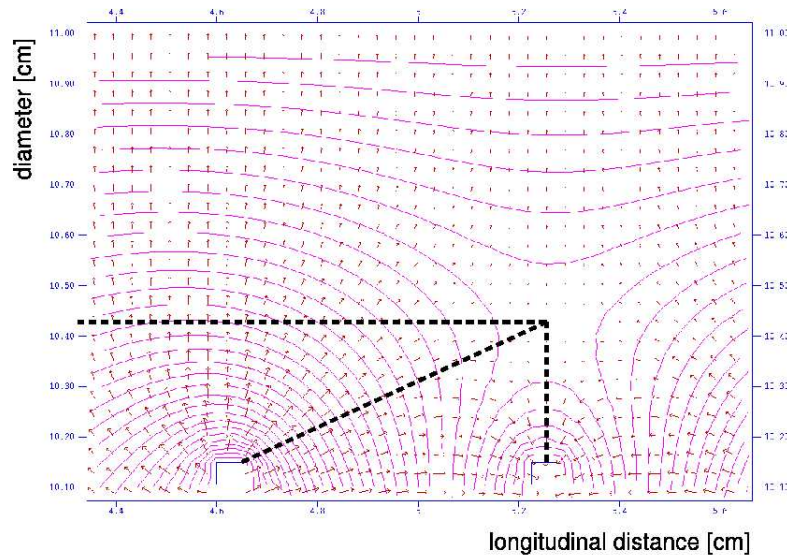


Figure 5.3: Electric flux lines and the equipotential lines between two electrodes and the detector wall.

Rang Cut-Off Value

One of the parameters that can be set by the Geant4 user is the range cut-off value. Some electromagnetic processes require a production threshold that avoids infrared divergence, which would extremely increase the CPU time. Hence gammas, electrons and positrons need a production threshold, which the user should set. This threshold is defined as a distance that is in Geant4 internally converted to an energy cut-off for individual materials. Secondary particles, which have less energy as the one specified by the range cut-off value are not generated and the according energy is deposited at the actual location of the primary particle. A more detailed description of the range cut-off value can be found in section 4.1.4.

A systematic analysis of the deposited energy in the sensitive detector volume for different range cut-off values is performed. Protons with energies of 200 MeV, 10 GeV and 400 GeV were generated as a pencil beam parallel to the detector axis and impinging at the centre of the ionisation chamber. Figure 5.4 shows that decreasing the cut value the deposited energy per primary particle increases. But this also has the effect that the CPU time increases, due to the fact that more secondary particles are generated and have to be tracked. At one point a compromise has to be made, between exactness of the result and the afforded time. The different responses in respect to the particle energy are due to larger induced showers at higher energies.

With 200 MeV protons additionally simulations with range cut-off values between 1 nm and 10 μm

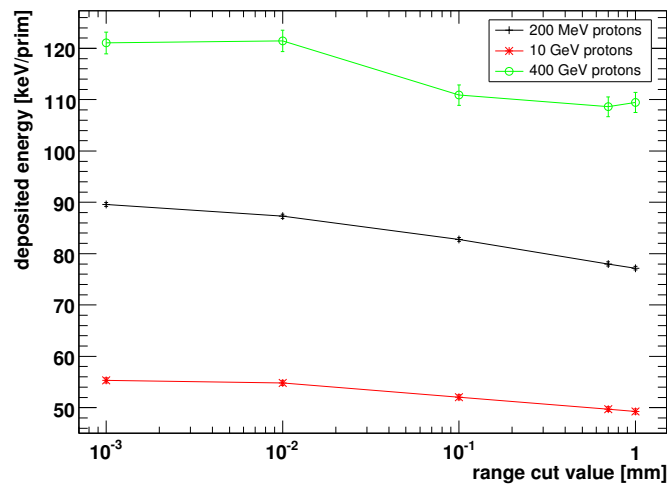


Figure 5.4: Energy deposition in the detector versus different range cut-off values. The pencil beam (protons) impacts longitudinally to the detector axis.

were performed. One would expect a more or less constant mean energy deposition, because lower energetic particles are produced which will less contribute to the absolute result of the energy deposition. The results for these range cut-off value scan are shown in Figure 5.5. An increase in response of 2.6% for a step from 10 μm to 1 μm is observed. A reduction of the range cut-off value further by three orders of magnitude to 1 nm increased the response by only 0.8% compared to the one simulated at 1 μm . This shows that a plateau in energy deposition is reached, as expected.

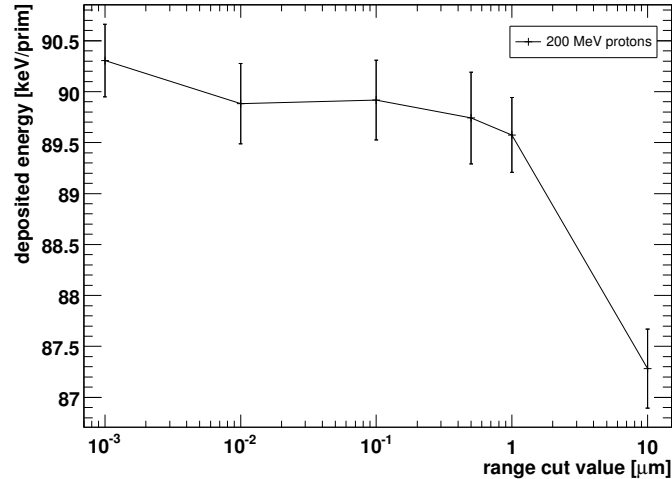


Figure 5.5: Energy deposition in the detector for protons at 200 MeV versus different range cut-off values. The pencil beam impacts longitudinally to the detector axis.

In Table 5.1 the ratios of the mean energy deposition at different range cut-off values are plotted. One can see a maximum difference in energy deposition of 14.5% between the 1 mm and the 1 nm range cut-off value. In the last column the ratio between the mean energy deposited at 10 μm range cut-off value and the mean energy deposited at the other range cut-off values is plotted. The maximum difference in energy deposition is about 3.3%.

A range cut-off value of 10 μm was chosen for the simulation of the detector response. From the

investigation of the systematic error due to different range cut-off values, an uncertainty of 3.3% was derived for a range cut-off value of $10\ \mu\text{m}$. This seems to be a good compromise between CPU time consumption and accuracy of the results.

Table 5.1: Mean energy deposition of protons in the ionisation chamber for different range cut-off values. 200 MeV proton energy. The ratios are between the mean energy deposited at 1 mm and at $10\ \mu\text{m}$ range cut-off values and the mean energy deposited at the other range cut-off values.

range cut-off [μm]	E_{dep} [keV/proton]	error [keV/proton]	ratio $E_{dep(1\text{ mm})}/E_{dep}$	error	ratio $E_{dep(10\ \mu\text{m})}/E_{dep}$	error
1000	77.17	0.35	1	0.01	1.131	0.006
10	87.28	0.39	0.884	0.006	1	0.006
1	89.57	0.37	0.862	0.005	0.974	0.005
0.5	89.74	0.45	0.860	0.006	0.973	0.006
0.1	89.92	0.39	0.858	0.005	0.971	0.005
0.01	89.88	0.39	0.859	0.005	0.971	0.005
0.001	90.31	0.36	0.855	0.005	0.967	0.005

Impact Angle

Another source of systematic error is the impact angle of the particles onto the detector. Different wall thicknesses with respect to the angle cause a change in energy cut-off which means particles with kinetic energies below a corresponding threshold are absorbed in the walls and do not contribute to the signal. Therefore the detector response depends on the impact angle of the particles. For protons this effect was studied and the results are shown in Figure 5.6. The different impact angles are relative to the longitudinal detector axis. As an example, protons with an energy of 1 GeV show in the worst case a difference of 40% in detector response which is for impact angles of 0° and 90° . In the following chapters the detector response functions are convoluted with particle fluence spectra. In this calculations the impact angle of the particles is neglected which gives rise of statistical and systematic errors depending on the detector position and utilised response functions.

Physics Lists

Geant4 offers the possibility to utilise predefined physics lists. Figure 5.7 shows results obtained with different physics lists. Used are the LHEP list of Geant4.7.0.p01, the LHEP list of Geant4.8.0 and the QGSP list of Geant4.8.0. The simulations are performed with protons launched as a pencil beam, which impacts at the centre of the detector in longitudinal to the detector axis. The utilised physics lists show up to 50 GeV equal results in deposited energy per primary proton. Above this energy the QGSP physics list shows a larger signal than the QGSP list of Geant4.8.0, which is similar to the LHEP list of Geant4.7.0.p01. At 1 TeV the maximum difference is about 40%.

For all further simulations described in this section the QGSP physics list of Geant4 8.0 - released 10 February 2006 (patch-01), if not mentioned otherwise, is utilised. This was recommended by Geant4 experts [25].

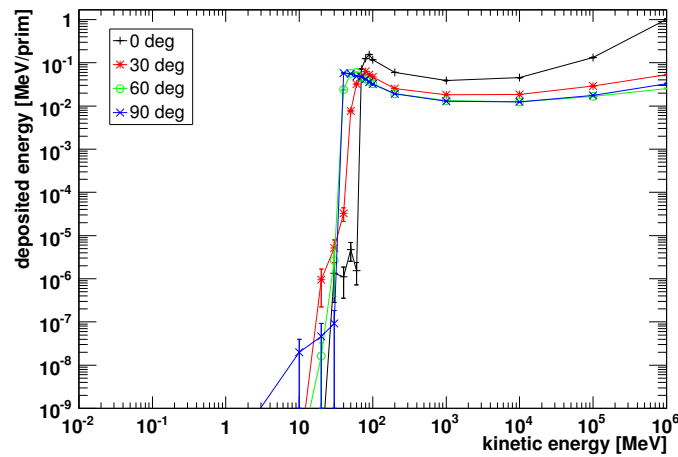


Figure 5.6: Response of the detector in deposited energy for different impact angles. Angle zero corresponds to the longitudinal direction (uniform irradiation).

In the following chapters detector response simulations are conducted. The spectra derived at different locations (detector positions) do not show particles with energies above 50 GeV. Hence, the uncertainties arising from different physics list can be neglected and it is assumed that the response for other particle types behaves in the same way as the protons (except neutrons). The final results, which are compared to measurements, are generated with the physics list QGSP-BERT-HP. This physics list includes an improved modelling of the hadronic reactions between a few MeV and about 10 GeV and a more precise simulation of neutrons below 20 MeV. Also the final detector response function simulations were performed with QGSP-BERT-HP [24].

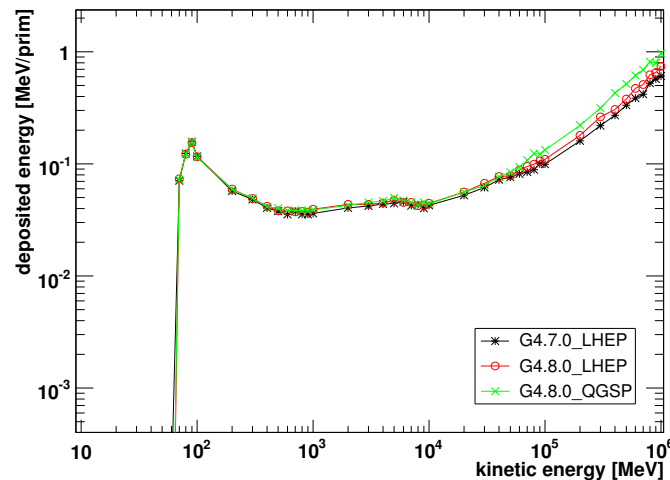


Figure 5.7: Comparison between different Geant4 physics lists (uniform irradiation).

5.3 Detector Response

5.3.1 Response Functions for various Particle Types

Depending on the loss location of the primary protons in the LHC the BLM detectors will be exposed to different radiation fields. The energy of the particles is spread over a large range from keV to TeV and their number rapidly decreases with energy. Therefore, it is necessary to calibrate the detector and to know the response of the different particle types at various kinetic energies. This can be achieved with Monte Carlo simulations and calibration measurements.

With Geant4 several runs for different primary energies are performed. The energy is increased from 1 keV up to 10 TeV in 59 unequal steps. The steps are chosen to fit best the requirements. At each step in the low energy range up to 10^5 and for higher energies up to 10^3 primary particles were simulated. The particles are uniformly distributed over the front or the side of the detector (parallel or normal to detector axis). Primary particle types are electron (e^-), gamma (γ), muon (μ^\pm), neutron (n), pion (π^\pm), positron (e^+) and proton (p).

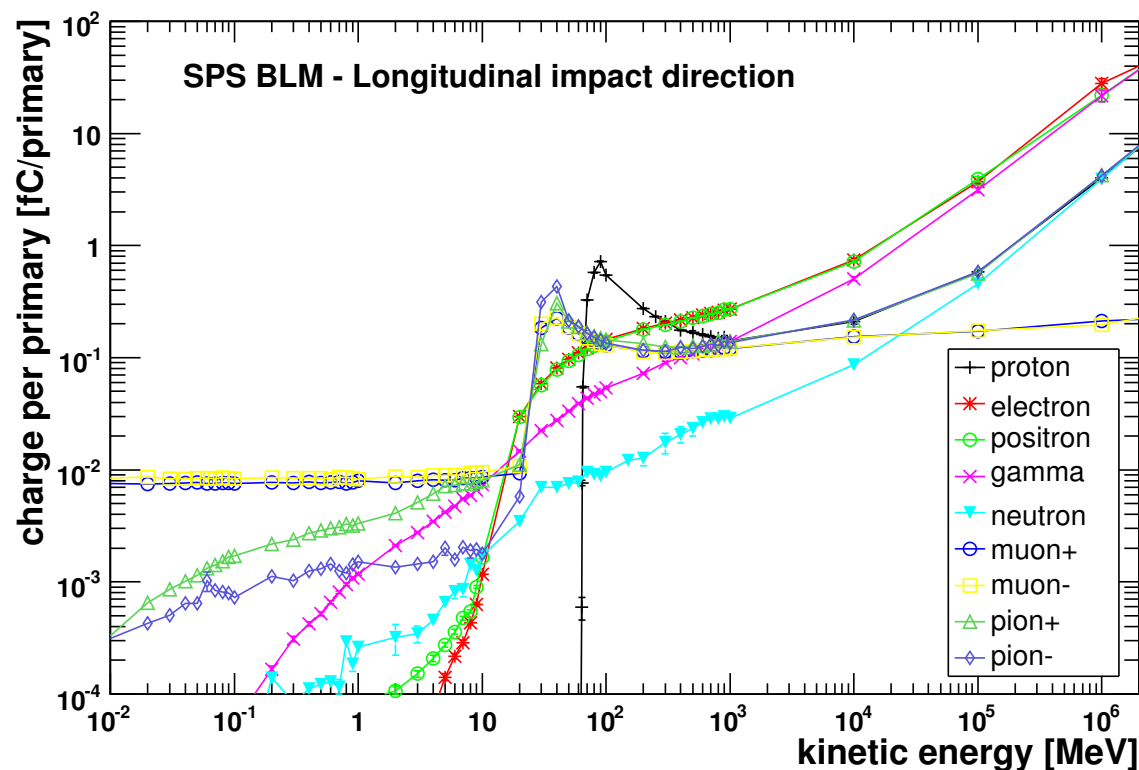


Figure 5.8: Response function for different particle types with different kinetic energies in the range of 10 keV up to 1 TeV. Particles are launched longitudinally to the detector axis (QGSP-BERT-HP).

The simulated detector response functions for longitudinally (with respect to the detector axis) impacting particles is shown in Figure 5.8. For transversely impacting particles it is shown in Figure 5.9. The detector response is normalised to the number of primary particles and is expressed in fC/primary. The response curves are shown for an energy range of 10 keV to 1 TeV.

In the case of longitudinally impacting particles the detector response rises at about 20 MeV for

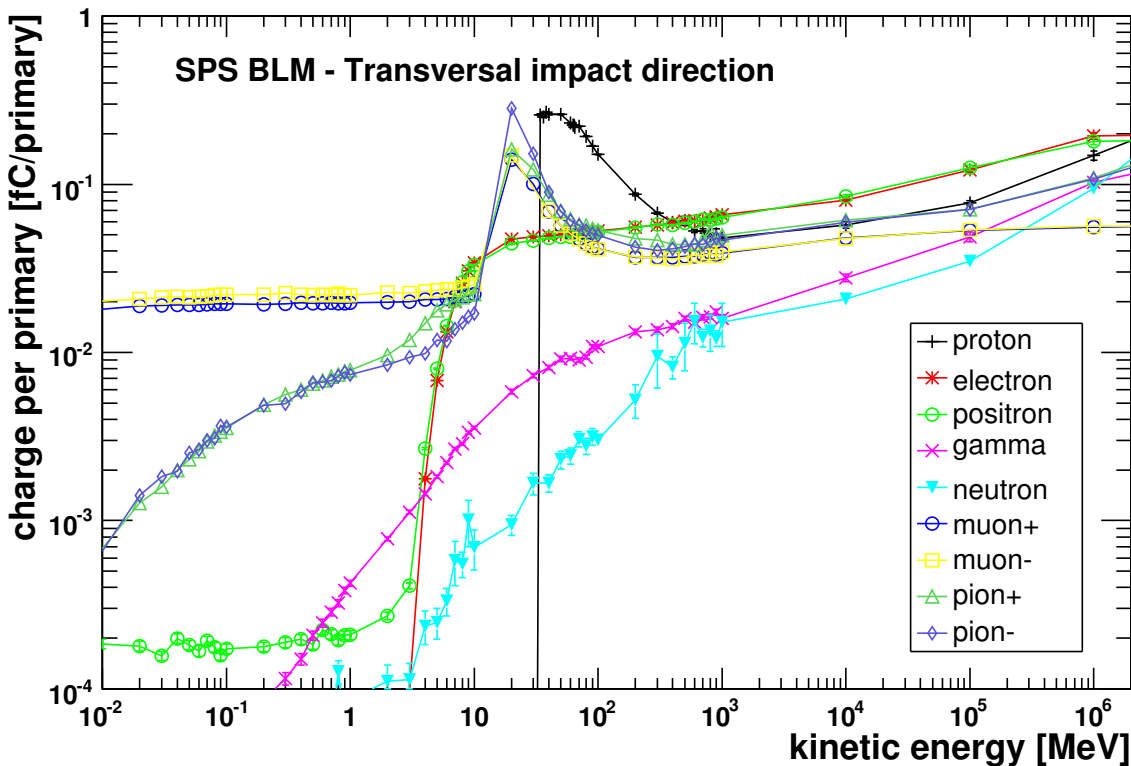


Figure 5.9: Response function for different particle types with different kinetic energies in the range of 10 keV up to 1 TeV. Particles are launched transversely to the detector axis (QGSP-BERT-HP).

all particle types. In the transverse case the rise in response is at lower energies at about 3 to 10 MeV. Except gammas and neutrons do not show a sudden rise in response, their response function rises steadily with kinetic energy. The lower energy cut-off for the transverse impact is derived from the different amount of material the particles have to pass to enter the detector. Particles with energy below a certain threshold are absorbed in the wall. The side wall has a thickness of 2 mm compared to the end caps of the detector which have a thickness of 5 mm and 8 mm.

An estimated factor of 2 was found for the difference of absolute signal height comparing the longitudinal response curves to the transverse ones. This is determined by the different path lengths the particles travel in the sensitive gas volume. The sensitive volume is 18 cm long and has an averaged diameter of 7.5 cm, dividing the two results in a factor of 2.4 which is close to the approximated factor of 2 in signal height. The response functions for the longitudinal case rise above about 10 GeV disproportionately high which is topic of further investigations described in section 5.3.1.

Protons show a very sharp edge in response at 60 MeV for the longitudinal case and at 35 MeV for the transverse case. Also μ^\pm and π^\pm show a steep rise in response at about 30 MeV and 10 MeV respectively to impact direction. These particles are absorbed below their specific energy threshold in the detector wall and cannot reach the sensitive volume to deposit energy. The rising is followed by a peak in response, which occurs because the interaction cross section increases as the charged particle's energy decreases. Beyond the peak the detector response is constant for μ^\pm and up to several GeV for protons and π^\pm . The particles pass the whole detector and the

increase in interaction cross section is rather small so their energy loss is almost constant.

No peak in response is observed for electrons, positrons, gammas and neutrons. Particles with an initial kinetic energy above the energy necessary to penetrate the detector wall arrive at the sensitive volume with low kinetic energy. If the electron's energy falls below a certain level (critical energy) it dissipates its energy rather by ionisation and excitation as by generating more shower particles. This leads to the smoother detector response functions for electrons and positrons.

Neutrons and gammas do not carry charge and therefore do not interact with matter by Coulomb interaction. Therefore, their response function has no peak.

As previously mentioned is the deposited energy in the sensitive volume converted to produced charges by the W-factor which for nitrogen is 34.8 eV per electron-ion pair.

Validation Calculations for different Particle Types

In section 5.3.1 the detector response functions for several particle types at different energies are presented. Some results shown in Figure 5.8 and Figure 5.9 are verified by analytical calculations which are the penetration energy for protons, electrons and gammas, the energy a proton needs to pass the detector and the energy deposition of muons.

The calculations correspond to a longitudinal irradiation of the ionisation chamber respectively to the detector axis.

By taking the geometrical properties of the detector into account a summation of the path lengths in a specific material, which has to be traversed by the particle is performed 5.1. The symbol $\sum_{material}$ refers in this section to the sum of path lengths in a certain material.

The density of stainless steel is approximated by the density of iron.

Total length of material to transverse:

$$\begin{aligned} \text{stainless steel:} & \quad \sum_{Fe} = 0.5 \text{ cm} \\ \text{aluminium:} & \quad \sum_{Al} = 0.4 \text{ cm} + 31 \times 0.05 \text{ cm} = 1.95 \text{ cm} \\ \text{nitrogen:} & \quad \sum_{N_2} = 2 \times 3.1 \text{ cm} + 0.95 \text{ cm} + 30 \times 0.575 \text{ cm} = 24.4 \text{ cm} \end{aligned}$$

Density of the materials:

$$\begin{aligned} \text{stainless steel:} & \quad \rho_{Fe} = 7.87 \text{ g/cm}^3 \\ \text{aluminium:} & \quad \rho_{Al} = 2.7 \text{ g/cm}^3 \\ \text{nitrogen:} & \quad \rho_{N_2} = 1.165 \cdot 10^{-3} \text{ g/cm}^3 \quad (20^\circ\text{C}, 1 \text{ bar}) \end{aligned}$$

Particles that can deposit energy in the sensitive volume have to pass at least 0.5 cm of iron (instead of stainless steel) and 0.45 cm of Al. The distance in nitrogen is neglected due to its relatively low density. Multiplying the path length with the corresponding density derives the

amount of material to be traversed in units of $[g/cm^2]$:

$$\sum_i \Delta x_i \rho_i = 0.5cm \cdot 7.87 \frac{g}{cm^3} + 0.45cm \cdot 2.7 \frac{g}{cm^3} = 5.15 \frac{g}{cm^2} \quad (5.1)$$

The National Institute of Standards and Technology (NIST) provides a large on-line database of physical reference data [30]. One of the subsection is denoted by "Stopping-Power and Range Tables for Electrons, Protons, and Helium Ions" with further links to either ESTAR, ASTAR and PSTAR [31]. The programs calculate stopping power and range tables for protons, electrons and helium ions in various materials. By selecting a material and the desired energies, or using the default energies, the corresponding stopping powers and ranges are tabularly presented.

The kinetic energy required to pass the calculated range of $5.15 g/cm^2$ is read off for protons and electrons in the corresponding range table.

Calculation for Protons

A kinetic energy of approximately 65 MeV is derived for protons. Protons which have an initial kinetic energy higher than 65 MeV are able to reach the sensitive volume and create a signal. Comparing this result to the simulations shows a good agreement.

Calculation for Electrons

For electrons a kinetic energy of 9 MeV is derived which is in good agreement to the simulation results.

Calculation for Gammas

If mono energetic photons penetrate a layer of material with a mass thickness of $d(= \rho \cdot x)$ and density ρ the incident intensity I_0 reduction of the emerging particles is calculated by the exponential attenuation law

$$I = I_0 e^{-(\mu/\rho)d} \quad (5.2)$$

which can be rewritten as

$$\mu/\rho = d^{-1} \ln(I_0/I) \quad (5.3)$$

μ/ρ is the mass attenuation coefficient.

For gammas the required kinetic energy at which the initial intensity I_0 is attenuated to $\frac{1}{e}$ when passing the mass thickness of $5.15 [g/cm^2]$ in iron is calculated by rewriting formula 5.3 to

$$\frac{\mu}{\rho} \cdot \underbrace{\rho \cdot x}_{5.15 g/cm^2} = 1 \Rightarrow \frac{\mu}{\rho} = 0.19 \left[\frac{cm^2}{g} \right] \quad (5.4)$$

A total mass attenuation coefficient of $0.19 \text{ cm}^2/\text{g}$ is derived. The NIST Photon Cross Sections Database [32] quotes the total attenuation coefficients versus photon energy. For a total mass attenuation coefficient of $0.19 \text{ cm}^2/\text{g}$ the required photon energy of 150 keV is found. This result is in good agreement to the simulated data.

Calculation of the total Energy Deposition for Protons

The minimum energy a proton requires to pass the whole sensitive volume is calculated. The proton has to pass a mass thickness of 9.2 g/cm^2 which is the sum over all iron and aluminium path lengths multiplied by the respective density. From the previously described range tables a kinetic energy between 80 and 90 MeV is derived. A proton at this energy will deposit all its energy in the detector and therefore generate the highest response which is represented by the peak of the response function for protons in Figure 5.8. The peak is at about 90 MeV which shows a good agreement to the calculation.

Calculation of Muon Energy Deposition

To verify the simulation results, calculations of the energy deposition in the detector gas with the Bethe-Bloch formula ([7]) are performed. For different kinetic energies (30 MeV to 1 GeV) the energy loss in the gaps between the electrodes was calculated and summed which is proportional to the detector signal. A positively charged muon (μ^+) with a kinetic energy of 34 MeV is completely absorbed in the detector, most probably in one of the electrodes. During the passage the muon is losing constantly energy while its mean rate of energy loss ($\langle -dE/dx \rangle$) increases. In the last steps it loses larger amounts of its remaining energy, which leads to a high uncertainty in the calculation. In this case a small change in primary kinetic energy makes a large change in the result due to the statistical nature of the processes, which are described by analytical formulae. A comparison of the calculated energy loss in the sensitive gas to the simulated energy deposition is shown in Table 5.2. The density effect correction is not included in the calculations with the Bethe-Bloch formula, which predicts for higher energies a lower mean rate of energy loss.

Table 5.2: Comparison of the energy deposition in the sensitive volume calculated with Bethe-Bloch and simulated with Geant4.

μ^+	Bethe-Bloch calc.	Geant4 simulation		ratio
E_{kin}	E_{dep}	E_{dep}		sim/calc
[MeV]	[keV/ μ^+]	[keV/ μ^+]	error	
30	80.05	72.27	0.033	0.9
34	112.15	95.14	0.050	0.85
40	91.14	81.45	0.042	0.89
1000	40.78	38.60	0.026	0.95

The ratio of the results for a 1 GeV μ^+ is 0.95. For a 34 MeV μ^+ the difference between calculation and simulation is approximately 15%. The results for the other considered energies are within these two cases. Finally, the best agreement is found for a 1 GeV μ^+ , here the simulation fits the calculation with Bethe-Bloch within 5%. At lower kinetic energies the difference between the simulated results and the calculated ones is still within 15%. It is shown that the simulation

predicts in all cases a lower energy deposition in the sensitive gas compared to the calculations performed with Bethe-Bloch.

Irradiation of separate Parts of the Detector

The simulated results show for all longitudinal impinging primary particles, except for muons, onwards from 10 GeV a relative steep increase in detector response. This attribute of the response functions was further investigated. In the simulation several parts of the detector are separately irradiated to characterise this slope. The beam positions, where the particles have to travel through more material (connecting rods and the detector wall), show an above average increase in the energy deposition. Each result is multiplied by its fractional area and added up to a total sum for the detector response.

The results are displayed in Figure 5.10. The comparison of the detector signal derived by summing the results for the separate irradiation to the result obtained by the simulation utilising a uniform particle distribution shows a good agreement in the whole energy range.

The general rise of the detector response with energy is related to the increase of the secondary particle generation at higher particle energies, which is dominant in the solid parts of the detector compared to the gas.

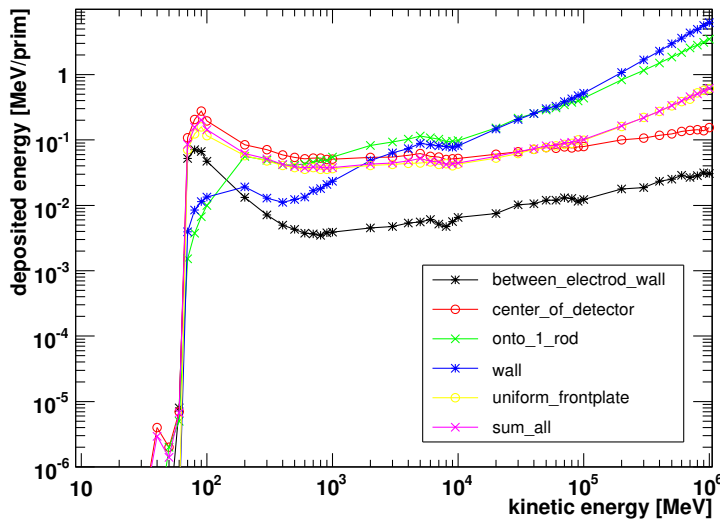


Figure 5.10: The detector response of protons for the irradiation of separate detector parts is compared to a uniformly distributed irradiation.

5.4 Validation Measurements

5.4.1 400 GeV Proton Beam Measurement

A by-product of an experiment at T2 is a cross-check of Geant4 simulations of the SPS Beam Loss Monitor's. Previously performed measurements at T2 were compared to simulations which are described in [33]. The shape of the signal development versus beam position was verified,

but the absolute signal height was not reached in the simulation. Additionally to the cross-check of the detector response simulation is an investigation to gain a better understanding of the measured detector signal development performed. Several simulations, with modified parameters, are compared to the measured detector signal.

Description of the Experiment

The experiment was performed at the transfer line from the SPS to the north area, in front of the T2 target. The detector was mounted vertically on a sliding table in front of the target. Here the beam pipe is cut so that there is a small gap in air (Figure 5.11). The remotely controlled sliding table allowed to move the detector horizontally through the beam. With this method it is possible to perform a scan of the whole cross section of the detector (transversely to the detector axis). The measurement is illustrated in Figure 5.11.

Table 5.3: Beam parameters at the T2 area

Location	North Area - T2
Primary particle	proton
Primary momentum	400 GeV/c
Intensity	$30.0 \pm 0.1 \cdot 10^{11}$

The SPS target intensity at T2 is $30.0 \pm 0.1 \cdot 10^{11}$ protons per pulse at 400 GeV/c. The spill length is approximately 4.8 seconds with a total cycle length of 16.8 seconds (Table 5.3). The beam size (4σ) at the detector is approximately 1.0 cm horizontally ($\sigma_h = 2.5$ mm) and 0.5 cm vertically ($\sigma_v = 1.25$ mm). The estimated beam size has an error of $\pm 15\%$.

As detector, a SPS BLM (parallel plate ionisation chamber) is utilised. It is filled with nitrogen (N_2) at a pressure of 1.1 bar. Between the electrodes a bias voltage of 1500 V is applied to collect the produced charges in the detector. The readout is performed with a charge integrator which is described in appendix A.2.

Measurement

Initially the detector is positioned outside of the beam, the centre of the detector is 160 mm from the centre of the beam. The detector is moved by the remote controlled sliding table in steps of 2 mm through the beam. At about 150 mm the beam touches the detector. The detector remains at each position to perform a couple of acquisitions before it is shifted to the next position, which allows a statistical treatment of the data. The charge integrating electronics is triggered at each accelerator cycle. During each spill the charges created in the detector are integrated and recorded as counts for the corresponding integration time. In the data analysis the counts are converted to number of charges, normalised to the beam intensity [aC/p]. The final measurement results are compared to simulations.

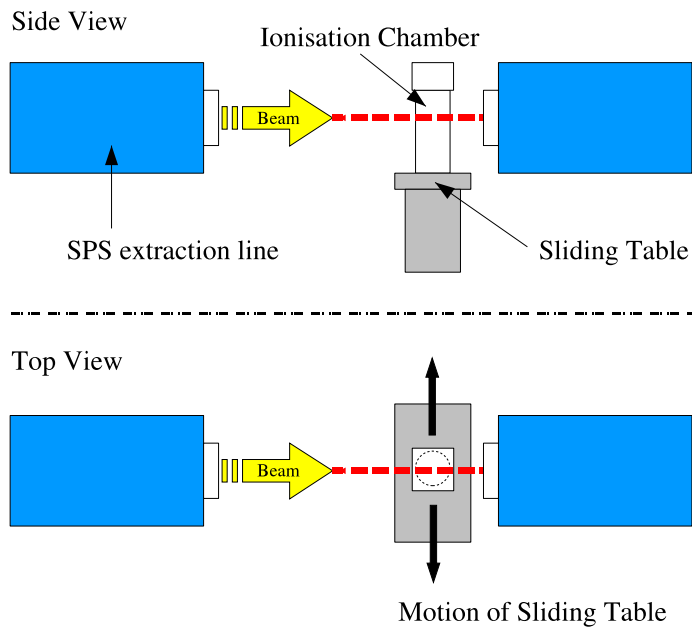


Figure 5.11: Left: Layout of the experiment. Illustrated is the relative movement of the detector to the beam axis. Right: Experimental area T2, the detector is mounted in the gap of the beam pipe. The beam is passing from left to right.

Comparison of Simulation to Measurement

Geant4 versions 4.8.0.p01 and 4.8.1.p01 are utilised to simulate the detector response. The geometry is quite precisely modelled, as described in section 5.2.1. Applied were the predefined physics lists QGSP (Geant4 versions 4.8.0.p01) and QGSP-BERT-HP (Geant4 versions 4.8.1.p01). The default production range cut-off value of Geant4 was set to 0.01 mm (default is 0.7 mm) according to previously described investigations in section 5.2.3.

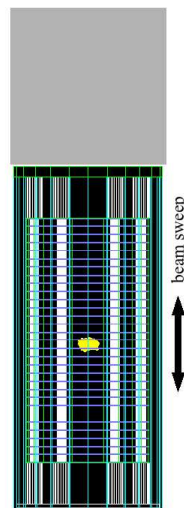


Figure 5.12: The picture shows the Gaussian beam centred between two electrodes. The beam is swept vertically.

The primary proton beam parameters are correspondingly to the measurement implemented. The beam size was estimated by a Gaussian distribution, initially with $\sigma_h = 2.5$ mm and $\sigma_v = 1.25$ mm.

The beam divergence is not taken into account.

As mentioned in the introduction to this section the shape of the signal development versus beam position was verified, but the absolute signal level was not reached in the simulation. The beam size is at the scale of the electrode spacing. The beam position relative to the inner structure is unknown which leads to a large systematic uncertainty. Therefore simulations were conducted in which the beam impacts transversely to the detector axis at the centre of the detector. In several steps the beam centre moved from the exact middle of an electrode to the middle of the distance between two electrodes. These outer positions are the extreme cases for the maximum and the minimum detector response for this simulation. For clarification is the Gaussian beam centred between two electrodes shown in Figure 5.12 and the movement of the beam is indicated by the arrow.

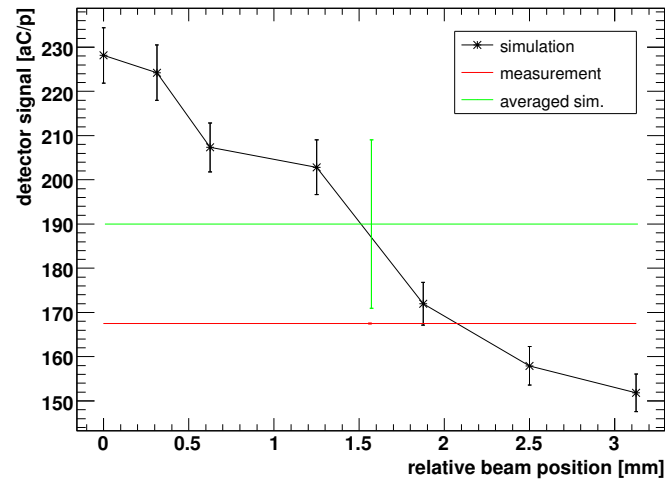


Figure 5.13: Simulations for different beam positions in the range between an electrode and the half-distance to the next electrode. The mean value graph corresponds to the mean value of the simulation results.

The deposited energy in the sensitive volume is scored and converted with the W-factor to the number of produced charges, which is normalised to the number of primary particles.

The simulation results for the stepwise movement of the beam are presented in Figure 5.13 and in Table 5.4. Plotted are the single simulation results, their average and the measurement results. The highest signal is found for the beam position centred on an electrode. From this maximum the signal is continuously decreasing to a minimum at the position at which the beam is centred between two electrodes. The large difference in signal is about 50%. The protons hitting the electrodes (Al has an about 3600 times smaller radiation length than N_2) produce a larger number of secondary particles than protons only passing through the detector gas. These secondaries deposit more energy in the sensitive volume and increase the signal.

The quoted average of the simulation results and its error are derived from the minimum and maximum of the signal height. The difference in signal between the two extreme beam positions is estimated as 4σ which results in an error of $\pm 11\%$. The uncertainties on the measurement are smaller than 2%. The measured detector response lies within the simulation results.

In a second simulation the beam is swept parallel to the electrodes, which corresponds to the performed measurements. In the longitudinal direction of the detector the beam position is set

Table 5.4: Comparison of measurement and simulation performed at the experimental area T2. The simulation results are printed for the two extreme positions of the beam.

	distance *) [mm]	detector signal [aC/p]	statistical error	systematic error
measurement:	—	168.3	0.09	
simulation: (centre)	0	228.1	6.29	
(middle)	3.13	151.8	4.25	
mean value:		190.0		19.08

to a distance of 2 mm from the centre of an electrode. At this distance the measurement and the simulation shown in Figure 5.13 agree best. The beam is shifted in steps of 2 mm parallel to the electrodes across the detector as indicated in the left plot of Figure 5.11. After several iterations with small modifications of the beam size and the beam position relative to the electrode a good agreement between the measurement and simulation was found. The final beam size is 70% of the estimated one ($\sigma_h = 1.75$ mm, $\sigma_v = 0.875$ mm) and the final beam position is 1.7 mm from an electrode. In Figure 5.14 the final comparison of the stepwise measurement and simulation are shown. The inner structure of the detector was aligned to the measurement and the simulation results as illustrated in the plot. The shape of the signal development in the measurement is followed by the simulation within the statistical errors. The inner structure of the detector can be seen in the pattern of the detector signal. At the outer edge of the detector the simulation shows a 2 times lower signal than the measurement. The detector is mounted with 4 supporting rods, which are not implemented in the simulation. The additional material the protons have to pass creates more secondary particles and therefore a larger signal in the measurements. The final simulation was performed with QGSP-BERT-HP of Geant4.8.1.p01.

Conclusion

The agreement between measurements and simulations is good considering the fairly large systematic uncertainties, which arise from the unknown beam position relative to the electrodes. This was verified in the simulation moving the beam stepwise along the longitudinal detector axis centre. If the beam is impinging on an electrode the signal is about 50% larger than if it passes between two electrodes. These two beam positions are the extreme cases. In a final simulation with adjusted beam size and position the measurement results for the experiment in front of the T2 target could be verified. In Figure 5.14 the measurement and simulation results are combined and aligned to the inner structure of the detector which is visible in the pattern of the signal.

The detector signal at the outer walls is a factor of 2 lower in the simulation than in the measurement. In the experiment the detector is mounted with 4 rods, which are not implemented in the simulation. The additional material the beam has to pass creates more shower particles and therefore a higher signal.

This is not a very stringent test for the Geant4 simulation, but the simulations and the measurements are consistent within the systematic errors of about 11%.

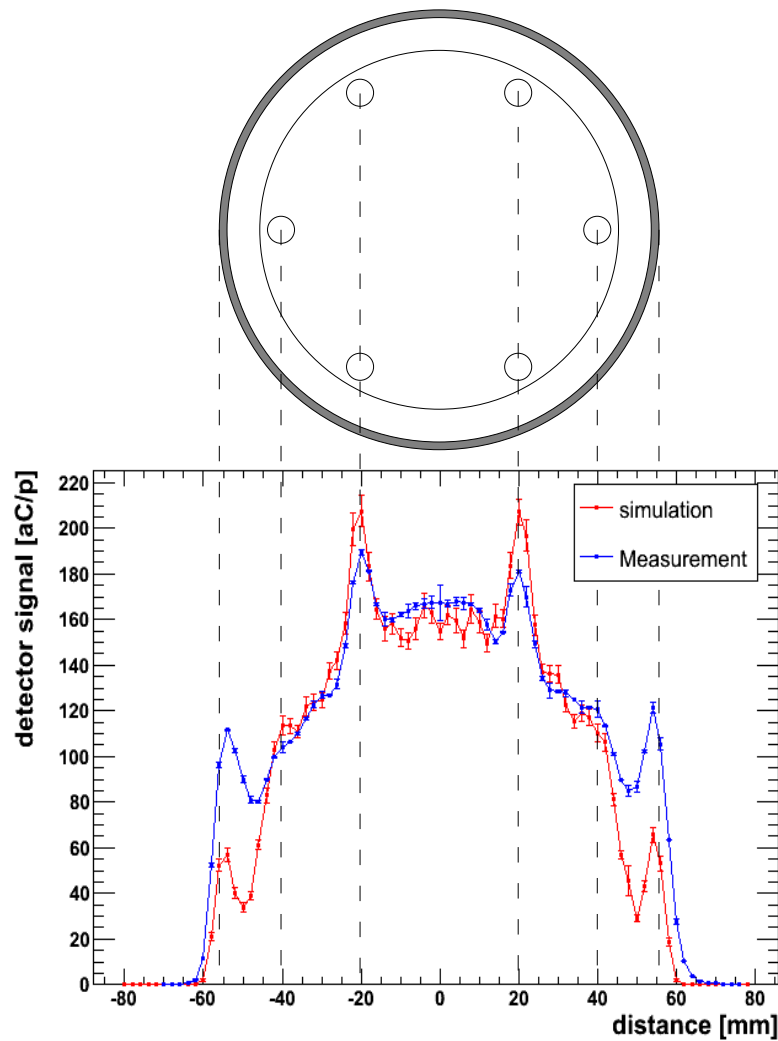


Figure 5.14: Comparison of the measured and simulated detector signal for the 400 GeV/c proton beam experiment at T2.

5.4.2 662 keV Gamma Ray Measurement

With gamma rays a calibration and verification measurements were performed at the SC-RP Calibration Laboratory for Radiation Protection Instruments at CERN. The measurements were conducted with several Caesium 137 (Cs137) sources at various activities and distances. Both detectors, the LHC BLM and the SPS BLM, were utilised in the measurements. The detector was placed on a moveable table at the same height as the Cs137 sources. The dose rate was chosen by changing the distance between the detector and the source. The detector was irradiated perpendicular to its longitudinal axis.

The detector showed a linear behaviour over two orders of magnitude in dose rate ($30 \mu\text{Sv/h}$ to 3mSv/h). The ambient dose equivalent ($H^*(10)$) for each measurement was converted to fluence. $H^*(10)$ is defined as the dose equivalent at a point in a radiation field that would be produced by the corresponding expanded and aligned field in the ICRU sphere at a depth of 10 mm on the radius opposing the direction of the aligned field [34]. The conversion factors can be found in appendix A.3. From fluence one obtains the number of primary photons, which can be utilised to normalise the detector signal. The normalised signal is compared to the simulated detector

response function for gammas and to additional simulation results derived for different irradiation angles.

A comparison of the simulated detector response (described in section 5.3.1) for gamma rays was performed by linear interpolating the simulated detector response at 662 keV from the results at 600 keV and 700 keV. Additional simulations with the exact photon energy of 662 keV and a rotation of the detector between 0° and 10° were also compared to the measurements. In all simulations the layout of the irradiation facility as well as the divergence of the radiation were not taken into account. In all simulation it is assumed that the detector is uniformly irradiated with parallel rays. The irradiation direction is perpendicular to the longitudinal axis of the detector or tilted from this direction by the quoted angle.

Table 5.5: Simulation of the detector response in respect to the irradiation direction. The difference is between the simulation at 0° and the other simulations. The results are in atto-coulomb per photon.

angle [$^\circ$]	simulation [aC/ γ]	error	difference
0	0.270	0.013	0%
0.5	0.320	0.014	16%
1	0.361	0.017	25%
2	0.369	0.017	27%
3	0.391	0.018	31%
4	0.392	0.017	31%
5	0.385	0.017	30%
10	0.385	0.017	30%
average (0-5)	0.361	0.046	25%

In Table 5.5 a comparison of the simulations in respect to the irradiation angle is shown. It is observed that by tilting the detector by only a small angle the response rises. This rise in response is due to the larger amount of material the particles have to pass (electrodes) in the tilted detector and produce thereby a larger number of secondary particles, which can deposite energy in the gas. A maximum difference of 31% between the simulations is found, which is between the perpendicular (0°) irradiation and the one tilted by 4° .

Table 5.6: Gamma ray measurement results and comparison to simulation (10^{-18} Coulomb per photon), errors are statistical. Shown are the simulation response ^{a)} minimum, ^{b)} maximum and ^{c)} average (0° to 5°).

[aC/ γ]	measurement	error	simulation	error	ratio (sim./meas.)	error
SPS BLM ^{a)}	0.42	0.01	0.27	0.02	0.64	0.05
SPS BLM ^{b)}	0.42	0.01	0.39	0.02	0.93	0.05
SPS BLM ^{c)}	0.42	0.01	0.36	0.05	0.85	0.11
LHC BLM	0.40	0.02	—	—	—	—

The closest distance between the radiation source and the detector was 1.68 m. At this distance the maximum angle of 5° between the centre and the edge of the detector is obtained. Therefore, the simulated detector responses between 0° and 5° are averaged and compared to the measurement.

In Table 5.6 the measurement results, the simulated detector response and the ratio between simulation and measurement are shown. The shown simulation results are the derived minimum, the maximum and the averaged (0° to 5°) detector response. All results are quoted in attocoulomb normalised to the photon intensity. The simulation performed with the perpendicular irradiation showed a difference of 36% to the measurement. The detector tilted by 4° showed an agreement of within 7% to the measurement and the average detector response obtained from the simulations differs by 15% from the measurement.

Possible reasons for the difference of 15% include scattering effects of the source encapsulation, the walls, the support of the chamber and the divergence of the radiation, which were not included in the simulation. Additionally, uncertainties arise from the conversion of ambient dose equivalent to fluence. $H^*(10)$ is defined for a sphere in vacuum which introduces uncertainties as the detector is a cylinder in air.

The response for the LHC BLM detector is also shown in Table 5.6. A comparison of the measurement to the simulation was not performed, as there were no response functions available. The responses of the two detector types, the LHC BLM detector and the SPS BLM detector are similar. The SPS detector shows a slightly higher normalised signal, which is due to the larger diameter of the detector.

Considering the simplifications in the simulation and the large systematic error found, the agreement between simulated detector response and measured detector response is good. To achieve a better agreement the experimental setup and the radiation source with the corresponding activity and encapsulation should be implemented in the simulation, which also avoids the conversion from dose to photon fluence.

5.4.3 174 MeV Neutron Measurement

In the LHC the BLM detectors are placed in the tails of hadronic showers. The main part (98%) of these showers is neutral particles (neutrons and gamma rays). The detector was already calibrated with a Cs 137 gamma ray source. At the The Svedberg Laboratory (TSL), at Uppsala University, the detector was exposed to neutrons and was compared to detector response simulations.

The new neutron beam facility at the The Svedberg Laboratory, Uppsala produces high-intensity well collimated and energetically well defined neutron beams with the use of primary protons in the energy range of 25 to 180 MeV (neutron energy range 11 to 175 MeV). An overview of the facility is shown in Figure 5.15. The neutron beam is produced with the reaction ${}^7\text{Li}(p,n){}^7\text{Be}$. Different target sizes are available between 1 and 23.5 mm thickness and a rectangular shape of $20 \times 32 \text{ mm}^2$. The forward cone of the neutron beam is collimated by a cylindrically shaped iron collimator block, 50 cm in diameter and 100 cm long, with a hole of variable size. The proton beam is bent away 45° from the original direction by a magnet onto a heavily shielded water-cooled graphite beam dump [35].

The experiments were performed with an incident proton beam of $178.7 \pm 1.0 \text{ MeV}$ and a maximum beam current on the 23.5 mm thick lithium target of $0.4 \mu\text{A}$. The average energy of the produced neutrons in the peak of the spectrum was 174.3 MeV. A 100 cm long iron collimator with a cylindrical hole of 102 mm in diameter is shaping the beam. For monitoring the neutron intensity a thin-film breakdown counter (TFBC) and two ionisation chamber monitors, one close to the collimator and one at the beam dump are installed [36]. The measurements were normalised to

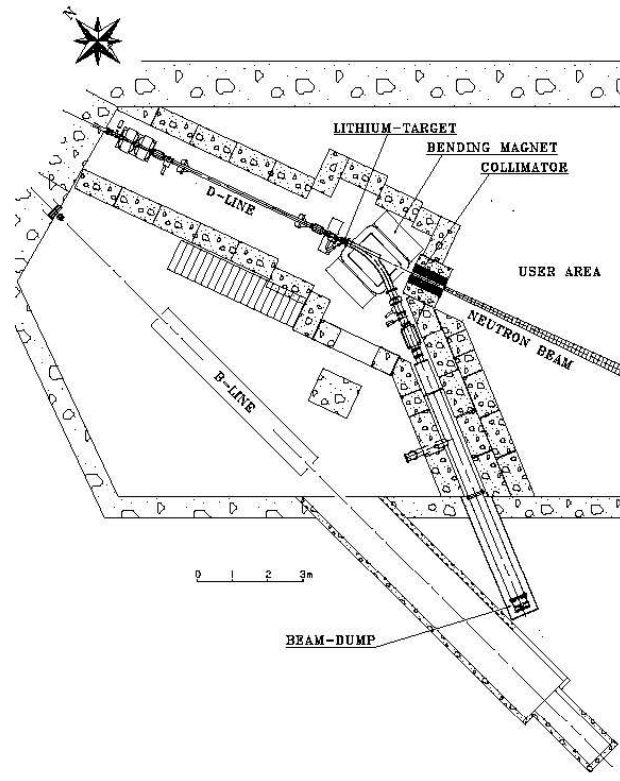


Figure 5.15: Overview of the experimental area at the The Svedberg Laboratory [35].

the ICM raw data (ionisation chamber monitor close to the collimator).

Measurements were performed with an LHC BLM detector and a SPS BLM detector. Each detector was separately measured. In Figure 5.15, one can see the *user area* where the neutron beam is exiting the collimator, this starts about 311 cm downstream of the lithium target [35]. The detector is placed at a distance of about 350 cm from the lithium target. The exact distance is depending on the orientation of the detector and was measured accordingly (closest point of the detector to the Li target). The $1/r^2$ law can be utilised to re-calculate the given fluence from the ICM raw data to any other position. The detector axis was each time horizontally and vertically aligned to the middle of the neutron beam. A layout of the experiment is shown in Figure 5.16. The beam diameter at the detector location was about 11.7 cm.

The measurements were performed with a KEITHLEY 6517 electrometer, controlled via a Math-

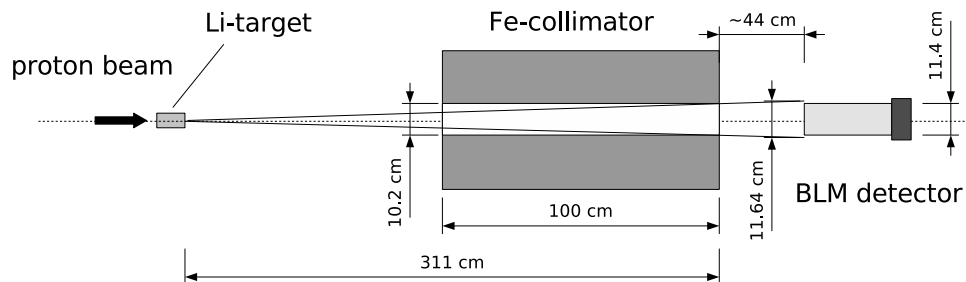


Figure 5.16: Schematic of the experiment.

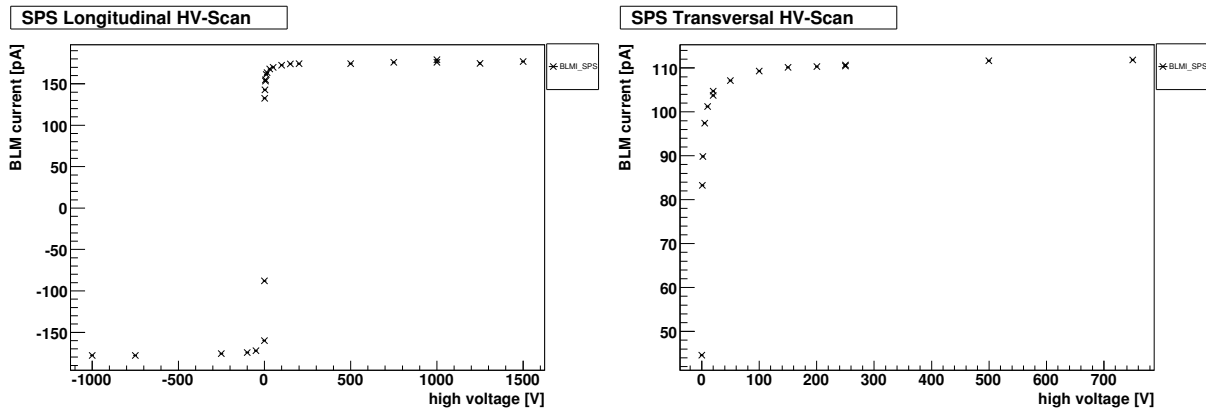


Figure 5.17: High voltage scan for the SPS BLM detector for longitudinal and transverse irradiation. The detector was placed behind another instrument. Therefore, the signal was not normalised to the beam intensity.

Lab program. A FUG HCL 14-3500 was utilised as a DC high voltage power supply, also controlled with the same software. A 100 m long coaxial cable for the signal transmission was installed. The data from the current measurement with the KEITHLEY were written to files. The Institute provided information about the beam intensity.

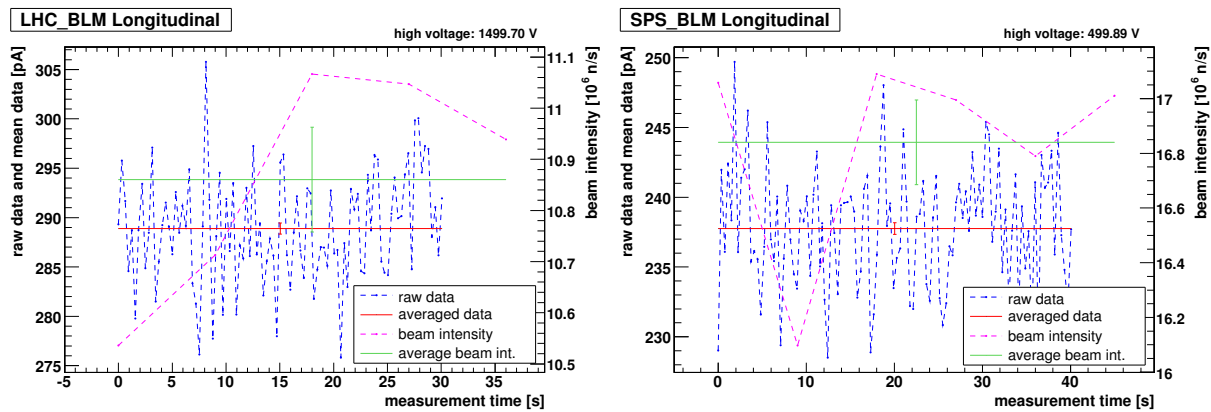


Figure 5.18: Measurement data for the LHC BLM and the SPS BLM at supply voltages of 1.5 kV and 500 V. Shown are the signal raw data, its average and the neutron beam intensity with its average.

For both detectors, the signal versus supply voltage was measured. In the case of the LHC BLM up to 1.5 kV and for the SPS BLM between -1 kV and 1.5 kV. Figure 5.17 shows the high voltage scan for the SPS BLM detector at longitudinal and transverse irradiation. The measurement is not normalised to the beam intensity, because another radiation measurement monitor (RADMON [37]) was placed in front of the detector, so the beam intensity deviated from the provided one.

Above approximately 100 V one can see a linear behaviour. All initiated charges are collected. Below 100 V some of the produced electron-ion pairs are lost due to recombination.

The measurements were normalised to the provided neutron beam intensity, which was calculated for each distance. At a distance of about 350 cm from the Li target the beam already covers the whole front face of the two detectors. To calculate the correct neutron intensity one has to take the irradiated surface of the corresponding detector into account and keep in mind that the neutron intensity measurements with the ICM counter correspond to the peak area in the neutron

fluence spectra. The calculated ratio between the number of neutrons in the peak of the neutron fluence spectra to the total number of neutrons is 0.42. With the SPS BLM a surface of 102 cm^2 for both irradiation set-ups was applied, because the beam has a diameter slightly larger than the detector diameter. For the LHC BLM in longitudinal irradiation direction 63 cm^2 (diameter of the detector is 9 cm) and in transverse direction 93 cm^2 was utilised (no circular irradiation area). The raw data from the KEITHLEY is averaged and normalised to the averaged neutron intensity. The averaged neutron intensity is thereby multiplied by 2.388, which corresponds to the ratio in the spectra. The measurement has an unknown time offset compared to the neutron intensity of the order of 20 seconds. The averaged signals are shown in Figure 5.18. As an example, a measurement with the LHC BLM detector at 1.5 kV and a measurement with the SPS BLM detector at 500 V are shown. The raw data from the KEITHLEY measurement device were averaged over the whole measurement period. The beam intensity that is provided by the institute as neutron flux for 10 seconds is averaged over roughly the same period as the measurements. The signal average is divided by the corresponding neutron intensity. The final results are shown in Figure 5.19 for the LHC BLM detector and in Figure 5.20 for the SPS BLM detector. The final detector response is acquired by averaging the measurements taken with more than 200 V of bias voltage (plateau).

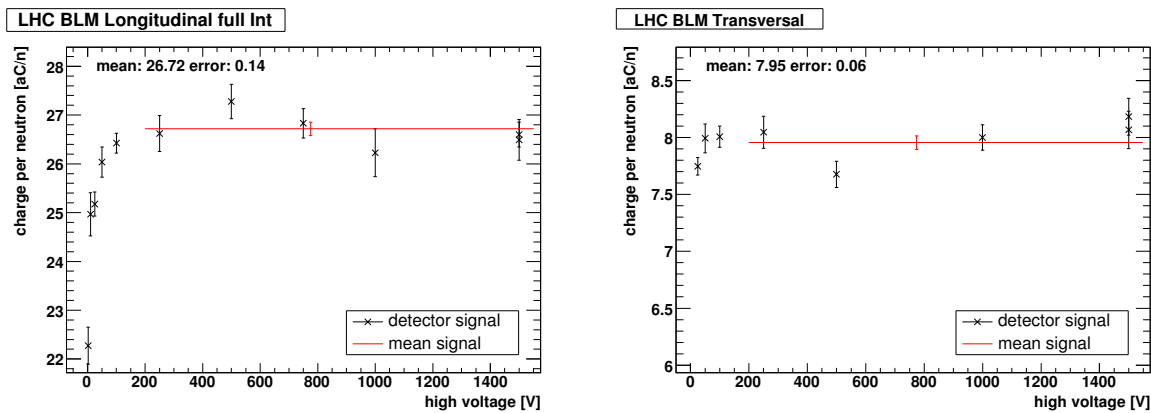


Figure 5.19: High voltage scan for the LHC BLM detector, longitudinal and transverse irradiation. Signal is normalised to the neutron beam intensity.

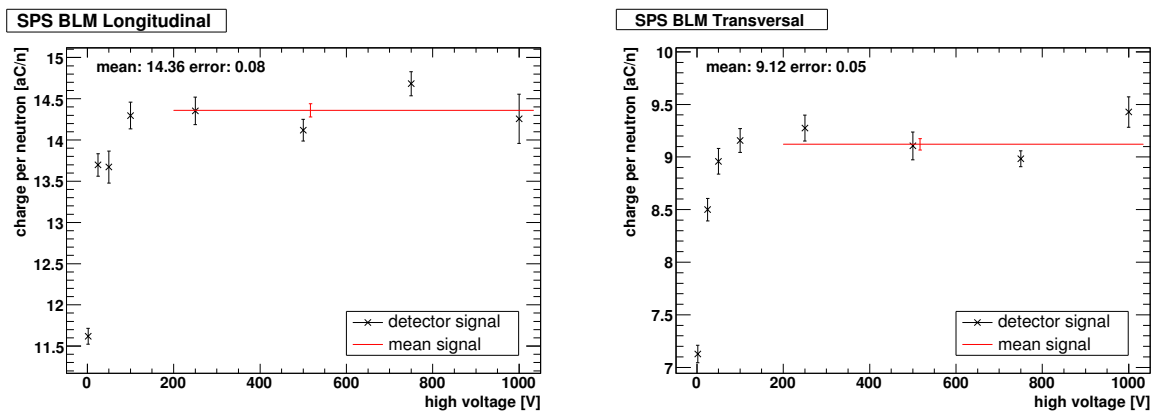


Figure 5.20: High voltage scan for the SPS BLM detector, longitudinal and transverse irradiation. Signal is normalised to the neutron beam intensity.

With the LHC BLM detector additional beam intensity scans were performed. At several beam intensities data at different supply voltages similar as shown in Figure 5.19 were obtained. The neutron intensity was reduced to one half, one fourth and one eighth of the nominal intensity,

with a maximum (nominal) intensity of $1.1 \cdot 10^7$ n/s. A linear fit of the averaged detector signals at different beam intensities is shown in the left plot of Figure 5.21. The associated relative residuals are shown in the right plot. The fitted line crosses, as expected, close to the origin the axis. The residuals are within 1.2% of the linear fit. The systematic error correlated to the beam intensity is estimated to 1%, which provides already a good ratio of χ^2/ndf . Hence, within 1% the linearity of the detector in this intensity range was demonstrated. From the institute a systematic of $\pm 10\%$ on the beam intensity measurement is reported. These two systematic errors are taken into account in the error of the final results.

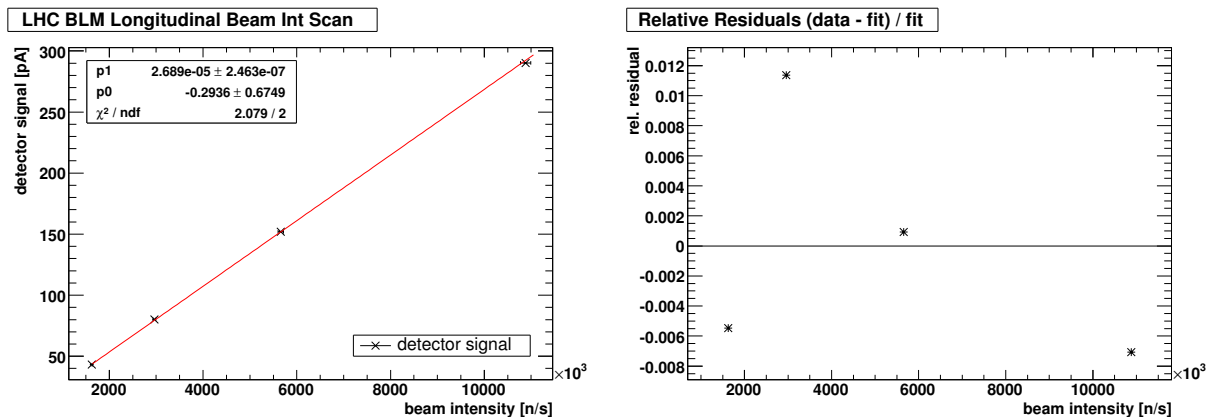


Figure 5.21: LHC BLM detector signals at different beam intensities for longitudinal irradiation. Left: linear fit of the data. Right: relative residuals.

Comparison of Measurements and Simulations

The aim of this experiment was the calibration of the ionisation chamber to neutrons and to verify Geant4 detector response simulations. The simulated detector response was bin-wise multiplied with the neutron spectrum, in respect to the orientation of the detector to the beam. The contribution from gamma rays present in the neutron beam to the signal was neglected in the first analysis. The neutron spectrum for this work was provided by TSL, in form of a calculated spectrum, see Figure 5.22 right. It was shown in reference [38] that the RMS deviation between the calculated and the measured spectrum is less than 7%. The integrated area of the neutron spectrum of TSL is here shown normalised to one giving a probability function which is shown in Figure 5.22 right.

Figure 5.22 left shows the simulated detector response (signal versus kinetic energy of the neutrons). The simulation was performed with the QGSP-BERT-HP physics list of Geant4. In the interesting energy rang between 30 MeV and 180 MeV the detector response increases the a factor of 2. Hence, nearly all neutrons in the spectrum contribute to the signal. The spectrum intensity is dominated by a peak situated a few MeV below the primary proton energy and comprising about 42% of the total number of neutrons.

For each bin in the spectrum the neutron probability function (Figure 5.22 right) was bin-wise multiplied with the corresponding linearly interpolated detector response (Figure 5.22 left), including the statistical error. The result of this convolution is illustrated in Figure 5.23 (left). The final detector signal (Figure 5.23 right) was obtained by integration of Figure 5.23 (left) over the whole energy range. The detector signal is derived in units of Coulombs per neutron. One can see that the contribution due to neutrons from the lower part of the spectrum to the signal is

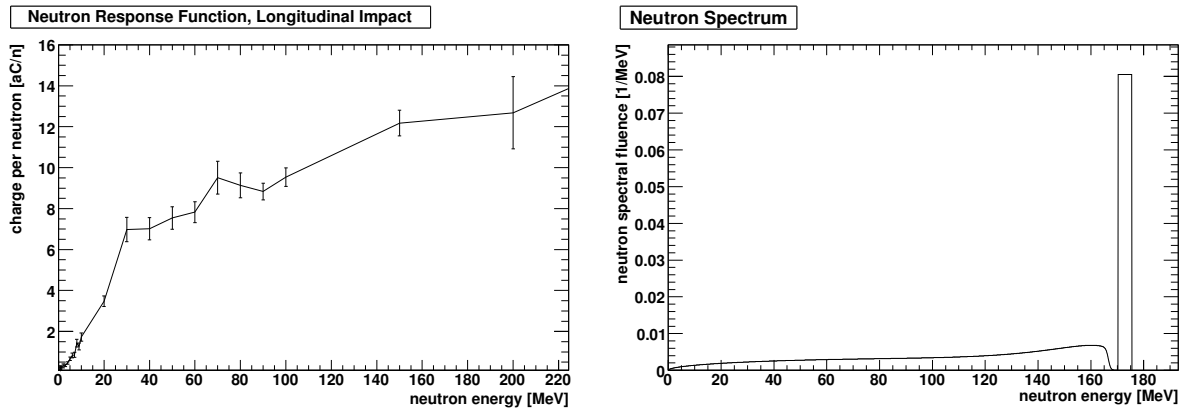


Figure 5.22: Left: Geant4 simulated detector response function (including statistical error) for neutrons, impacting longitudinally to the detector axis. Right: Neutron spectrum of TSL normalised to one.

roughly 50%. That points out the importance of including the lower part of the neutron energy spectrum.

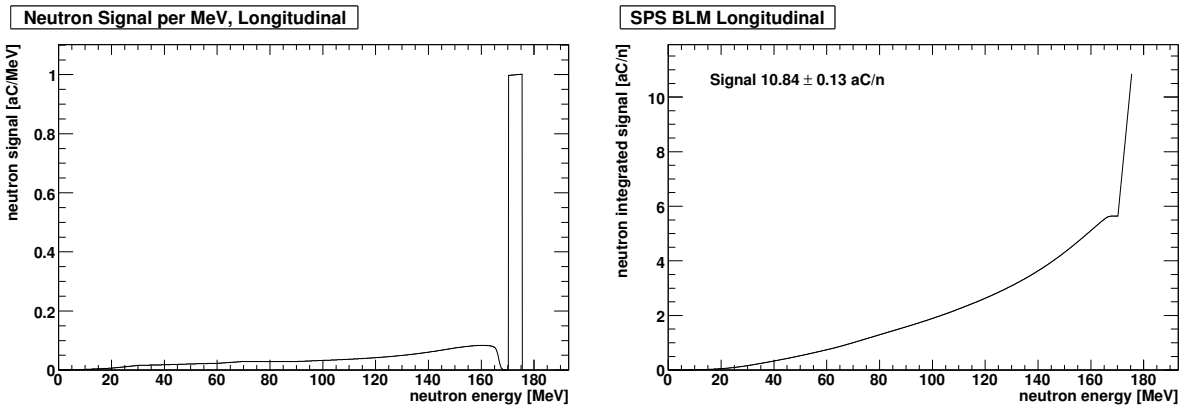


Figure 5.23: Left: Convoluted detector signal, corresponding to each energy bin. Right: Integrated detector signal for longitudinal irradiation.

The same procedure of bin-wise multiplication of the given spectrum with the detector response was applied in the case of transverse irradiation. Figure 5.24 shows in the left plot the simulated detector response and in the right plot the integrated detector signal. A similar behaviour as in the longitudinal case can be observed; the contribution due to low energy neutrons to the signal is about 50%.

The final comparison between measurements and simulations is shown in Table 5.7. Tabulated are the detector responses of the LHC BLM and the SPS BLM detector to neutrons in units of atto-coulomb per neutron. The results of the measurement include statistical errors, a systematic error of 10% from the beam intensity measurements and a systematic error of 1% derived from the beam intensity scan measurements. The LHC BLM detector compared to the SPS BLM detector shows for longitudinal irradiation a 1.85 times higher response. The LHC BLM detector has a 1.3 times larger volume, which does not explain the full difference. Other factors that affect the signals are the neutron intensity change due to the different detector lengths, the attenuation by the detector material itself and the radial beam profile. But only the uncertainties arising from the radial beam profile influence the ratio in the right direction. For the transverse irradiation the LHC BLM detector shows a 13% lower response compared to the SPS BLM detector. The ratio

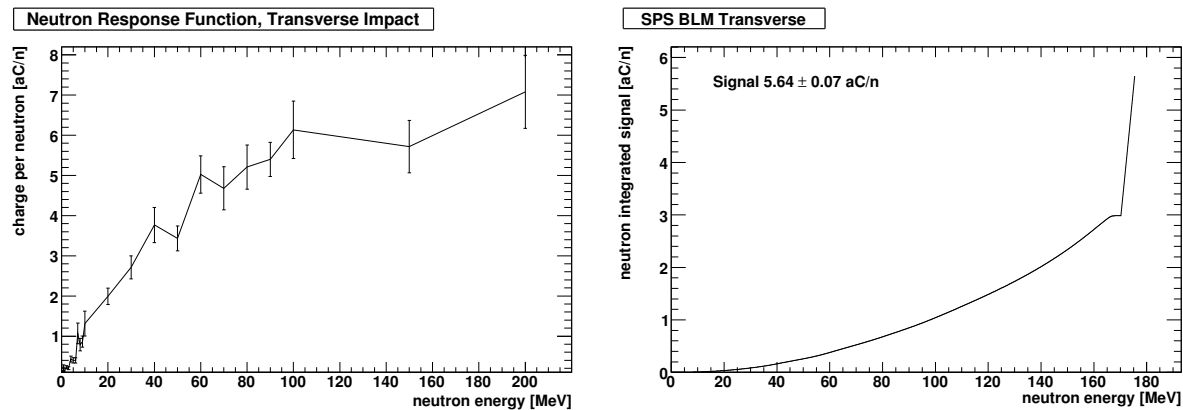


Figure 5.24: Left: Geant4 simulated response function for neutrons impacting transverse to the detector axis. Right: Integration of the convolved neutron spectrum and the detector response function.

for the different irradiated volumes is about 0.75, which again cannot explain fully the difference.

Table 5.7: Measurement results and comparison to simulations. All results are in atto-coulomb (10^{-18}C) per neutron. ^{a)} 15% of gamma ray contribution is taken into account.

[aC/n]	n-impact dir.	Measurement	error	Simulation	error	sim./meas.	error
LHC BLM	longitudinal	26.72	2.69	—	—	—	—
	transverse	7.96	0.80	—	—	—	—
SPS BLM	longitudinal	14.36	1.45	10.84	0.13	0.75	0.08
	transverse	9.12	0.92	5.64	0.07	0.62	0.06
SPS BLM ^{a)}	longitudinal	12.21	1.23	10.84	0.13	0.89	0.09
	transverse	7.75	0.78	5.64	0.07	0.73	0.07

At the moment there is only a simulated detector response for the SPS BLM detector available, which was used in the comparison between measurements and simulations. No fundamental differences are expected for the LHC BLM detector. For the longitudinal irradiation case the ratio of simulation to measurement is 0.75 ± 0.08 . For the transverse irradiation the first comparison of simulation to measurement showed a ratio of 0.41 ± 0.04 (see Table 5.8). In the experiment the detector was not completely covered by the beam for transverse irradiation, which is different to the detector response simulation that covers the whole cross section (including parts that contribute less to the signal). A second simulation was performed with a circularly shaped beam centred on the detector and a beam diameter equal to the detector diameter. The results are in better agreement to the measurements as shown in Table 5.8 with a ratio of 0.62 ± 0.06 . Additionally, the contribution to the signal from gamma rays was not considered. The gamma ray contribution is described in more detail in the following section. In Table 5.7 a gamma contribution ^{a)} of 15% is taken into account. The ratios between simulation and measurement improve from 0.75 to 0.89 for longitudinal irradiation and from 0.62 to 0.73 for transverse irradiation.

Table 5.8: Comparison of the results for two different detector response simulations. In both cases the irradiation is perpendicular to the detector axis. In ¹⁾ ("standard" response simulation) the whole cross section is irradiated, in ²⁾ the beam shape is circular and centred in respect to the sensitive volume, the beam size is equal to the detector diameter. All results are in atto-coulomb (10^{-18}C) per neutron.

[aC/n]	n-impact dir.	Measurement	error	Simulation	error	sim./meas.	error
SPS BLM ¹⁾	transverse	—	—	3.78	0.07	—	—
SPS BLM ²⁾	transverse	9.12	0.92	5.64	0.07	0.62	0.06

Evaluation of the Photon Contribution to the Detector Signal

At a distance of 5 m after the lithium target a measured ambient dose equivalent rate due to electromagnetic radiation of approximately $3.37 \text{ mSv/h} \pm 20\%$ ($9.5 \mu\text{Sv/h/nA} \pm 15\%$ of the proton beam) was found by TSL [39]. The spectrum of the photons was not measured. As the ionisation chambers have an energy dependent response, the photon fluence spectrum was simulated and scaled with the given dose rate to derive the contribution to the detector signal.

At the measurements performed for this work the BLM detector was placed at about 3.5 m from the lithium target. Taking the inverse-square law ($1/R^2$) for the dose re-calculation into account, we obtain a dose rate of 6.88 mSv/h at the detector location of 3.5 m. A part of the photon fluence spectrum is due to bremsstrahlung. There is also a contribution from electron capture-x-ray decay of ${}^7\text{Be}$ with a photon energy of $E_{\text{photon}} = 0.478 \text{ MeV}$ and a gamma-ray contribution from the decay of excited ${}^7\text{Be}$ states. The photon fluence spectrum was not measured and is therefore simulated with Geant4.

The dose (ambient dose equivalent $\text{H}^*(10)$) is converted to KERMA (kinetic energy released in matter, KERMA in air K_a) and subsequently to fluence (number of photons). The conversion coefficients from $\text{H}^*(10)$ to K_a are printed in Table A.3 ([34], table A.21). Conversion coefficients from KERMA to fluence are printed Table A.2 ([34], table A.1). The coefficients are only given up to 10 MeV photon energy. For higher energies the $\text{H}^*(10)$ to K_a conversion coefficient was assumed to be constant at 1.1. The K_a to ϕ conversion coefficient was linearly interpolated by:

$$\frac{K_a}{\phi} = 1.9853 \cdot E_{\gamma}[\text{MeV}] + 4.1767. \quad (5.5)$$

The fluence spectrum of gamma rays exiting the lithium target and entering the detector at a distance of 2 mm and 3.5 m from the target was simulated with Geant4. The collimator was implemented as a total absorber. The position at 2 mm was chosen to have better statistics in the whole energy range of the spectrum. At 3.5 m the high energetic part, above 20 MeV, is not visible anymore due to low statistics. A geometrical tracking of the particles from the 2 mm position up to 3.5 m and 5 m from the target confirmed this. The ratio between the spectrum at 3.5 m and 5 m is about 2.3 ± 0.5 which is consistent with $\frac{5^2}{3.5^2} = 2.0$. In figure 5.25 the fluence spectra at 2 mm and 3.5 m are compared. To estimate the gamma ray contribution to the total detector signal the photon fluence spectrum at the actual detector position (3.5 m) was binned in 10 logarithmically equally spaced bins. The bin content represents the number of photons per primary proton per square centimetre.

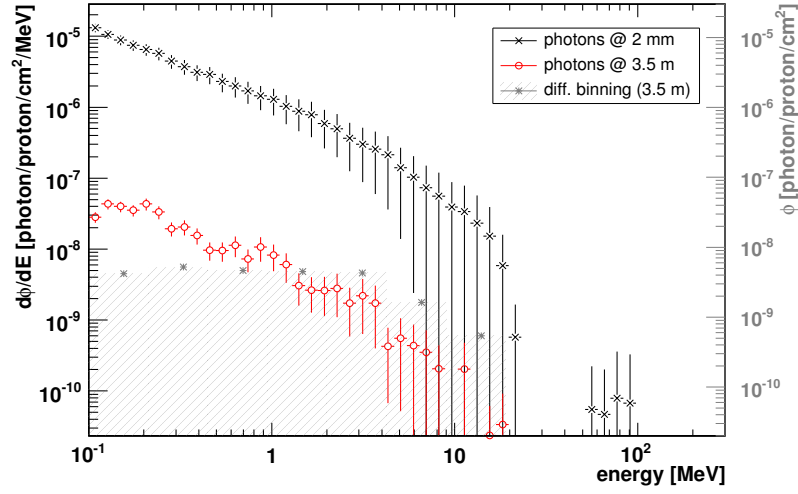


Figure 5.25: Comparison of simulated photon spectra at 2 mm and at 3.5 m after the Lithium target for 179 MeV primary protons in units of [photon/proton/cm²/MeV]. Spectrum at 3.5 m also shown with a different binning and in units of [photon/proton/cm²].

In order to estimate the photon contribution, the simulated photon fluence spectrum is scaled to the measured dose rate $H^*(10)$ as follows. The ambient dose equivalent $H^*(10)$ is expressed as an integral over the photon energy:

$$H^*(10) = \int h^*(E) dE \quad (5.6)$$

$h^*(E)$ is correlated to the photon fluence spectrum by

$$\varphi(E) = \frac{h^*(E)}{f_1(E)f_2(E)} \quad (5.7)$$

where $f_1(E)$ and $f_2(E)$ are the previously mentioned conversion factors from $H^*(10)$ to KERMA and further to fluence. The photon fluence spectrum $\varphi(E)$ is proportional to the photon fluence spectrum per proton $\Psi(E)$ shown in Figure 5.25, α being the proportional factor.

$$\varphi(E) = \alpha \cdot \Psi(E) \quad (5.8)$$

This proportionality factor represents the proton beam intensity and is therefore derived from the total dose $H^*(10)$ by:

$$H^*(10) = \int \varphi(E)f_1(E)f_2(E) dE = \alpha \int \Psi(E)f_1(E)f_2(E) dE \quad (5.9)$$

$$\alpha = \frac{H^*(10)}{\int \Psi(E)f_1(E)f_2(E) dE} \quad (5.10)$$

Dependent on the dose rate, α is derived for 6.88 mSv/h to $4.2 \cdot 10^{16}$ proton/h which is compared to the proton beam intensity of $8 \cdot 10^{15}$ by a factor of 5.3 different. This difference is mainly from uncertainties in the simulation of the spectrum and from the utilised $H^*(10)$ conversion factors. The contribution S to the detector signal is calculated, as shown in equation 5.11, by bin-wise multiplication of the photon fluence spectrum per proton with the simulated detector response function $R(E)$ and a multiplication of the deduced proportional factor α .

$$S = \alpha \int \Psi(E)R(E) dE \quad (5.11)$$

The numerical integration is performed at the bin centres of the spectrum. The detector response function for gammas was linearly interpolated for the corresponding energy.

The absolute contribution of the gamma rays to the signal is about 36 pA for 6.88 mSv/h. Compared to the total detector signal of about 240 pA this corresponds to 15%.

Table 5.9: Calculated detector response due to gamma rays. The gamma ray fluence spectrum was binned in 10 logarithmically equal space bins. Printed are the centres of the bins, the contribution of each bin to the total signal for the given dose rate, the relative contribution to the signal in percent and the percentage of the spectra contribution of each bin.

E_γ [MeV]	signal [pA] @ 7.35 mSv/h	rel. contribution [%]	spectral ratio [%]
0.16	0.61	1.7	16.7
0.33	2.10	5.9	20.9
0.7	1.87	5.2	18.6
1.48	8.58	23.9	18.1
3.12	14.42	40.1	17.1
6.61	1.60	4.5	6.5
13.99	6.75	18.8	2.2
29.6	0	0	0
62.63	0	0	0
132.53	0	0	0
sum	36	100	100

In Table 5.9 the calculated detector response due to the simulated photon fluence spectrum is summarised. The photon spectrum was binned in 10 logarithmically spaced bins. The centre of the bins refers to the energy of the photons. The contribution of each bin to the total detector signal is shown for the given dose rates of 6.88 mSv/h. In the third column the relative contribution of each bin to the total signal is printed. The last column shows the percentage of photons in the corresponding energy bin of the spectrum.

Comparing the detector signal for each energy bin to the relative number of photons in the corresponding energy bin shows that the main contributing part of the spectrum to the detector signal is above 1 MeV. The photon fluence spectrum above a few MeV shows large statistical uncertainties and therefore the derived contribution to the detector signal is a rough estimate. Other calculations for different spectra and binnings have been performed and showed similar results.

5.4.4 Mixed Radiation Field Measurement

Depending on the beam loss location, the LHC beam loss monitors (BLM) will be exposed to different mixed radiation fields. Therefore the monitors have to be calibrated for different particle types and at different energies. To be able to do this, controlled conditions are necessary which are available in the CERN-EU High Energy Reference Field Facility target area (CERF) at CERN [40]. The measurements were compared to a combination of Geant4 [22] and FLUKA [41][42] simulations.

Description of the Experiment

The experiment was performed at the CERF target in the secondary SPS beam line H6. Previous experiments at this target were performed by the CERF group. These experiments will be referred in this document as "CERF experiment". It is described in the report [43]. In this experiment six ionisation chambers (PMI detector, manufactured by PTW, type 34031) were positioned around a copper target so that they are exposed to different mixed particle fields. The secondary particle shower varies strongly in its mean energy. This experiment was compared to FLUKA simulations. These measurements and the simulations are utilised as a reference. A part of the FLUKA simulation is reused as input to the Geant4 simulation. Due to the unavailability of LHC BLM type ionisation detectors SPS BLM's had to be utilised. In Figure 5.26 a schematic layout of the H6 target area is shown. In the top view (Figure 5.27) the detector positions relative to the copper target can be seen. The placement was similar to the CERF experiment, except at position 2 where no detector could be placed. A mixed hadron beam (see Table 5.11) impacts the cylindrical copper target (length: 50 cm, diameter: 7 cm). This leads to an irradiation of the five detectors with secondary particles produced in hadronic and electromagnetic cascade processes. All monitors are mounted at the same height as the copper target.

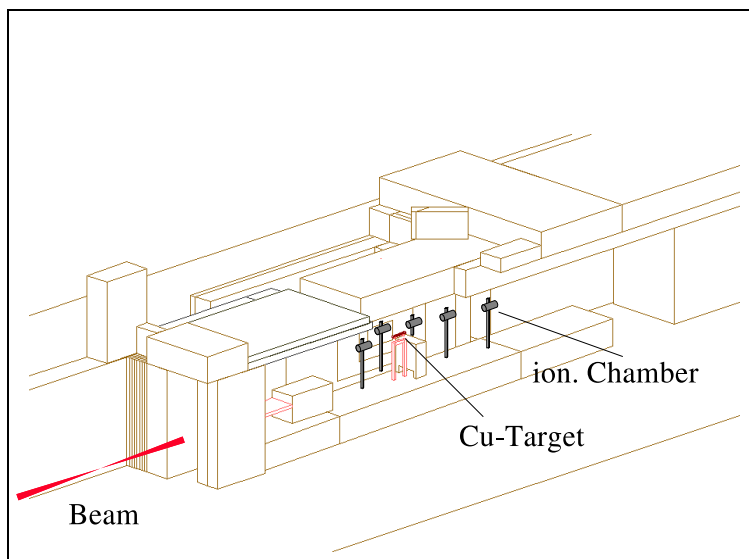


Figure 5.26: Layout of the CERF-target area (H6). The experimental area is inside a thick concrete shielding. The front concrete wall is not shown. The mixed hadron beam arrives from the left side [43].

The SPS beam loss monitors are labelled so that detectors with lower position numbers experience the lower energetic part of the cascades. The higher the position numbers the higher the contribution of high energetic particles. Detector 1 is therefore exposed to the back-scattered low

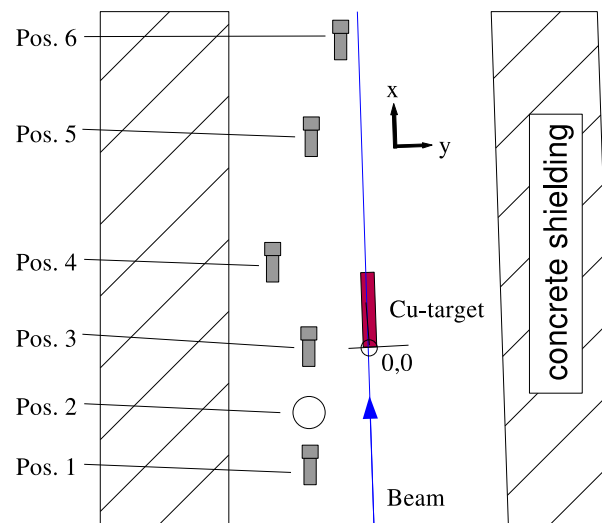


Figure 5.27: Top view of the CERF-target area (H6). The beam loss monitors are positioned around the Cu target. At position 2 no detector could be mounted.

energetic part of the hadronic and electromagnetic processes. The opposite is true at detector 6, which is close to the primary beam axis. It is irradiated by forward scattered particles, which are high energetic cascade products. The exact positions of all chambers are quoted in Table 5.10.

Table 5.10: Position of the detectors. Reference is the impacting point of the hadron beam on the copper target.

position	x [cm]	y [cm]	position	x [cm]	y [cm]
1	-100.5	-49.5	4	70.5	-80.3
2	-50.5	-49.5	5	176	-47.5
3	0	-50	6	250	-22.5

Beam Parameters

From the SPS the proton beam is extracted to the TCC2 area, where the 400 GeV/c proton beam hits a beryllium target (T4). The secondary charged particles with a momentum of 120 GeV/c are transported into the North Hall onto the CERF target. There, these secondary particles act as an incident beam on the copper target to produce a mixed radiation field. The parameters of the beam utilised in the experiment are tabulated in Table 5.11.

The time structure of the arriving beam at the CERF target is defined by the SPS beam extraction. The acceleration of the protons in the SPS takes 12s. It is followed by a 4.8s long extraction onto the T4 beryllium target in the TCC2 area. More information on the beam shape and beam profile can be found in [43].

An air ionisation chamber placed in the beam 8.5 m upstream of the target, the PIC counter, was utilised to monitor the beam intensity. The values given by this counter are the "PIC counts". One PIC count corresponds to a beam intensity of $23 \cdot 10^3$ particles, with an uncertainty of $\pm 10\%$ [43].

Table 5.11: Mixed hadron beam coming from the T4 beryllium target. These parameters refer to a position 8.5 m upstream of the copper target’s front face.

Momentum	120 GeV/c		
Intensity	up to $9.5 \cdot 10^7$ hadrons (4130 PIC) per 16.8 s		
Gaussian beam shape approximation at 4000 PIC	$\sigma_{horizontal}$	1.3 cm	
	$\sigma_{vertical}$	1.0 cm	
Particle composition in %	π^+	protons	K^+
	60.7	34.8	4.5

Description of the Detector

The detectors utilised in the experiment are SPS beam loss monitors. These are similar in design to the LHC type BLMs, which are nitrogen filled ionisation chambers. A comparison and a detailed description of the two detectors has been given in chapter 2.

During the experiment the chamber was operated at a voltage of 1500 V. The charges produced inside the sensitive volume (see subsection 5.2.1) are measured with a charge integrator. The charge integrator is the one utilised for the SPS BLM system readout which is described in appendix A.2. The integrator electronics for the SPS BLM measurements is triggered accordingly to the accelerator cycle. In this experiment, however, the measurement was triggered by observing the beam spill. One acquisition lasts for 7 seconds, including a full extraction onto the target of 4.8 s. One detection count corresponds to a collected charge of 10.74 pC.

Particle Spectra at different Detector Positions

Derived from FLUKA simulations are the particle fluence spectra at the different detector positions. Figure 5.28 shows in 6 graphs the photon, neutron, charged hadron and electron/positron fluence for each detector positions. For each of the graphical representations a logarithmic binning of the particle’s kinetic energy on the abscissa versus fluence per unit lethargy on the ordinate (see section A.4) is utilised. The unit of fluence per unit lethargy is cm^{-2} (per primary beam particle hitting the copper target). All particles arriving at a certain position are registered and artificially stopped. These spectrum were provided by the CERF team and are described in more detail in [43].

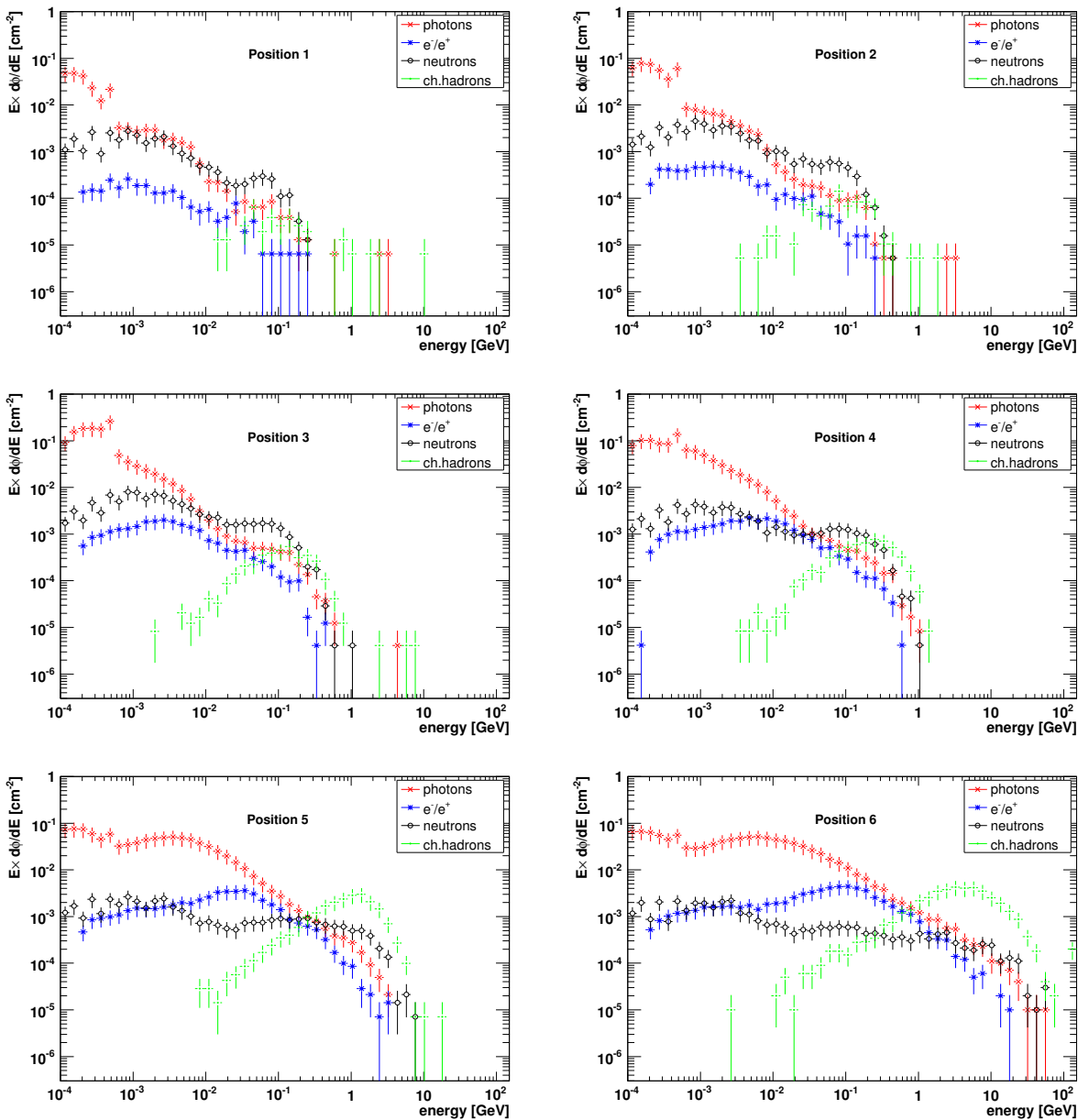


Figure 5.28: The Particle fluence spectra per primary particle onto the copper target at different detector positions were simulated with FLUKA and utilised as input to Geant4 [43] (lethargy representation).

Description of the Simulation

The Monte Carlo code Geant4 8.0 – released 10 February 2006 (patch-01) is utilised to simulate the detector response. To describe the physics processes in the simulation the predefined physics list QGSP is taken. The Geant4 default production range cut-off value of 0.7 mm was modified to 0.01 mm (see section 5.2.3).

The FLUKA simulations, described in [43], are in good agreement with the PMI detector measurements (within 10%, see Figure 5.32). Due to this good agreement and the complex geometry of the H6 experimental area, the simulated FLUKA spectra were utilised as an input to the

Geant4 detector response simulations.

With FLUKA the irradiation of the copper target with a primary hadron beam was simulated. At the positions of the PMI detectors all arriving particles were registered and their transport artificially stopped. All particle properties were recorded (detector position, particle type, particle position, particle direction and kinetic energy). The fluence spectra for the various detector positions are shown in Figure 5.28.

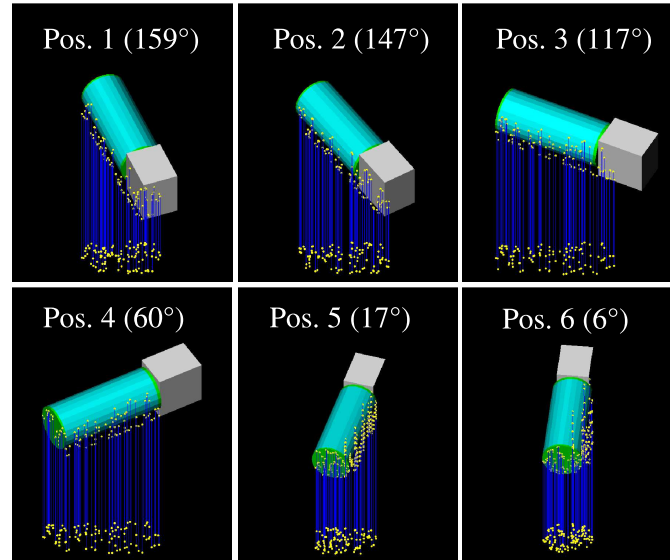


Figure 5.29: Illustration of the different detector positions in the simulation, seen from above the centre of the target under an angle of 45° . The particles are impinging parallel with an uniform distribution.

This data is further processed to act as a input to Geant4. Each detector was separately simulated. The spectra were produced for the PMI detector, which is different in size to the SPS BLM. The PMI detector is a vertical tube with a height of approximately 30 cm and a diameter of 20 cm, in respect to the SPS BLM which is a horizontally mounted tube with a length of 22 cm and a diameter of 12 cm. Therefore, the particle position and direction could not be taken into account. Only the information of the particle type and its kinetic energy was utilised. Each detector was irradiated with a corresponding uniform distribution of these particles over the whole cross section. An illustration of this simplification is shown in Figure 5.29. A side effect of this procedure is an increase of the particle density in the Geant4 simulation compared to the FLUKA simulation and an increase in uncertainty of the results. To compensate for the density increase the relative area ratios between PMI and SPS detector at each detector position had to be taken into account in the final results. Table 5.12 shows the relative area ratios for each detector position corresponding to its rotating angle (rotating angle is relative to the centre of the copper target and the beam downstream direction).

Due to applying a uniform random particle position distribution instead of the exact particle positions and directions some of the particles in this simulation will travel a longer or shorter distance in the detector. To reduce this effect the whole spectra was run 10 times in the Geant4 simulation with different initial random seeds.

The detector response is obtained as described previously. The sum of the deposited energies in the sensitive detector volume is normalised to the number of primary particles onto the copper target, which were initialised in the FLUKA simulation (6000 primaries). With the W-factor for

Table 5.12: Corresponding area ratio between PMI and SPS detector in respect to the rotation angle. The rotation angle is between the beam axis and the detector position in respect to the target centre.

position	A_x/A_{PMI}	area ratio	rot. angle
1	A_1/A_{PMI}	2.88	159°
2	A_2/A_{PMI}	2.33	147°
3	A_3/A_{PMI}	1.83	117°
4	A_4/A_{PMI}	1.85	60°
5	A_5/A_{PMI}	3.16	17°
6	A_6/A_{PMI}	4.46	6°

nitrogen (35 eV per electron-ion pair [19]) the number of charges is calculated. At the CERF experiment the results are compared in counts. Thus by applying the relation that one detector count corresponds to 10.74 pC the final detector signal is derived. This result can be directly compared with the measurements.

Detector Response at different Beam Intensities

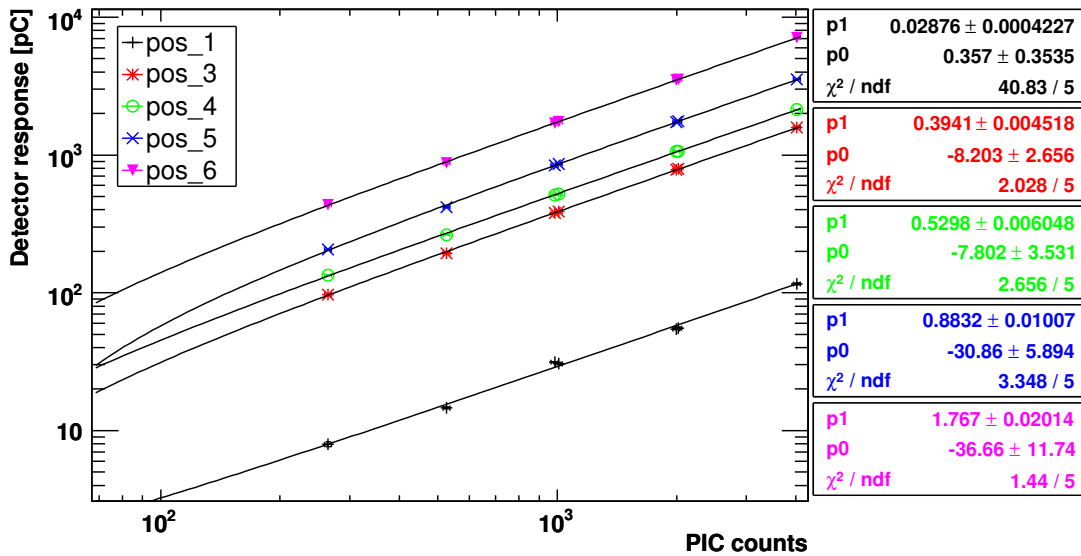


Figure 5.30: Detector response at different beam intensities (PIC counts). Linear fits applied to all detector signals. An error of 2% on the PIC counts was utilised.

Measurements performed at various beam intensities are shown in Figure 5.30. The detector readings (raw data) from the charge integrator given in counts are processed by, first subtracting the background readings and second by normalising to the beam intensity. The background level was measured after each series of measurements (without beam). The counts are converted to produced charges in the chamber (pC) by considering the correct amplification factor of the charge amplifier. A 1.5 V battery was connected to one of the input channels. The constant signal from the battery was amplified with a factor of 10 and utilised as a calibration point. The final results from the other channels are normalised to the channel connected to the battery and to a

volume of 1 dm^3 (the SPS detector is considered to have a sensitive volume of 1.18 dm^3).

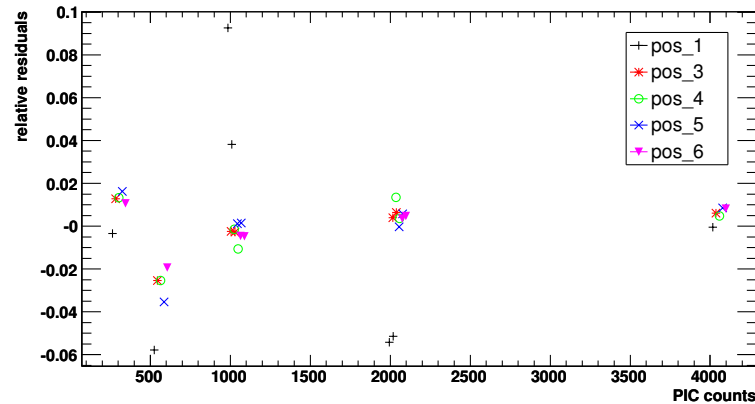


Figure 5.31: Relative residuals $((measurement - fit)/fit)$ for the different detectors versus beam intensity in PIC counts.

Each point in Figure 5.30 represents the average over a set of measurements (between five and eleven). In the plot the fit parameters and the Chi-square per degree of freedom (ndf) for a linear fit are shown. A ratio for χ^2/ndf of 1 is considered as a “good” fit. In a first analysis of the data the averaged measured beam intensities was utilised for the normalisation of the individual measurements. The statistical error of the average beam intensity was below 0.5% and χ^2 over number of freedom ratios between 9 and 75 were derived. These high ratios show that the statistical variation of the PIC normalised detector measurements is not sufficient to explain the estimated errors for getting a realistic expectation value of χ^2 over number of freedoms. Therefore, an estimated error of 2% due to unknown uncertainties was applied to the beam intensities. Detector 3 to 6 show a χ^2/ndf below one which indicates that the applied error of 2% is to high, but the χ^2/ndf for detector 1 is still larger than 8. This behaviour is not understood.

With the applied estimated error the ionisation chamber signal shows a roughly linear relation to the beam intensity in the range of 200 to 4000 PIC counts which corresponds to $4.6 \cdot 10^6$ to $9.2 \cdot 10^7$ primary particles on the copper target.

In Figure 5.31 the relative residuals are shown. They are calculated by subtracting the fitted signal from the measured one and normalisation to the fit function. The results for the different detectors are separated on the beam intensity axis for better visibility. The maximal deviation observed is at detector 1 of below 10%. This matches the larger ratio of χ^2/ndf from the fit. The maximum relative residuals for the other detectors are below 4%, for beam intensity readings below 1000 PIC. The beam intensity is adjusted with collimators, which changes also the beam size. Uncertainties arising from different beam sizes were not investigated.

Detector Response at a PIC Count of 4000

The convention to compare the measured and simulated results at a level of 4000 PIC counts, performed in the CERF experiment, is kept. All measurement and simulation results are normalised to a PIC count of 4000. That corresponds to a beam intensity of approximately $9.2 \cdot 10^7$ hadrons onto the copper target per SPS extraction. To compare the measurement and simulation results from the CERF experiment to the ones described in this thesis all results were converted to pC and normalised to a detector volume of 1 dm^3 . The sensitive volume of the PMI detector

is 3079 cm^3 . At the CERF experiment one count from the system readout corresponded to a collected charge of 1 pC . The sensitive volume of the SPS BLM detector is about 1180 cm^3 (see section 5.2.3).

Table 5.13: Measured counting rate deviation for different misalignment of the detector position perpendicular to the beam axis [43].

position	Counting rate deviation for +3cm [%]	Counting rate deviation for -3cm [%]	Average counting rate deviation for $\pm 3\text{cm}$ [%]	Average counting rate deviation for the assumed misalignment of $\pm 1\text{cm}$ [%]
1	1.66	-1.4	1.53	0.51
2	0.55	0.48	0.52	0.17
3	-6.54	8.4	7.47	2.49
4	-7.29	5.51	6.4	4.27
5	-4.84	4.64	4.74	3.16
6	-19.17	16.25	17.71	11.8

At the CERF experiment (with PMI detectors), the influence of the chamber position inaccuracy on the measurements was investigated. This investigation was only performed for the Y-direction (Figure 5.27). The distances in the X-axis were well known. Table 5.13 shows average counting rate deviations for a misalignment of $\pm 3\text{ cm}$ at position 6 of 17.71% . This is due to the fact that the detector at position 6 is close to the primary beam axis and therefore more sensitive to any displacement. The high-energy particles are close to the primary beam and their number decreases rapidly with radial distance. For the other positions this error is in the range of a few percent. Because of time constraints the misalignment investigation was not redone for the measurements with the SPS detector. It is assumed that the behaviour of both experiments is similar. In the error calculation a misalignment of $\pm 1\text{ cm}$ was taken into account.

The results of the measurements with the PMI detector and with the SPS BLM are shown in Table 5.14 and compared to each other. The error calculation for the SPS detector measurements takes a beam intensity measurement error of 10% , the mentioned misalignment error and the statistical error into account. The statistical error is below 1.5% .

The two measurements differ most at the outer positions. The SPS BLM at position 1 detects about 32% less than the PMI detector. At the lower numbered positions the spectra of the arriving particles are shifted to lower energies (Figure 5.28). Due to the different wall materials the energy cut-off for particles, which contribute to the signal, is for the SPS detector higher. The PMI detector is mainly made of polyethylene compared to stainless steel in the SPS detector. At position 5 the SPS BLM shows a signal 1.32 times higher than the PMI and at position 6 a signal 2.05 times higher. Again this difference in signal amplitude is due to the different construction materials utilised. The secondary electromagnetic shower production depends partly on the atomic number to atomic mass ratio and the density of the material. This leads in the case of the SPS BLM (stainless steel) to a larger number of secondary particles in the gas and therefore to a higher energy deposition. At position 3 and 4 the two detector signals are similar, the two effects apparently cancel each other.

As mentioned before, there was no SPS monitor mounted at detector position 2.

Table 5.14: Produced charges per spill at a PIC count of 4000 for the PMI and the SPS detector normalised to 1 dm³.

position	PMI detector [pC]		SPS BLM [pC]			ratio	
	measurement	error	measurement	stat. error	total error	SPS/PMI	error
1	168.89	16.89	115.33	1.63	11.66	0.68	0.10
2	465.09	46.77	—	—	—	—	—
3	2009.74	206.56	1577.75	0.84	162.59	0.79	0.11
4	2360.51	258.53	2121.52	1.76	230.69	0.9	0.14
5	2671	283.21	3531.98	1.33	370.42	1.32	0.20
6	3458.27	537.84	7091.16	2.98	1096.82	2.05	0.45

Simulated Detector Response at a PIC Count of 4000

The simulation of the detector signals is performed as described previously. In Table 5.15 the simulated detector signals with FLUKA and Geant4 are compared. The ratio between the two shows the same behaviour as in the measurements. At lower numbered detector positions the simulated SPS detector shows a 1.9 times lower signal than the PMI detector. At position 5 and 6 the simulation with Geant4 produces a higher signal than the one performed with FLUKA. This gives confidence that the two simulations work reliably.

Table 5.15: Produced charges for a PIC count of 4000 in the FLUKA and the Geant4 simulation, respectively to the utilised detector (PMI, SPS).

position	FLUKA simulation [pC]		Geant4 simulation [pC]		ratio	
	PMI detector	error	SPS BLM	error	SPS/PMI	error
1	168.89	3.9	91.13	11.09	0.54	0.07
2	479.38	12.99	281.22	18.9	0.59	0.04
3	2016.24	22.09	1656.38	57.57	0.82	0.03
4	2550.18	19.49	2386.62	68.09	0.94	0.03
5	2874.96	37.67	3943.99	73.12	1.37	0.03
6	3236.12	24.68	6495.5	55.46	2.01	0.02

Comparison of Measurement and Simulation

The CERF experiment results and the corresponding FLUKA simulations are plotted in Figure 5.32. The agreement of the simulation to the measurement is within the uncertainties. The maximum difference is at position 4 of about 8%.

The consistency of the Geant4 simulation with the measurement is less precise as shown in (Figure 5.33 and Table 5.16). A few simplifications described previously were applied to the simulation. Despite these assumptions the results of the simulation are still within the uncertainties, which are dominated by the measurement.

In Table 5.16 are the measurement results, the simulation results and a comparison of the two

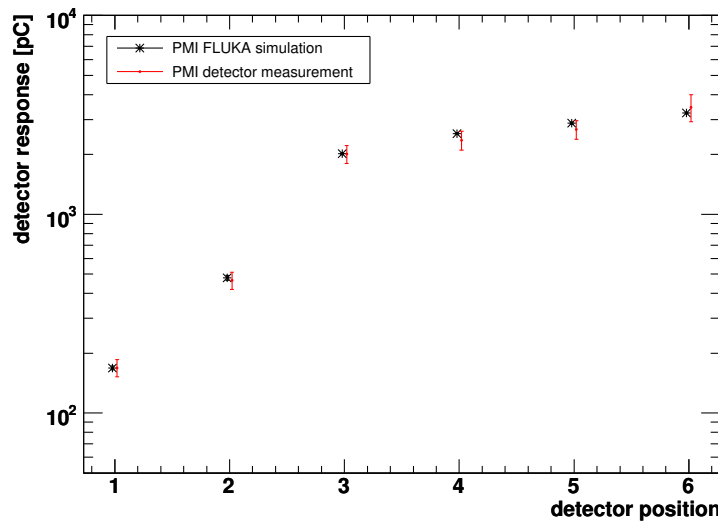


Figure 5.32: Comparison of FLUKA simulations and measurements for the PMI detector. Detector response normalised to an active volume of 1 dm^3 [43].

shown. The relative difference between the simulation and the experimental data is up to 12%, except at detector position 1. There, a relative difference of 21%, in the final simulation, is observed.

At detector position 1, mainly back-scattered particles arrive. Most are low energy neutrons and gammas. The FLUKA spectra has large statistical fluctuations and discontinuities above 300 MeV as shown in Figure 5.28. The lower energy cut-off of the SPS detector leads to less particles that can contribute to the signal and the SPS detector response functions show from 10 MeV onwards an increases in response which lead to a too low simulated detector signal. The uncertainties in the spectra were not compensated which could be partly performed by fitting the spectra or increase the number of primary particles in the spectra simulation.

As mentioned, the particle's starting position and direction are neglected. Instead a uniform distribution with random starting positions of the particles is applied. To increase the possibility of a particle interaction which contributes to the signal and to reduce the uncertainties on the detector signal due to simplifications in the simulation, the spectra are initialised 1000 times at detector position 1 compared to 10 times at the other positions. A significantly better agreement between simulation and measurement is observed. The relative difference between the simulation and the measurement decreased by 6.5%. The error on the Geant4 results is calculated as standard deviation of the mean. Due to launching the particle fluence spectra more often the error on the results is artificially decreased. To correct for this procedure the errors are multiplied by the square root of the number of repetitions.

At the other detector positions the simulation results lie within the uncertainties. The best agreement is found at detector 3. The simulated detector signal is 5% higher than the measured one. At detector positions 4 and 5 the simulation result is 12% larger. The last detector, number 6 is closest to the original beam. Misalignment errors have a large effect on the results. Even at this position the simulation agrees with the measurement within 8%.

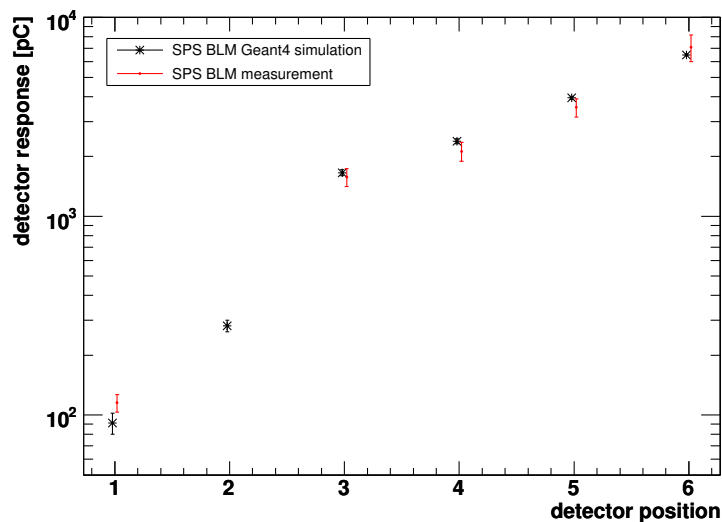


Figure 5.33: Comparison of Geant4 simulations and measurements of the SPS beam loss detector. Detector response normalised to an active volume of 1 dm³.

Table 5.16: Comparison of SPS beam loss monitor measurements and the corresponding Geant4 simulations.

position	Geant4 simulation [pC]		measurement [pC]		ratio	
	SPS BLM	error	SPS BLM	error	sim/meas.	error
1	91.13	11.09	115.33	11.66	0.79	0.13
2	281.22	18.9	—	—	—	—
3	1656.38	57.57	1577.75	162.59	1.05	0.11
4	2386.62	68.09	2121.52	230.69	1.12	0.13
5	3943.99	73.12	3531.98	370.42	1.12	0.12
6	6495.5	55.46	7091.16	1096.82	0.92	0.14

Conclusion

To obtain a better understanding for the LHC beam loss monitor, measurements with similar SPS beam loss monitors were performed at the CERF target area (H6) and compared to Geant4 simulations. Geant4 is utilised to perform the detector response simulations for the LHC BLM detectors.

The lack of available LHC BLMs made it necessary to utilise SPS BLMs. But these two types of detectors utilise the same principles of particle detection (ionisation chamber) and are similar in their design. One major difference is the detector volume, which should not compromise the results.

One of the previous experiments performed at the CERF target area was taken as a guide for the experiment described in this report. One can find a description of the former experiment in [43].

Measurements within one order of magnitude in beam intensity showed a proportional detector response in respect to the given PIC counter uncertainties.

The Geant4 simulations compared to the measurements show an acceptable consistency. The difference is within 12% for all detector positions except position 1. Here, the measured signal differs from the simulated one by 21%. The detector specific energy cut-off, the shift of the particle fluence spectra to lower energies (below 300 MeV) and the large statistical fluctuations and discontinuities above 300 MeV lead to a low statistics in the number of particles that contribute to the detector signal (Figure 5.28).

It was shown that the Geant4 simulations reproduce well the measurements. One concludes that the simulations work well for the different particle types. The results indicate that the detector response can be simulated with Geant4 to better than 20% accuracy (worst case), starting from given energy-particle-spectra.

5.5 Summary

The ionisation chamber, which is the main detector type of the LHC BLM system was simulated in Geant4. The statistical and systematic uncertainties in the simulations were investigated by geometry, range cut-off value, impact angle variations and utilising different physics lists. Utilising the results from these uncertainty investigations the detector response functions were simulated with the QGSP-BERT-HP physics list of Geant4, for different particle types at various kinetic energies in the range of 10 keV to 1 TeV and for transverse and longitudinal impact of the particles. The validation of these detector response functions and the calibration of the detector was performed in four irradiation scenarios with different particle types and at various kinetic energies.

The results from the three direct irradiation experiments, the proton experiment, the gamma-ray experiment and the neutron experiment are all within approximately 15% of the simulation results. The mixed radiation field measurements and simulations for the first detector agree within 21%, for the other detectors the agreement was better than 12% with an error of 11%.

A comparison of particle fluence spectra obtained outside of an LHC quadrupole magnet (see chapter 7) and the particle fluence spectra derived from the simulations of the mixed radiation field experiment at detector position 2, 3 and 4 shows that these spectra are similar. From these characteristic spectra to which the LHC BLM detectors are exposed the one at position 4 shows the largest total uncertainty of 17% in the comparison of measured to simulated detector signal, which is derived for the 12% deviation with its error of 11%. Therefore, the uncertainty of 17% is utilised as the systematic error of the detector response functions.

Chapter 6

Error Estimation on Hadronic Shower Tail Simulations and Measurements

6.1 Introduction

The LHC beam loss monitors (BLM) are placed outside of the magnet cryostats. The initial threshold levels for quenching and for damaging the magnets are mainly derived from simulations. Far away from the shower axis large simulation uncertainties are expected for transverse hadronic shower tails. Monte Carlo simulation codes like Geant4 or FLUKA describe calorimeters very well. There, it is important to predict the energy deposition in the core of the shower. In the case of quench level prediction the energy deposition in an ionisation chamber to the tails of hadronic particle showers is important. The specification of the system requires a total final uncertainty of a factor of 2. To investigate the uncertainties in such a special application, hadronic shower simulations are compared to measurements. In 2005 no accelerator was running at CERN. Therefore, the measurements were performed at DESY's electron proton collider HERA.

Considered were different options to measure hadronic shower tails. An alternative was to utilise a superconducting quadrupole or dipole magnet at HERA. But the necessary beam intensity measurements including particle tracking, in which the uncertainties were difficult to predict in advance, would have presented a major effort. Therefore, the HERA proton beam dump fitted best the requirements to measure far tails of transverse hadronic showers. Eight ionisation chambers were installed around the beam dump. Six of them were placed on top of the dump. The particles have to traverse a large amount of material before they reach the outside of the dump and hit the detectors. In the years 2005 to 2007 the installation was nearly continuously running and acquiring data, which was a long term test of the LHC BLM system in real accelerator environment.

6.2 The HERA Proton Beam Dump

The largest accelerator at DESY is HERA. It is a superconducting proton on electron/positron collider. HERA was designed to store up to $2 \cdot 10^{13}$ protons at an energy of 820 GeV. This corresponds to a total beam energy of 2.6 MJ. An upgrade in 1996 extended the top energy to 920 GeV. If the beam is lost in an uncontrolled way in the ring, the components could suffer great damage. 2.6 MJ are enough to melt 3.6 kg of iron. Additionally, there is the risk of quenching a superconducting magnet, which requires about 1 mJ in one gram of the superconducting coil. An additional risk is connected to the particle type. Electrons interact with the atomic shell, but hadrons (e.g. protons) interact with the nucleus of the atoms. An impact of highly energetic protons on matter activates it, producing radioactive elements [44][45].

These reasons make it clear that it is necessary to have a proton beam dump at which it is possible to absorb the beam in a controlled manner without damaging or destroying machine components. The production of radioactive nuclei can not be avoided, but with a beam dump they are located in one place and not distributed around the whole ring.

Three other elements, which also belong to the beam dump, are the kicker-magnets, the pulser and the control electronics. As the system is also important for human safety, the pulser and the electronics have simultaneously working backup systems.

Besides the trigger pulses, two more signals are required. Depending on the beam energy, the amplitude of the kicker pulse current has to be changed. At the ramping of the beam momentum the pulse height is increased at the same time. Second, the kicker pulse has to be synchronised to the specially created hole in the otherwise regular proton bunch pattern, because the normal bunch spacing of 96 ns is insufficient to rise the kicker magnets to the necessary field strength to divert the beam onto the dump. Otherwise, the beam is lost elsewhere in the ring.

The internal dump is located in the HERA proton storage ring at about west left (WL) 80 m. WL represents one eighth of the ring, where no experiment is situated and the vacuum system of the proton and the electron ring are separated. The first superconducting magnet is 80 m downstream, which minimises the risk of quenching it by secondary particles leaving the dump.

Table 6.1: Comparison of a superconducting LHC magnet to the HERA proton beam dump in terms of radiation length (X_0) and nuclear interaction length (λ_0) [46].

distance		HERA dump		distance		MQY LHC	
long. [m]	lateral [m]	$[X_0]$	$[\lambda_0]$	lateral [m]	$[X_0]$	$[\lambda_0]$	
0	0.5	21.02	2.28	0.33	11.59	1.17	
1.5	0.5	64.44	6.98	0.33	51.08	5.17	
2.5	0.5	103.42	11.18	0.33	83.83	8.49	
3.5	0.5	144.57	15.62	0.33	116.86	11.83	
5	0.5	202.54	21.88	0.33	—	—	
6	0.5	246.47	26.64	0.33	—	—	

The proton beam dump of HERA has a rather simple geometry compared to a complex superconducting magnet, but in terms of material to be traversed by the beam particles it is similar. In table 6.1 the radiation lengths X_0 and nuclear interaction lengths λ_0 for different detector locations (like HERA dump installation) are compared between HERA dump and MQY LHC

quadrupole. The dump is in terms of radiation length and nuclear interaction length less than a factor of two “thicker” at detector position one and about 30% “thicker” at the other detector positions. Monte Carlo shower simulations predict well the particle distribution in the centre of the shower [24]. The prediction in the far tails of showers is in most applications, e.g calorimeters, of less interest and less well described. In terms of radiation length and position of the detectors in the hadronic shower tails the HERA proton beam dump simulation provides an upper limit compared to the simulations, which have to be performed for the threshold determination of the LHC BLM system.

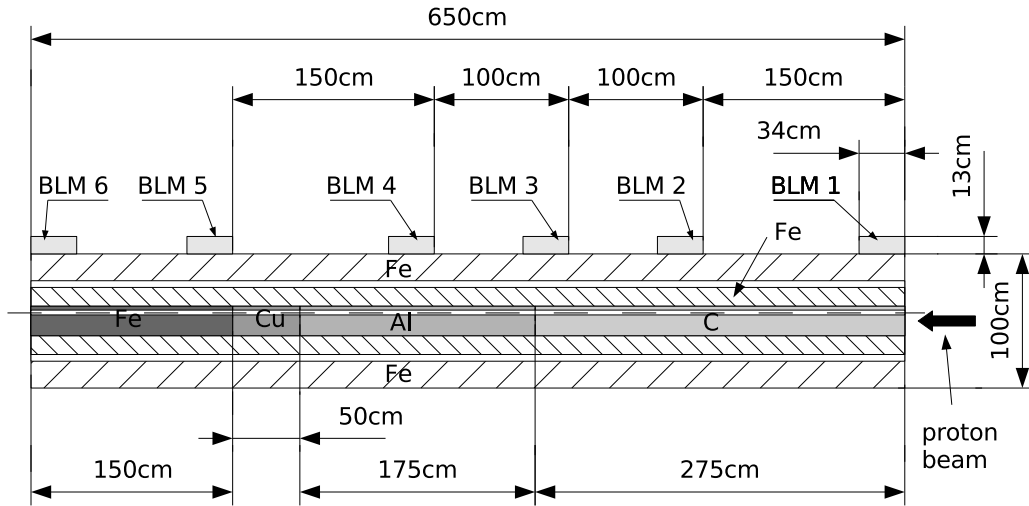


Figure 6.1: Schematic of the HERA proton beam dump (side view). Protons are arriving from the right onto the carbon piece. The installed SPS BLM detectors are illustrated on top as boxes [44].

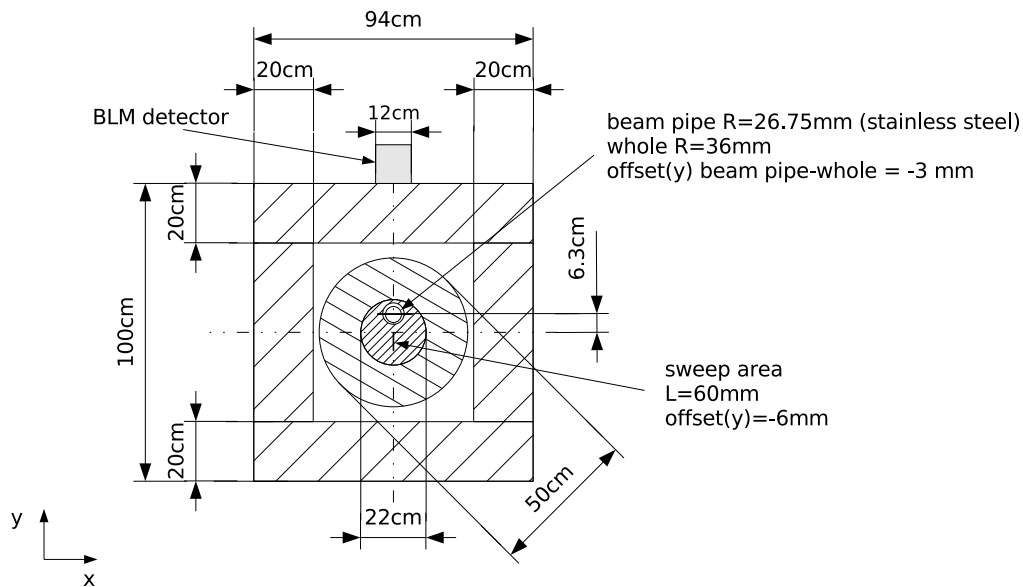


Figure 6.2: Schematic of the HERA proton beam dump. View in beam direction [44].

A cut through the configuration of the HERA proton beam dump is illustrated in Figure 6.1 and Figure 6.2 [44]. The beam pipe is passing the dump close to its centre. The deflection needed to divert the beam towards the position specified for its absorption is therefore small. A complete fill of the storage ring (up to $2 \cdot 10^{12}$ protons) is distributed across a vertical line between 6 cm and 12 cm from the beam orbit. With this sweeping procedure the total energy

in the beam is distributed over a larger area, which decreases the local energy density. The energy density is additionally reduced by the longitudinal segmentation of the dump in materials with increasing atomic number and density. This inner or “hot” core consists of cylindrical filling pieces with a diameter of 22 cm and are made subsequently of carbon (length: 2.75 m), aluminium (length: 1.75 m) and copper (length: 0.5 m). A final piece made of iron (length: 1.5 m) provides the shielding in the longitudinal direction. All filling pieces have a non concentric hole with a diameter of 72 mm, through which the beam pipe with a diameter of 53.5 mm is passing. This inner core is surrounded by a 14 cm thick iron cylinder. For the final shielding in the transverse direction four quadratic iron blocks with a thickness of 20 cm and a length of 6.5 m are utilised, which is the total length of the beam dump. The dump has a total mass of about 40 t.

After the beam is deflected by the kicker magnets about 60 m upstream of the dump, it still travels in vacuum until 30 cm before the dump. Here it traverses a 3.5 mm thick wall of stainless steel and passes through air before it hits the front face of the carbon piece and starts showering.

Previous simulations [44] of the hadronic and electromagnetic showers have shown that the inner core (C, Al and Cu filling pieces) absorbs 62% and that the whole dump absorbs 98% of the beam energy.

Additional calculation of the heat load and the remanent radiation were performed [44]. The temperature increase by impacting protons is in both cases, with and without sweeping, below the melting temperature of the corresponding materials. From the point of view of mechanical destruction, a beam extraction without sweeping might damage the carbon and the aluminium piece. The remanent radiation outside of the dump was estimated in the worst case to be about 2.6 mGy/h after 10 years of operation and a decay time of 15 min.

From the measurements performed for this work the remanent radiation after an extraction was estimated. After 10 seconds the dose rate of 0.63 Gy/h was measured. After 15 minutes 2.7 mGy/h and after 20 min 2.04 mGy/h were found. This agrees well with the results described in [44].

6.3 HERA Proton Beam Dump Measurements

In total 15 SPS BLM type ionisation chambers were installed at HERA. Seven of them were installed at special locations, e.g. at the collimators, to compare the signal to the one measured by the beam loss measurement system of HERA itself and for system tests. The rest of the detectors were placed around the HERA proton beam dump. Six ionisation chambers were mounted on top of the dump as shown in Figure 6.1 and Figure 6.3. The detectors were placed in the middle of the dump, parallel to the beam direction and roughly spaced by 1 m in longitudinal direction. The exact position are plotted in Table 6.2. The distances are measured downstream in beam direction from the impinging point of the protons.

Table 6.2: Detector positions. The distance is measured from the beam impacting point in longitudinal direction (beam direction) to the first edge of the detectors.

position	det 1	det 2	det 3	det 4	det 5	det 6
distance [cm]	0	150	250	350	500	615

No shielding from synchrotron radiation was installed around the ionisation chambers on the



Figure 6.3: Detector installation on the HERA proton beam dump.

dump. The standard beam loss detectors of HERA are shielded by a few centimetre of lead. This prevents photons, mainly produced by the electron beam from triggering a signal. The beam dump is located in a straight section where very little synchrotron radiation is expected anyway. Observations of the accelerator operation showed that the standard procedure of dumping the two beams, is to extract the electrons first and afterwards the protons. As the synchrotron radiation comes basically only from the electrons, shielding was not necessary. An exception is the seven detectors at the special locations, which were shielded by a few centimetre of lead, because these detectors were utilised during the operation of the accelerator.

6.3.1 Beam Parameter and Impact Position

After the latest upgrade of HERA in 1996, the protons can be ramped up to 920 GeV [45]. Protons are injected in three trains from the pre-accelerator PETRA at an energy of 39 GeV.

Ten bunches form a standard bucket, which can be placed anywhere in the ring. Only the first bunch position has to be filled. It is used to trigger the timing. The filling pattern for limited intensity runs is 3×50 bunches. If HERA is running at full intensity (standard operation) 3×60 bunches from PETRA are injected. An average single bunch intensity for the HERA proton beam is about $7 \cdot 10^{10}$ particles, that is for 180 bunches up to $1.3 \cdot 10^{13}$ beam particles. This corresponds to a beam current of 100 mA. The lowest beam current, for a single bunch, is about 0.5 mA [47].

The orbit of the proton beam in the region of the dump is lowered while the beam energy is ramped. The shift of the beam is performed with a closed orbit bump. This procedure keeps the beam as close as possible to the dump and decreases the necessary beam displacement to hit the dump at the foreseen position. In the following equations y_{max} is the largest distance the beam is deflected from its actual orbit.

The calculation of the impact position for a single bunch can be performed with equation 6.1 and equation 6.2. To keep the sweep area at the same position due to the above described shift of the orbit of 12 mm y_{max} is adjusted with respect to the beam energy. For $E = 39 \text{ GeV}$ $y_{max}(E)$

is 120 mm and for $E = 920$ GeV $y_{max}(E)$ is 108 mm. Equation 6.1 calculates for each bunch the impact position $y_n(E)$ relative to the closed orbit. The equation is valid up to bunch number 28 where the diversion reaches the maximum. For higher bunch numbers equation 6.2 calculates the correct impact position due to the exponential decay of the kicker magnet current with the decay parameter $\tau = 30.30 \mu s$. The mean impact position for a filling pattern of 150 bunch positions, shown in Figure 6.4 left, is at about 82.3 mm. The distance refers to the centre of the nominal beam orbit. Both formulae were applied and the resulting impacting positions for each bunch are shown in the left plot of Figure 6.4 (at 920 GeV). Empty bunch places have zero as bin content. The transverse beam size at the dump is at low energy about 10 mm (2σ) and at high energy about 2 mm (2σ).

$$y_n(E) = y_{max}(E) \cdot \sin(2\pi/16 \{1.359 + n \cdot 0.096\}) \quad (6.1)$$

$$y_n(E) = y_{28}(E) \cdot e^{-\left(\frac{(n-28) \cdot 0.096}{\tau}\right)} \quad (6.2)$$

In the HERA database one can find single bunch current measurements. An analysis of this data was performed to estimate the error on the final results derived from different bunch filling patterns, because the mean impact position of the protons and therefore the detector signal varies with the filling pattern. The number of acquired dump events was limited, but for dumps with 150 proton bunches in the accelerator a systematic variation of about 5% to 10% on the detector signal due to different filling patterns was found.

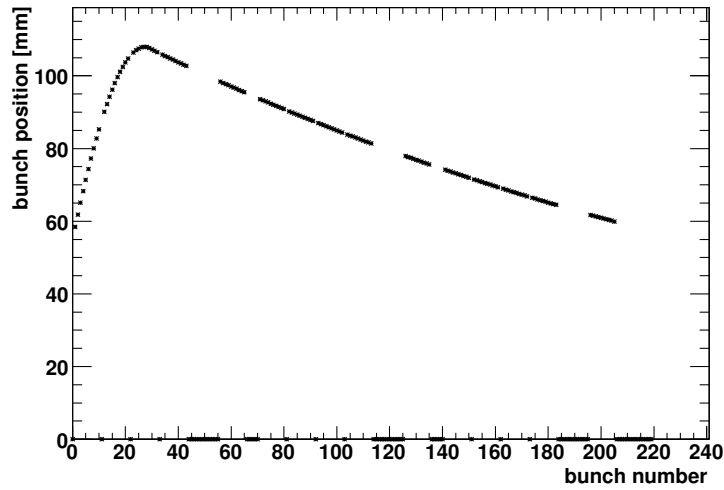


Figure 6.4: Calculated bunch impact position for 920 GeV relative to the beam orbit.

6.3.2 Data Acquisition System

In addition to the detectors a complete LHC BLM acquisition electronics was installed. Each detector is connected with a coaxial cable to a patch box. The detector installed around the beam dump are connected to a C-R filter, because the detector signal exceeded the measurement range of the acquisition electronics, which has an upper limit of 1 mA. The filter consists of a $1\ \mu\text{F}$ capacitor and a resistor of $10\ \text{k}\Omega$ which is placed in the patch box in the tunnel close to the dump and an additional resistor of $21.5\ \text{k}\Omega$ which is connected in the surface patch box. The two patch boxes (tunnel and surface) are connected via a NG18 cable. From there the signal is fed into one of the two CFC (current frequency converter) cards. These cards integrate the current over a period of $40\ \mu\text{s}$ and convert it to a frequency which is transmitted through a fibre connection to the DAB (data acquisition board). The DAB calculates different running sums (integration over different time periods) and logs the maximum of each running sum every second. The latest installed acquisition software provided the record of $40\ \mu\text{s}$ data for a period of 1.7 s which is self-triggered by the counting rate of the detector signal (threshold of eight ADC counts). This feature was introduced at the end of 2006. The final readout of the DAB is performed with a Power-PC that records the data continuously on a Linux machine. A layout of the acquisition system is shown in Figure 6.5.

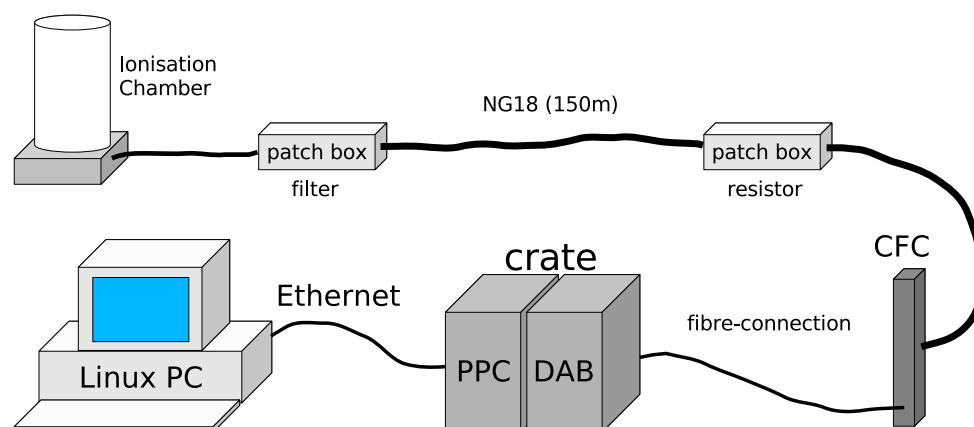


Figure 6.5: Installed acquisition chain (similar to the one in LHC) for the eight detectors on the beam dump.

6.3.3 Calibration of the Electronics

In February 2007 the acquisition electronics utilised at the HERA beam dump experiment was sent back from DESY and calibrated. An equivalent network of the experimental setup at DESY was built in the laboratory. The ionisation chamber was replaced by a $1\ \mu\text{F}$ capacitor, which is alternately charged and discharged. The capacitor serves also as part of the filter. A switch toggles between a voltage source and the input to the equivalent network. It is triggered every 20 seconds by a frequency generator. In Figure 6.6 a schematic of the equivalent network is shown.

All filters in the experiment were implemented as well as the 150 m long cable. An analysis of the $40\ \mu\text{s}$ acquisition data (“post-mortem” data) showed for the installed acquisition chain at HERA a signal decay time of 40 ms, therefore an additional resistor with $5.1\ \text{k}\Omega$ was added to reach a similar signal decay time in the calibration circuit. With respect to different beam intensities a scan in charging voltage was performed. The scan was conducted from 10 V down to 2 mV ($10\ \mu\text{C}$ to 2 nC) which results in roughly 55000 CFC counts to eight CFC counts in the 1311 ms running

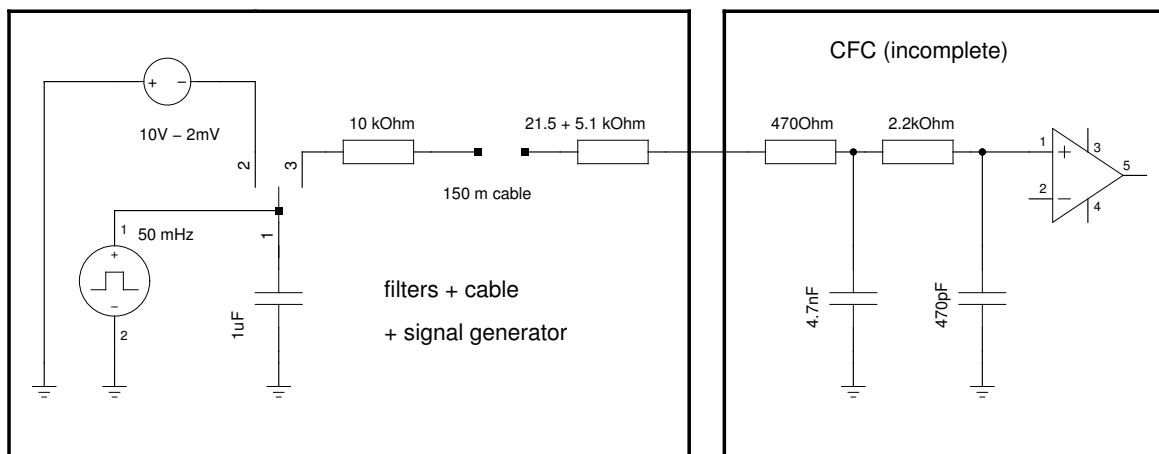


Figure 6.6: Diagram of the electronic circuits used to calibrate the LHC BLM electronics.

sum. The supply voltage to the switch was limited at 15 V. To reach higher counting rates we utilised two serial capacitors with a total capacity of $1.307 \mu\text{F}$ and charged them manually. With this method it was possible to drive the charge frequency converter (CFC) into saturation at about 200 V. That corresponds to a maximum counting rate of 255 in the $40 \mu\text{s}$ running sum.

The results for the low and high CFC counting ranges are combined and shown in Figure 6.7. In the plot two calibration data sets with different filter settings are compared to a linear fit of the data in the upper CFC counting range. The kink in the data is shifted to lower CFC counts, between 800 and 900 CFC counts, for the larger signal decay time $\tau = 40 \text{ ms}$. This calibration set-up represents reasonably well the HERA set-up which has a kink in the acquisition data at about 850 CFC counts. The calibration set-up is however not perfect, as there is still some remaining non-linearity at low counting rates. Below 300 CFC counts the deviation from the linear fit of the data is most probably due to the non-zero inner resistance of the utilised switch. The kink in the data sets is due to the data acquisition board's (DAB) internal combination of the raw counting numbers with the ADC values which will disappear in the latest version of the hard and software. The final conversion of the measured CFC counts into acquired charges was performed by a linear interpolation of the calibration data ($\tau = 40 \text{ ms}$). In addition a cut on the results below $0.15 \mu\text{C}$ was introduced which corresponds to roughly 900 CFC counts to partially avoid the kink in the analysis.

An error on the calibration was estimated from the largest deviation of the latest calibration data from a linear fit, which is the difference between the maximum and the minimum of the residuals. This difference amounts to 40% (four sigma) from which a systematic error of 10% is derived.

6.3.4 Data Acquisition and Data Analysis

The data acquisition is parasitic while HERA is performing its normal operation. If the beam intensity of the protons and/or the electrons gets too low for the experiments the beams are dumped and the accelerators are refilled. There was no direct connection between the HERA controls and our acquisitions electronics. Therefore, the acquisition was performed around the clock. Only the latest versions of the acquisition software were self-triggered, to record the “post mortem” data.

The database of HERA holds information about the time, the energy and the beam current for

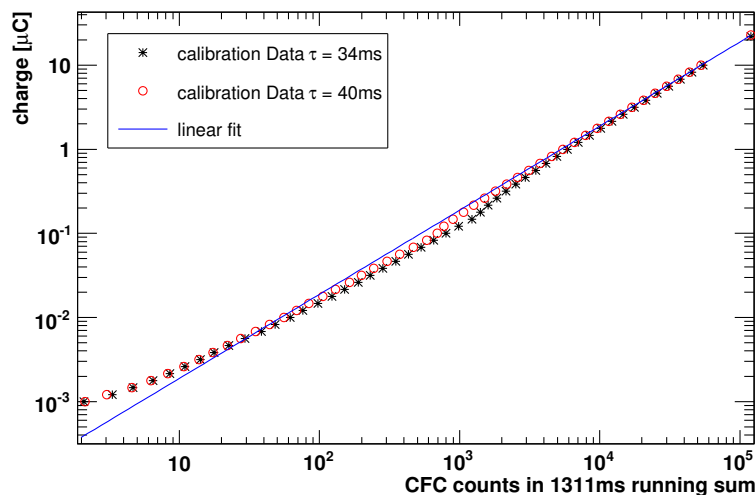


Figure 6.7: Results of the electronics calibration. The measured counts in the 1311 ms running sum can be converted into μC .

each beam dump event. Also available is the information if the beam dump was triggered by the operator or due to a beam dump signal from any of the instruments. In the data analysis the two information from the HERA database and the performed acquisition data are combined. Each beam dump in the HERA database file, triggered by an operator, was taken into account. These beam dumps are referred to as “clean dumps” and it is assumed that all protons in the beam are extracted onto the dump and nowhere else in the ring. For each detector the corresponding maximum for each running sum is searched in the combined data sets.

As previously described, the signal has a decay time τ of about 40 ms due to the installed filter. After $5 \times \tau$ it is assumed that all of the charges are integrated. Therefore, the running sum of 1311 ms was chosen for the analysis. The maximum of this running sum contains the total integrated charge produced during the beam dump in the detector. In the ongoing analysis the derived maxima, in CFC counts, have to be converted into acquired charges. For a first conversion the electronics specification were taken which is 200 pC per CFC count. This resulted in an unusual behaviour of the detector response at low counting rates. Each detector showed in its response a kink at the same signal level at about 850 CFC counts. As a next step the electronics was calibrated. A description of the calibration procedure can be found in the previous section 6.3.3.

The final calibrated ionisation chamber signals in μC versus beam intensity in mA for all detectors on the dump are plotted later in this chapter in the left two plots in Figure 6.11. The upper plot shows the results for 39 GeV and the lower one for 920 GeV.

Usually, one expects from an ionisation chamber operating in the plateau of the saturation current a linear relation between ionisation rate and detector signal. The results show that the detector signal is outside of this linear regime. To understand this behaviour different sources of non-linearity were investigated, such as systematic effects due to the beam sweep on the dump (see section 6.3.1), recombination losses (see section 6.3.5) and space charge effect corrections (see section 6.3.6).

In Figure 6.8 measurements taken at different beam intensities for both energies are shown. The detector signal is normalised to the beam intensity and plotted for each detector position

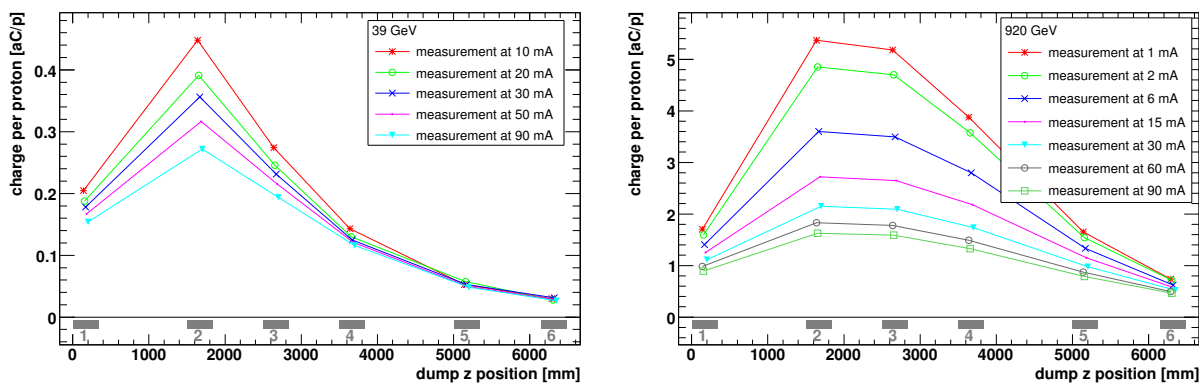


Figure 6.8: Normalised detector signal at different beam intensities versus detector position on the dump. The beam is impinging from the left side. Left: for 39 GeV. Right: for 920 GeV.

(distances are given relative to the impact point of the protons). In the left plot measurements taken between 10 mA and 90 mA of beam current at 39 GeV are compared. The difference in relative response is in the peak about 40%. For all detectors the relative signal increases at lower beam currents. For the detectors that are outside of the shower maximum the difference in relative signal is smaller. At the furthest detectors, 5 and 6, the response is nearly constant. At 920 GeV the same procedure is performed. Measurements between 1 mA and 90 mA are compared and shown in the left plot of Figure 6.8. The maximum difference for the relative response is about 70% at detector 2 and 3. Again, at detectors 5 and 6 the relative response varies less than the one at the other detectors. A comparison of the shower position, between 39 GeV and 920 GeV, shows that the shower maximum is shifted to a larger z-position and is broader at 920 GeV.

Recombination losses were not included in the Monte Carlo simulations. To compare the measurements to the simulations correction have to be applied which are described in the following sections.

6.3.5 First-order Recombination Loss Correction

An ionisation chamber shows up to a certain ionisation rate a linear response in intensity. But with rising ionisation rate recombination losses start to influence the measurement. At higher rates some of the charge ionised will not be collected on the electrodes due to recombination of ions and electrons. In a gas with a certain electron density n_- and an ion density n_+ the removal of charged particles by recombination is given by:

$$\frac{dn_-}{dt} = \frac{dn_+}{dt} = -r \cdot n_- n_+ \quad (6.3)$$

where r is the recombination coefficient [48].

Following the discussion in [49], the charge flow in an ionisation chamber can be described by coupled differential equations. A first order recombination loss simplification of this differential equations can be performed. A description of the equation system and the simplification can be found in the thesis of Zwaska [49].

In the work of Zwaska an equation to describe the recombination losses is derived. The collection efficiency ε is defined as the ratio between the charge collected Q_m at the electrodes and the initially created charge Q by the beam

$$Q_m = \varepsilon \cdot Q \quad (6.4)$$

where ε is given by:

$$\varepsilon = 1 - \frac{r_e \phi d^2}{6\mu E v_{e^-}(E)} \quad (6.5)$$

Here $r_e=2 \cdot 10^{-6}$ [cm³/(ions·s)] is the recombination coefficient, ϕ refers to the charge number density and is given in [1/cm³μs]. The distance between the electrodes is $d=0.58$ cm, the ion mobility expressed by μ equals $2.13 \cdot 10^{-6}$ [cm²/Vμs] and the electric field strength $E = U/d = 1724$ [V/cm] ($U = 1000$ V). The electron drift velocity at 1000 V in Nitrogen is $v_{e^-}=2$ [cm/μs].

After solving equation 6.5 for the created charge Q , a formula which can be directly applied to the measurements is derived:

$$Q = \frac{1 - \sqrt{1 - 4KQ_m}}{2K} \quad K = \frac{r_e d^2}{6\mu E v_{e^-}} \cdot \frac{1}{qV_{SPS}t_c} \quad (6.6)$$

Here q is the elementary charge, $V_{SPS} = 1200$ cm³ is the active detector volume and t_c refers to the irradiation time of 20 μs.

In Figure 6.9 the results of the equation 6.6 in a range of $Q_m = 2 \mu\text{C}$ to $30 \mu\text{C}$ are compared to a linear response. The recombination losses at $2 \mu\text{C}$ are about 1% and at $30 \mu\text{C}$ roughly 14%.

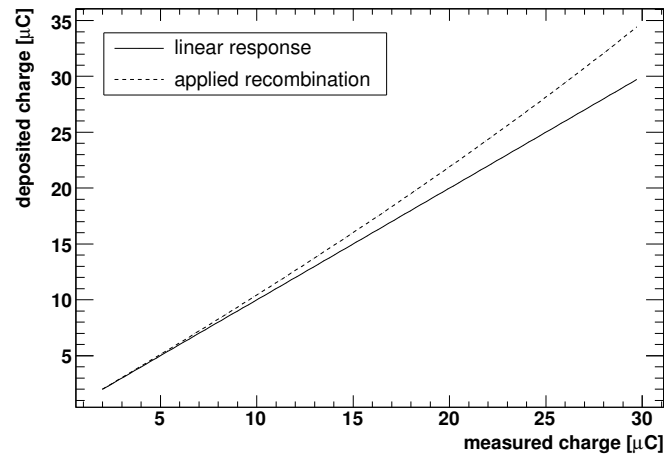


Figure 6.9: Comparison between a linear response to the one calculated from first-order recombination.

The measurement was corrected with the derived equation. A comparison of the corrected data to a linear response was not satisfactory. A calculation of the validity range of the above used simplification showed, that the measurements at highest beam current are above an ionisation rate at which space charge effects start to play an important role.

6.3.6 Space Charge Effect Correction

The maximum measured charge on the HERA beam dump is about $25 \mu\text{C}$. In a sensitive detector volume of 1200 cm^3 and with an irradiation time of $20 \mu\text{s}$ this corresponds to an ionisation rate of $6.5 \cdot 10^9 \text{ ions}/(\text{cm}^3 \mu\text{s})$. Space charge effects start to be important for the utilised ionisation chamber configuration at an ionisation rate of about

$$\phi_{crit} = \mu \frac{\epsilon_0}{q} \cdot \frac{4U^2}{d^4} = 4.16 \cdot 10^7 \left[\frac{\text{ions}}{\text{cm}^3 \mu\text{s}} \right] \quad (6.7)$$

which corresponds to a charge of $0.16 \mu\text{C}$ in the detector and is about 100 times lower compared to the measured ionisation rate.

In the thesis of Zwaska [49] space charge calculations are treated which are discussed below.

Space charge refers to slow moving ions that deform the applied electric field. At the critical ionisation rate, a dead zone starts to form. The electric field is completely shielded by the ions (nearly field free zone). As long as the irradiation continues the charge density in the dead zone increases approximately linear in time. If the ionisation rate is higher than the critical one, the dead zone expands. If one assumes all charges generated in the dead zone to be lost due to recombination, the effective length of the ionisation chamber is reduced by the width of the dead zone. A formula to calculate the effective length x_0 of the ionisation chamber is derived in the thesis of Zwaska

$$x_0 = \left[\frac{\epsilon_0 4\mu U^2}{q \phi} \right]^{1/4} \quad (6.8)$$

where ϕ is the ionisation rate. The space charge collection efficiency coefficient ϵ_{sc} can be expressed as

$$\epsilon_{sc} = x_0/d \quad Q_m = \epsilon_{sc} \cdot Q \quad (6.9)$$

One can derive from the equation above the analytical correlation between measured and deposited charge

$$Q = \left(\frac{Q_m}{K_2} \right)^{\frac{4}{3}} \quad K_2 = \frac{1}{d} \left[4 \cdot \epsilon_0 \cdot V_{SPS} \cdot t_c \cdot \mu \cdot U^2 \right]^{\frac{1}{4}} \quad (6.10)$$

The operating range of the beam loss monitors at the HERA proton beam dump is overlapping with the region where space charge effects start to develop (above $0.16 \mu\text{C}$). In Figure 6.10 the ranges for the nominal LHC beam loss monitoring operating range and the HERA dump measurement range are compared to the calculated range for the space charge effect. For most of the data taken at DESY a space charge correction is necessary. The ionisation rates at the standard BLM detector locations (magnets) in the LHC are below this threshold; therefore, no correction due to space charge effect has to be applied.

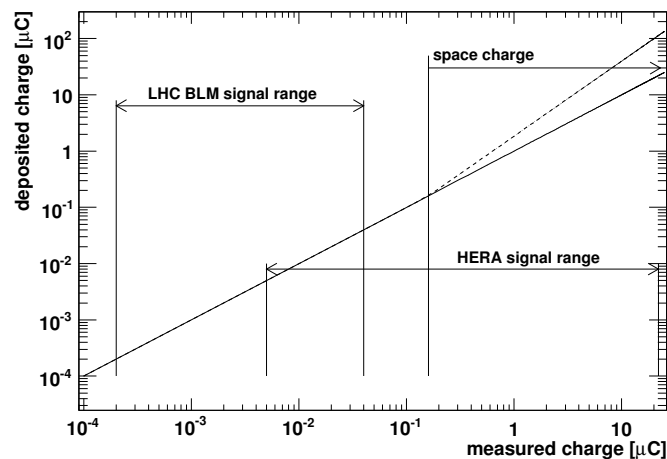


Figure 6.10: Comparison of the measurement range of the LHC BLM system and the HERA dump experiment. Space charge effect is only important for the HERA dump experiment.

Table 6.3: Signal charge dependant correction factors due to space charge effect for each detector with respect to the beam intensity.

detector	39 GeV		920 GeV	
	$I_{min}=1$ mA	$I_{max}=90$ mA	$I_{min}=1$ mA	$I_{max}=100$ mA
1	1	2.25	1.09	4.2
2	1	2.72	1.59	5.12
3	1	2.43	1.57	5.08
4	1	2.05	1.43	4.78
5	1	1.53	1.08	4.03
6	1	1.26	1	3.38

6.3.7 Measurement Results

Only formula 6.10 is applied to the data which does not include the previously described recombination effects. A major improvement in the linearity of the signal is observed. In Figure 6.11 the two left plots show the original measurements at 39 GeV (upper plot) and 920 GeV (lower plot). In the right plots the corresponding space charge effect corrected measurements are presented.

The relative residuals of the linear fits are shown in Figure 6.12 for both energies. The relative residuals are calculated as the difference between the linear fit forced through zero and the space charge effect corrected data divided by the linear fit. At 39 GeV the relative residuals are off by up to 25%. At 920 GeV below 40 mA, the deviation is up to about 50%. With the theoretically derived equation to calculate the space charge effect correction the detector response is roughly linearised. Still, the correction is not perfect as the relative residuals show.

Each of the detectors on the beam dump is exposed to a different radiation field in particle composition, energy and flux. Therefore, their signals differ. Each detector signal has to be multiplied by the corresponding space charge correction factor. In Table 6.3 the extreme cases of this correction factors are shown. At low energy, 39 GeV and low beam intensity the collected charge is not influenced by space charge. At beam intensities of 90 mA corrections between 1.26

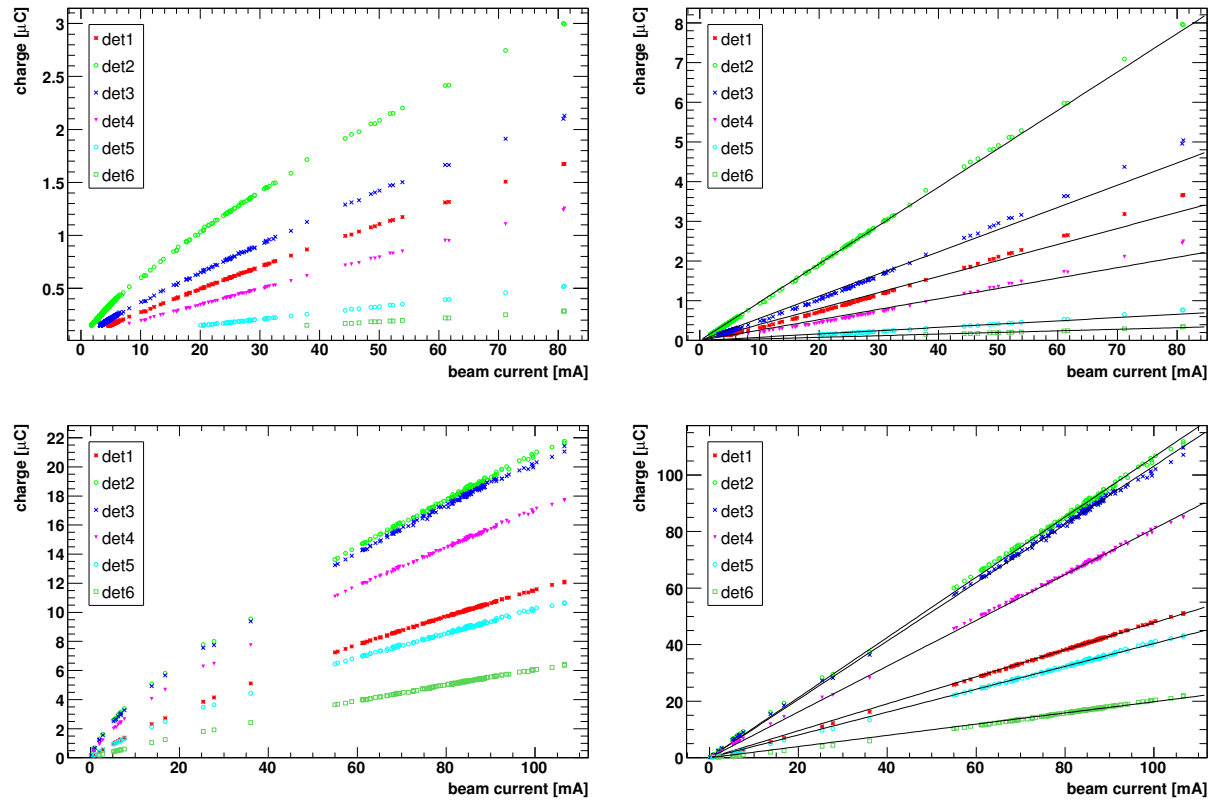


Figure 6.11: In the upper left plot the measured detector signals on the HERA beam dump at 39 GeV is shown. The upper right plot shows the space charge effect corrected measurements. In the lower left and right the measurements and the corrected ones for 920 GeV are shown.

and 2.72 have to be applied. The measurements taken at 920 GeV with a beam intensity of about 1 mA are already in the affected range. The corrections are between 1.0 and 1.59. At high beam currents, 100 mA, factors from 3.38 to 5.12 are predicted by the formula. The charge collection efficiency of the detectors at such high fluxes is reduced by more than 80%.

It was mentioned that the measurement results below $0.15 \mu\text{C}$ were discarded due to a non-linear behaviour of the acquisition electronic. The non-linearity is corrected for in the latest version of the LHC electronics. The measurements above $0.16 \mu\text{C}$ are space charge effect corrected and normalised to the number of protons impinging on the dump. Figure 6.13 shows the corrected relative detector response.

The final results, which are compared to the simulated signal, are derived by calculating the average between the normalised signal maximum and the normalised signal minimum in the range from $1.2 \cdot 10^{12}$ to the maximum beam intensity. This procedure is shown in Figure 6.13. The horizontal lines indicate the averages, which are expressed in atto-coulomb per proton. The error on the measurements is estimated again for the same beam intensity range as the difference between maximum and minimum of the relative signal, which is assumed to be 4 sigma. This method to calculate the mean and the error on the mean is utilised due to large differences in the number of acquisitions at different beam intensities. This error estimate comprises statistical errors (below 1.2%), uncertainties from the beam sweep procedure and uncertainties from the space charge effect correction.

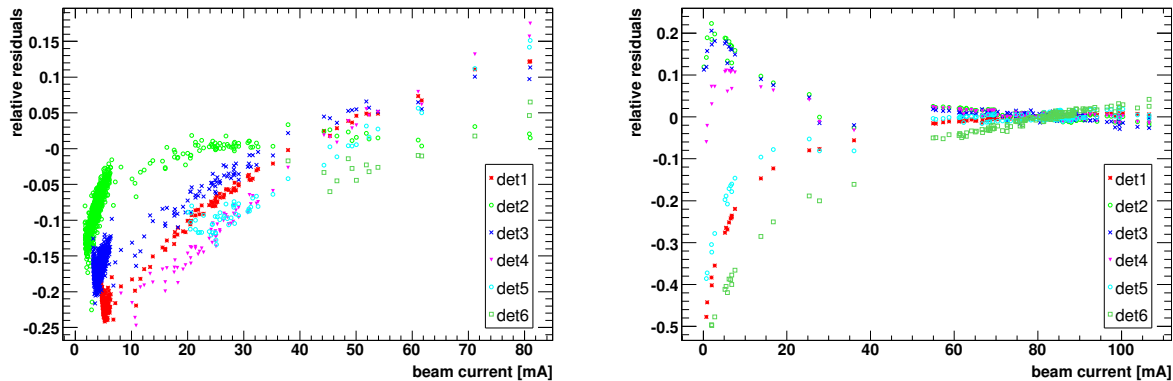


Figure 6.12: Relative residuals for the linearly fitted space charge effect corrected measurements. Left: for 39 GeV. Right: for 920 GeV.

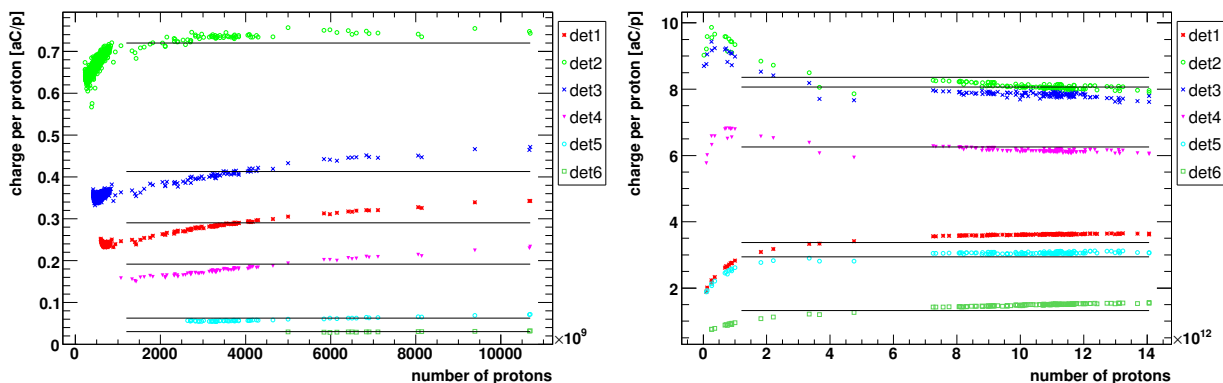


Figure 6.13: Relative detector signal versus beam intensity. The fitted lines are utilised to represent the average measurement results. Left: for 39 GeV. Right: for 920 GeV.

The measurements below a beam intensity of $1.2 \cdot 10^{12}$ protons show still a non-linearity and the signal characteristics is different for the different detectors. That shows that at low intensities additional effects are influencing the measurements. The origin of these effects could not be determined. Therefore, these measurements were not taken into account in the calculation of the results. These additional effects are currently subject of further investigations.

A summary of systematic errors in the measurements is shown in table 6.4. A systematic error due to remanent radiation, referred to as background, was estimated from the measurements to be below 0.1% as the signal of the detectors drops after a beam dump by a factor of 10^4 . The error on the proton beam intensity measurements at HERA was estimated to be below 2%. The error on the electronics calibration is about 10%. This error is derived from the largest difference of the relative residuals between the data and a linear fit. In the later described simulations the systematic error due to misalignment of the detector was investigated. Errors between 1% to 10% for the different detectors were found. The maximum total error from these uncertainties is about 12%. As mentioned, systematic errors due to different bunch filling pattern at similar beam intensities of 10% and from the space-charge-effect correction of 11% were found from their combined error of 15%.

The final results of the measurements are printed in table 6.5 for injection energy and high energy. The shown uncertainties are derived from the estimation in the measurement data as described

and by combining all found systematic errors which is at most 21%.

Table 6.4: Systematic errors estimated for the HERA dump measurements.

systematic error	
background	0.1%
beam intensity measurement	2%
electronics calibration	10%
misalignment of ± 1 cm	
detector 1	10%
detector 2	1%
detector 3	1%
detector 4	2%
detector 5	6%
detector 6	7%
totalised maximum systematic error	
beam sweep and bunch pattern	10%
space charge effect correction	11%

The conversion from beam current to beam intensity in number of protons in the accelerator is performed by:

$$N = \frac{I \cdot t}{q}$$

where N is the number of protons, I the beam current, t the revolution time which is at HERA $21.135 \mu\text{s}$ and q the elementary charge which has a value of $1.602 \cdot 10^{-19} \text{ C}$.

Table 6.5: Relative detector signal for each detector placed on the HERA proton beam dump at injection and high energy. Quoted are the ^{a)} combined uncertainty of beam sweep procedure and space charge effect correction and ^{b)} combined uncertainty for all found systematic errors.

detector	39 GeV [aC/p]	^{a)} error	^{b)} error	920 GeV [aC/p]	^{a)} error	^{b)} error
1	0.291	0.026	0.066	3.37	0.14	0.71
2	0.720	0.018	0.132	8.35	0.25	1.54
3	0.413	0.029	0.081	8.06	0.23	1.48
4	0.191	0.021	0.041	6.26	0.16	1.15
5	0.063	0.004	0.013	2.95	0.09	0.57
6	0.031	0.001	0.006	1.32	0.12	0.28

6.4 HERA Proton Beam Dump Simulations

Outside of a few nuclear interaction lengths the simulation of transverse hadronic shower tails has larger uncertainties than in the inner core of the shower. Therefore, the measurements are performed on the HERA proton dump and compared to simulations, which are described in this chapter.

There are several Monte Carlo codes available. At CERN Geant4 and FLUKA are used for many applications. For our investigations Geant4 releases Geant4.8.1.p01 and Geant4.8.2.p01 were chosen. FLUKA results [50] were kindly provided for comparison.

The HERA proton dump simulation was performed in Geant4 with several physics lists. Utilised were QGSP-BERT-HP and FTFP [51], for comparison LHEP-BIC-HP was used as well. For more information see chapter 4.

Three methods to derive the detector signals were utilised:

With the main method, which will be referred to as black-hole-method, all presented results are produced. The simulation is split into two parts. In a first step, the primary protons impinging on the dump are simulated up to the point where the secondary particles escape the dump and enter a defined volume. This volume is a long box, which encloses all six detectors. Particles entering this box are scored and artificially stopped. In this first part of the simulation different physics lists and Monte Carlo codes were utilised. In a second step, each detector is simulated separately with the QGSP-BERT-HP physics list of Geant4.8.1.p01. The recorded particles are utilised as input and the energy deposition in the detector is scored.

The second method is referred to as combined-simulation. It is equivalent to the black-hole-method and was utilised as a cross-check. All six detectors are included in the HERA proton dump simulation. Hence, the energy deposition (signal) in the detectors is recorded in one simulation run.

The third method, Folding-Method, is introduced to simplify the generation of the detector signals at any detector position. The Folding-Method utilises part of the particle fluence spectra generated with the black-hole-method. The secondary particles entering the bottom of the detector box are convoluted, with respect to their kinetic energy, with pre-simulated detector response functions (described in chapter 5) to derive the detector signals. The detector position can be varied over the distance the particle spectra were scored, according to the needs. The gain in calculation speed compared to the black-hole-method is more than a factor of 10. It is suggested to utilise this method for the LHC BLM threshold calculations.

6.4.1 Description of the Simulation

A general description of the performed simulation, including all three methods, is given in this section.

The geometry was modeled as shown in Figure 6.1 and Figure 6.2. Additionally, some iron pieces beside the dump and one above detector position 5 were implemented to increase the number of backscattered particles (mainly concerning neutrons and gammas). The detectors are placed for the combined-simulation on top of the dump with a longitudinal spacing of about 1 m, as in the experiment. For the black-hole-method the detectors are replaced by a long detector box which covers all six detectors.

The primary proton beam is launched 0.5 m before the dump with an angle of 1 mrad in the negative y-axis direction. The real beam size which is at low energy $2\sigma \simeq 10$ mm and at high energy $2\sigma \simeq 2$ mm, and the transverse beam profile were neglected. Instead the simulations were performed with a pencil beam. In section 6.3.1 the beam properties are described. In the experiment, the beam is diverted up-stream of the dump and swept over a defined area on the

dump. This beam sweep was not implemented in the simulation. Instead, the extreme positions were simulated. At low energy (39 GeV) the first bunch of protons hits the dump at $y = -6.0\text{ mm}$ and bunch number 28 impacts at about $y = -61.0\text{ mm}$, which is the maximum at both energies. For high energy the first bunch impacts at about $y = -7.0\text{ mm}$. The distances are relative to the centre of the carbon-filling piece. 5.5 cm of carbon corresponds to $0.29 X_0$ and $0.14 \lambda_0$. The end of the beam pipe wall with a thickness of 3.5 mm, which is 30 cm before the dump and the screen monitor are not implemented. In iron this corresponds to $0.2 X_0$ and $0.02 \lambda_0$. It was shown that the beam pipe wall has no influence on the results within the uncertainties.

As previously mentioned, the beam dump is designed to absorb 98% of the beam energy. Therefore, the generation of enough statistics in the results needs a lot of calculation power. Introducing regions speeded up the simulation. Geant4 offers the possibility to combine several volumes to a region and set there a specific range cut value. The range cut value is explained in more detail in chapter 4. The inner core, the surrounding tube, the bottom and the sidewalls of the dump were combined to region I. The range cut value for region I was set to 10 cm and in the latest versions of the simulation to 19 cm. In the remaining volumes, which are the top plate of the dump, the additional pieces around the dump and the world volume filled with air, the range cut value was set to 1 mm. The gain in speed is about a factor of 2 to 3 compared to an overall range cut value of 1 mm. The results are most likely not influenced as the top wall thickness is 20 cm and the detector wall has a thickness of 2 mm. Typically, $1 \cdot 10^4$ to $2 \cdot 10^4$ protons were launched in the dump simulation. The calculation time for a single run with 10^4 primary protons is approximately 250 h of normalised CPU-time (CERN Batch Services [52]). The final results were obtained by launching about $9 \cdot 10^4$ primary protons at 920 GeV and about $8 \cdot 10^5$ protons at 39 GeV. In the combined-simulation the range cut value in region I is kept. For the remaining geometry parts, including the detectors, a range cut value of 0.05 mm was set. This smaller range cut value was utilised to decrease the systematic uncertainties on the detector signal (see section 5.2.4).

To derive the final detector signal in the black-hole-method the previously scored particles are reloaded in Geant4. The energy, momentum direction, type and position of the particles were recorded. Each detector is simulated separately. The dump is not included in the simulation. The previously recorded secondary particles act now as primary particles. They are launched as recorded and the energy deposition in the sensitive detector volume is scored. The details of the detector simulation are described in chapter 5.

The particle fluence spectra generated with the black-hole-method are compared for high energy at detector positions 2 and 4 in section 6.4.3. All generated spectra are shown in appendix A.6.

A final summation and the conversion from deposited energy to charge is performed by utilising the W-factor (see chapter 5). These results are compared in section 6.5 to the measurements.

As part of a collaboration the HERA proton beam dump was implemented and simulated in with FLUKA. The FLUKA spectra were kindly provided for comparison [50]. The secondary particle fluence spectra were derived by utilising a similar black-hole-method. At each detector position on the dump a sensitive detector volume was placed. All particles entering the box are recorded and artificially stopped. The provided scored particle data files included again all the necessary particle properties. The detector signal simulation was once more performed with Geant4 (QGSP-BERT-HP). The FLUKA files had to be modified due to a different coordinate system utilised in the FLUKA simulation compared to the Geant4 simulation. A biasing was introduced in the FLUKA simulations, which decreases the CPU-time. Therefore, a larger number of primary protons could be launched, which leads to an increase in statistics of secondary particles entering the detector volumes. Biasing applies a statistical weight to each particle, which is considered

as well in the Geant4 detector simulation. The sum of the deposited energy for each particle (originating from FLUKA) is multiplied by its corresponding statistical weight. The number of primaries impinging on the dump in the FLUKA simulation were $9 \cdot 10^6$ protons for 920 GeV and $3.6 \cdot 10^7$ protons for 39 GeV.

6.4.2 Estimation of Required Primary Proton Number

The statistical uncertainties on the simulated detector signal were estimated to determine the required number of primary protons necessary to derive statistical errors below 10% on the detector signals. Geant4 simulations at 920 GeV with QGSP-BERT-HP (black-hole-method) were performed. Five simulation runs, each with 4000 primary protons, were conducted. The different detector signals at detector 1 are compared. From the 4000 primary protons about 30 led to an energy deposition in the detector. The maximum difference between the single detector signals is up to 60%. The average for $2 \cdot 10^4$ primary protons is 0.46 pC/p with an error on the mean of 0.06 pC/p which is about 14%. The error is proportional to one over the square root of the number of primary protons. Therefore, more than $4 \cdot 10^4$ primary protons are needed to decrease the error on the mean below 10%.

As mentioned, the final simulation runs at high energy are performed with up to $9 \cdot 10^4$ primary protons. The resulting error on the mean of detector 1 is about 7%, which confirms the estimation.

6.4.3 Comparison of Spectra

Different physics lists of Geant4 and FLUKA were utilised in the black-hole-method to perform the particle spectra simulations. These particle fluence spectra are analysed in more detail. For each detector a plot of the spectra was generated which are shown in appendix A.6. The logarithm of the particle energy is utilised for the abscissa of the histograms. For a better visualisation an adequate way to show the spectra is fluence per lethargy [cm^{-1}] (see section A.4). Only particles entering the bottom of the 12 cm broad and 650 cm long detector box at the corresponding detector position are taken into account. The particle fluence spectra are normalised to a surface of $34 \text{ cm} \times 12 \text{ cm} = 408 \text{ cm}^2$ and to the number of primary particles.

Table 6.6: Multiplication factors between the spectra at each detector position relative to the one at position 2 for 39 GeV and 920 GeV, QGSP-BERT-HP.

energy	sp 1/sp 2	sp 2/sp 2	sp 3/sp 2	sp 4/sp 2	sp 5/sp 2	sp 6/sp 2
39 GeV	0.422	1.000	0.315	0.070	0.006	0.001
920 GeV	0.171	1.000	0.598	0.244	0.039	0.003

The particle fluence spectra at 920 GeV are shown for detector 2 and detector 4 and are compared to each other. Figure 6.14 and Figure 6.15 show the spectra for the QGSP-BERT-HP physics list. Figure 6.16 and Figure 6.17 show the spectra for the FTFP physics list and Figure 6.18 and Figure 6.19 represent the spectra simulated with FLUKA.

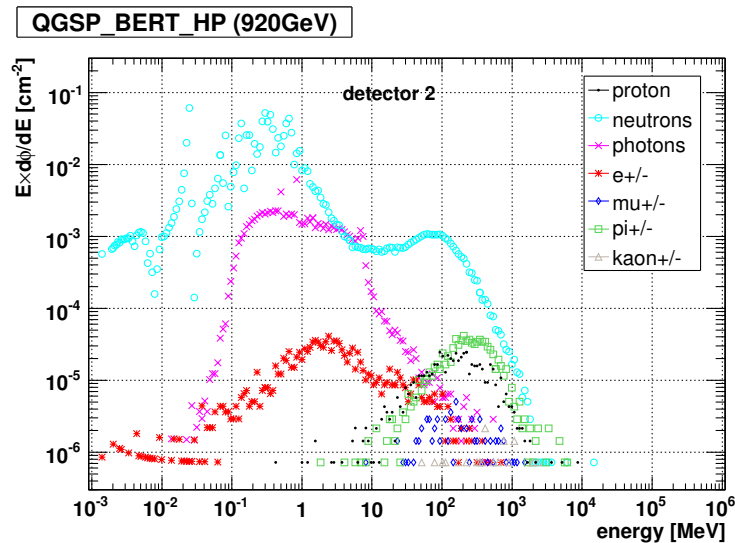


Figure 6.14: Secondary particle fluence spectra on top of the HERA dump arriving at detector 2. QGSP-BERT-HP, 920 GeV.

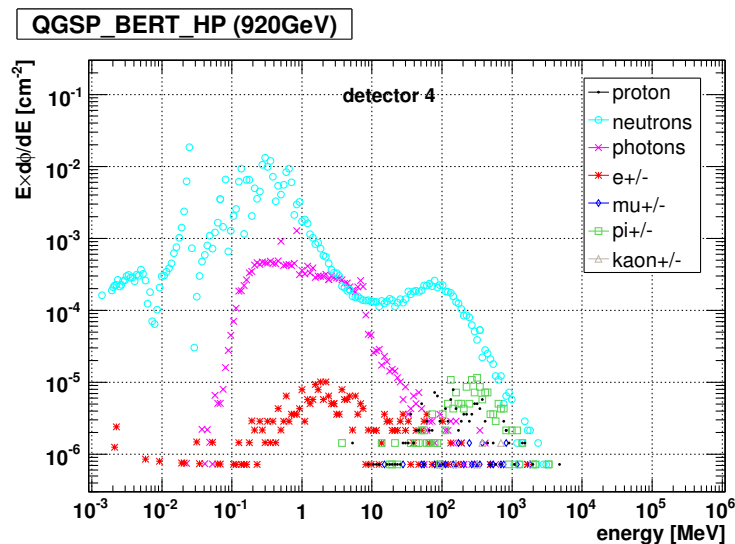


Figure 6.15: Secondary particle fluence spectra on top of the HERA dump arriving at detector 4. QGSP-BERT-HP, 920 GeV.

The spectra at the different detector locations differ mainly in absolute height. The energy range of the particles is between a few tens of keV up to about 2 GeV. With QGSP-BERT-HP neutrons are the main part of the spectra followed by gammas. Following the neutron spectrum from 2 GeV to lower energies it shows a first peak at 100 MeV, at about 1 MeV it reaches a maximum. At 10 MeV the number of neutrons is the same as for gammas. All other particle types are at least one order of magnitude below the neutrons. Between 100 MeV and 1 GeV charged hadrons have their maximum, electrons and positrons have a maximum at a few MeV in their spectra. The spectra between the different detector positions differ only in height and do not change in particle composition. For the spectra simulated with QGSP-BERT-HP at 39 GeV and 920 GeV the ratio between the spectra at each detector position to the one at detector position 2 was calculated. The multiplication factors are printed in Table 6.6. These factors are dominated by the neutrons as they dominate each spectrum. In the ratio plots it is shown that for each comparison a constant factor for all particle types and energy bins appeared. The only exception

is the spectrum at detector 1. Their the relative ratio of lower energetic neutrons is higher than at position 2.

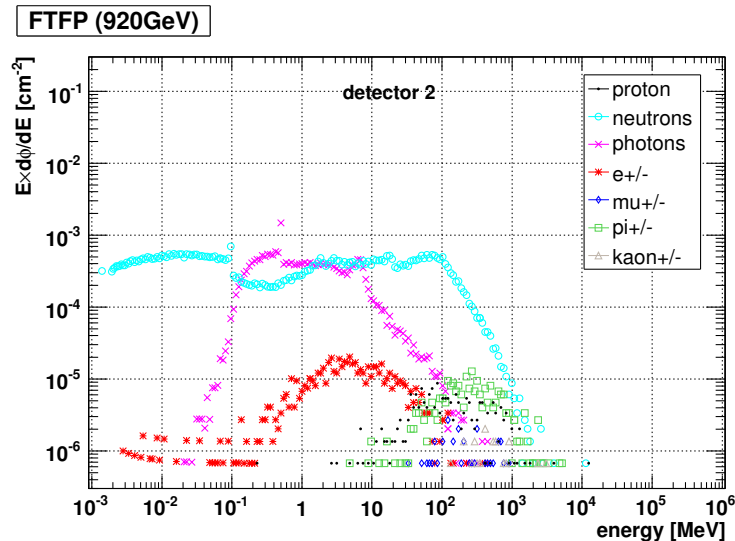


Figure 6.16: Secondary particle fluence spectra on top of the HERA dump arriving at detector 2. FTFP, 920 GeV.

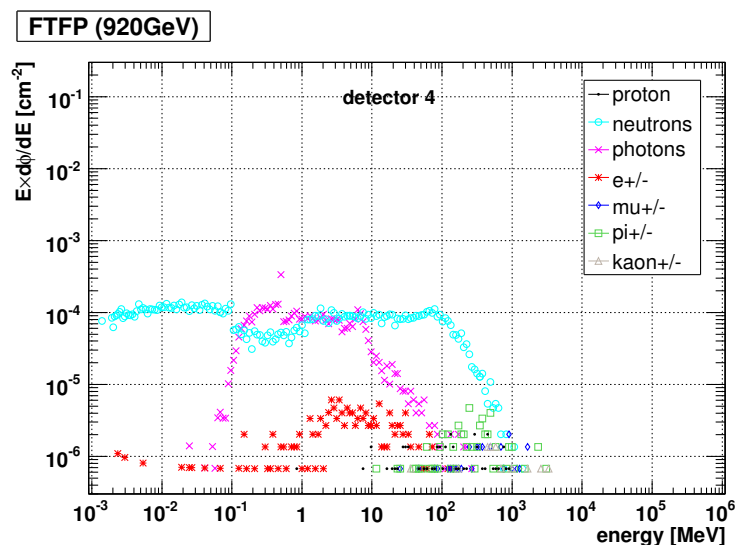


Figure 6.17: Secondary particle fluence spectra on top of the HERA dump arriving at detector 4. FTFP, 920 GeV.

For neutrons the spectra produced with FTFP are quite different to the ones produced with QGSP-BERT-HP. The energy range in which the particles appear is again between about 100 keV and 2 GeV. The neutron spectrum has a plateau up to about 100 MeV and slope down to zero at about 2 GeV. The total height is about a factor of 5 lower than in the QGSP-BERT-HP spectra and does not rise below 10 MeV. The shape of the gamma, charged hadron and electron/positron spectrum is similar as in QGSP-BERT-HP and their total height is a factor of 2 to 5 lower. From the lower number of secondary particles per impinging proton on the dump a lower simulated detector signal is expected. The two physics lists from Geant4 show an unexpected large difference in the particle fluence spectra profile as well as in the total height. This lead to lower simulated detector signals with FTFP.

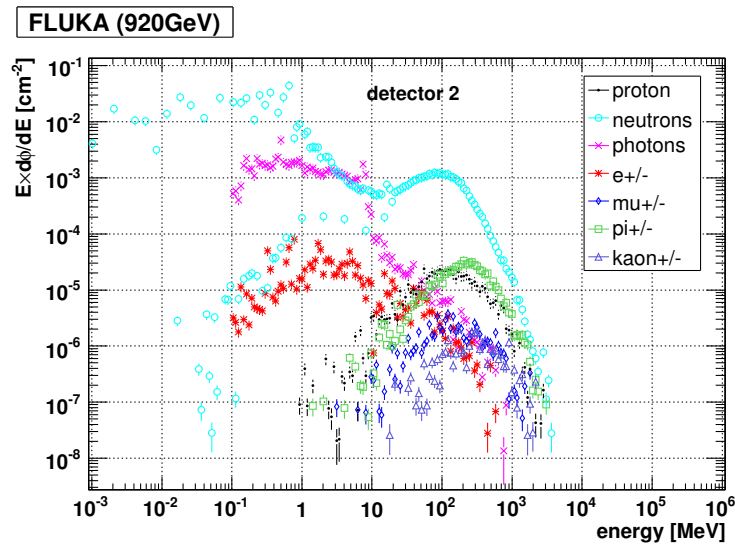


Figure 6.18: Secondary particle fluence spectra on top of the HERA dump arriving at detector 2. FLUKA, 920 GeV. Courtesy of R. Bruce.

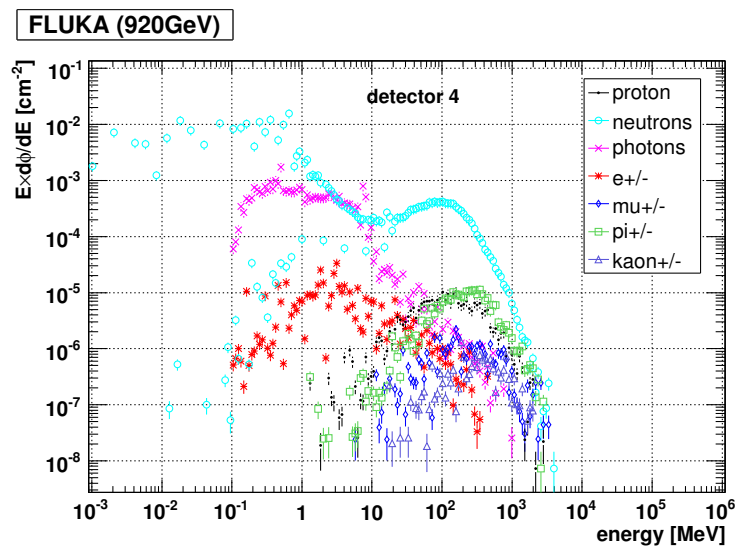


Figure 6.19: Secondary particle fluence spectra on top of the HERA dump arriving at detector 4. FLUKA, 920 GeV. Courtesy of R. Bruce.

A comparison between the spectra generated with FLUKA and the two spectra generated with Geant4 show that the FLUKA spectra are nearly identical to the ones produced with QGSP-BERT-HP. The FLUKA electron/positron spectrum and the gamma spectrum show an energy cut-off at 100 keV. The neutron spectrum shows a plateau at energies below 100 keV compared to the QGSP-BERT-HP neutron spectrum. As the Geant4, QGSP-BERT-HP and the FLUKA spectra are about identical, these two simulation methods are to prefer compared to Geant4, FTTP.

6.4.4 Escape Angle and Longitudinal Secondary Shower Profile

In section 6.4.8 are the black-hole-method and the Folding-Method compared. In the Folding-Method one of the pre-simulated detector response function is utilised, depending of the impact angle of the particles. The particle spectra produced with the black-hole-method include information of the particle position and the momentum vector. An analysis of the particles entering the bottom of the detector box which are the particles escaping from the dump in the centred, 12 cm broad and 650 cm long strip is performed. The results of this analysis are printed in Table 6.7. Shown are the mean escape angle at each detector position and the average of the absolute value of the escape angle shifted by 90° . The “modification” of the mean impact angle was performed, because regardless of a positive or negative impact angle of the particles the detector signal is equal. The average escape angle for the whole strip is about 90° and the modified average is about 65° . Out of the pre-simulated detector response function for different impact angles the one with 60° is closest to the modified mean escape angle of the secondary particles and therefore utilised in the Folding-Method.

Table 6.7: Average angles and modified average angle of the secondary particles leaving the top of the dump in a centred, 12 cm broad and 650 cm long strip.

detector	$\langle\vartheta\rangle$	$\langle abs(\vartheta - 90)\rangle$
1	78.41	63.32
2	91.35	64.75
3	91.85	64.65
4	93.23	63.8
5	94.69	63.17
6	102.9	60.82
total	90.39	64.67

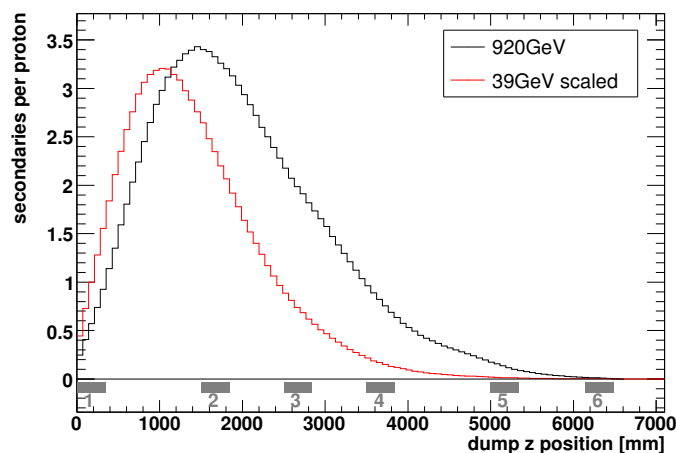


Figure 6.20: Secondary particles per primary proton versus longitudinal position on the dump for high and low beam energy.

Figure 6.20 shows the number of secondary particles entering the centred, 12 cm broad and 650 cm long strip versus the longitudinal position on the dump. The detector positions are marked with the numbered boxes. The distribution for 39 GeV is scaled by a factor of 10. At high beam energy the peak of the distribution is shifted to larger z -values and broader compared to 39 GeV.

6.4.5 Energy Deposition per Primary Proton

The energy deposition per impinging proton on the dump at the six detector positions for protons of 39 GeV is shown in Figure 6.21. For primary protons with 920 GeV the energy deposition distribution is shown in Figure 6.22. Both simulations are performed with QGSP-BERT-HP physics list. The deposited energy is logarithmically binned in 60 bins in an energy range of 1 eV to 1 GeV.

The entry “Integral” in the legend refers to number of entries in the histogram, zeros are not included (log-scale). The simulation was done for $7.9 \cdot 10^5$ protons. At 39 GeV the statistical error from the number of entries in the histogram corresponding to detector 1 to 4 is below 6%, at detector 5 22% and at detector 6 100%. At detector 2, which has the best statistics and the highest detector signal, only in 0.5% of all events is energy deposited. At detector 5 and 6 the ratio of events to number of primary protons is $2 \cdot 10^{-5}$ and $1 \cdot 10^{-6}$, respectively.

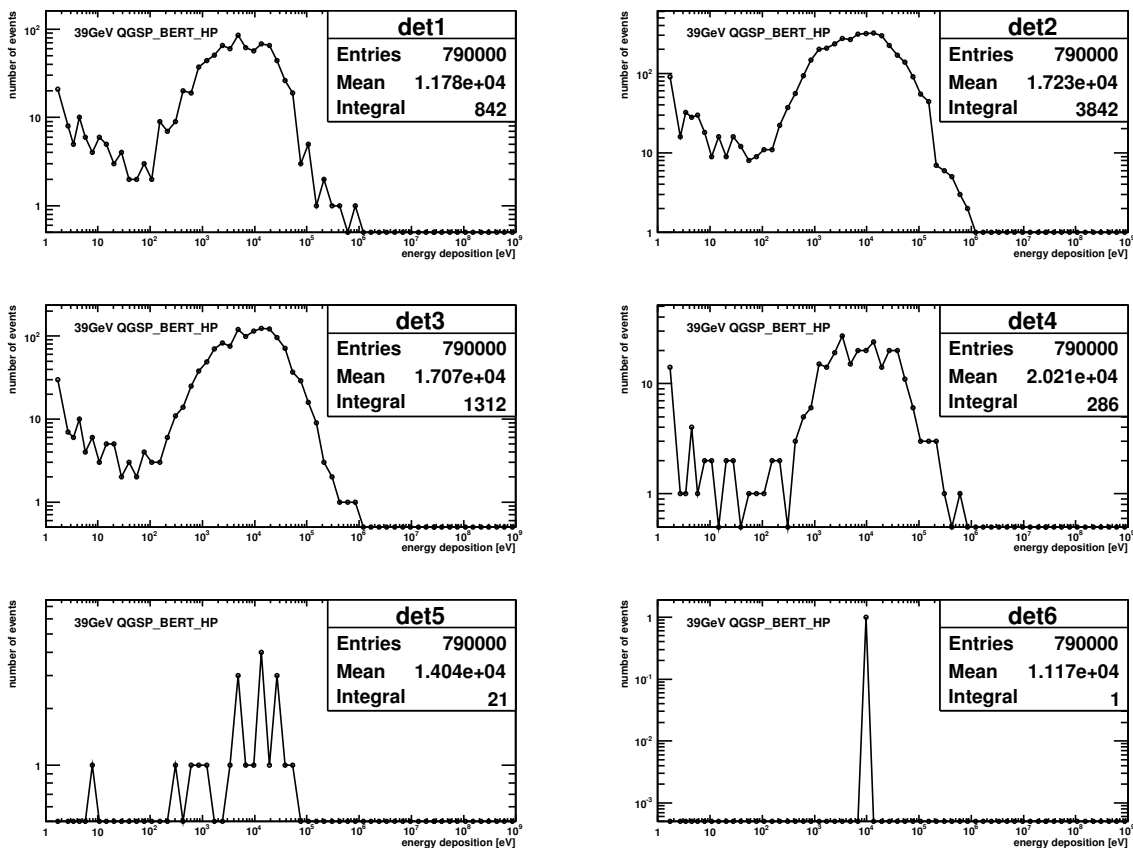


Figure 6.21: Energy deposition at the different detector positions for protons at 39 GeV. The deposited energy is logarithmically binned in 60 bins in the range of 1 eV to 1 GeV.

At 920 GeV $9 \cdot 10^4$ primary protons were simulated. One can see in Figure 6.22 that the number of events in which energy is deposited is higher than at 39 GeV, even though there were nearly 9 times less primary protons launched. At detector 2 in 6% of all events is energy deposited, at detector 5 its only 0.2% and at detector 6 0.02%. To increase the statistics at the more distant detector positions one can utilise a larger number of primary protons and/or introduce biasing in the simulation.

The largest amount of energy deposition in a single event is clearly found at 920 GeV. In detector

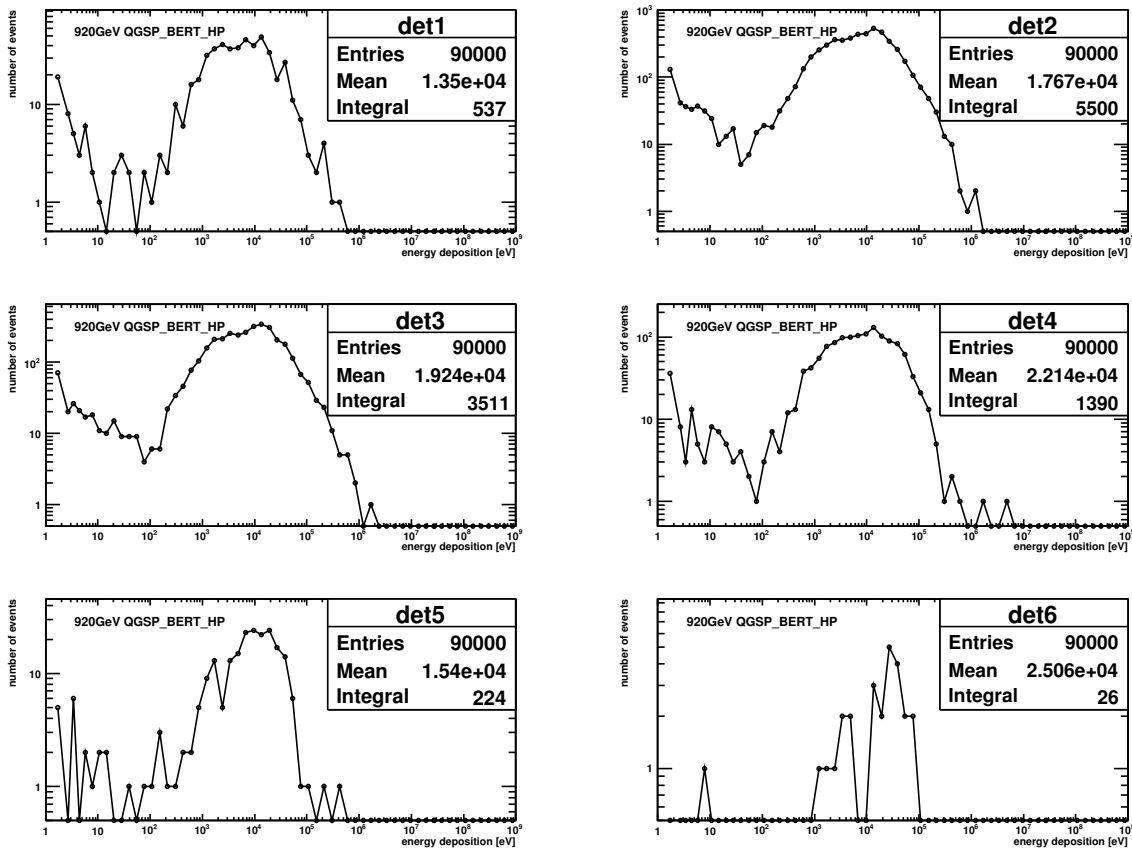


Figure 6.22: Energy deposition at the different detector positions for protons at 920 GeV. The energy deposition is logarithmically binned in 60 bins in the energy range of 1 eV to 1 GeV.

4 in some single events up to a few GeV is deposited. At low energy the maximum is about 1 GeV. The most probable energy deposition is about 10 keV for all positions and both energies. This is represented by the shape of the shown energy deposition distribution, which are similar for all detector positions.

6.4.6 Simulation Results

The simulated detector signals at 39 GeV versus detector position for different Monte Carlo codes are compared in Figure 6.23. A comparison of the simulated results for 920 GeV is shown in Figure 6.24. The points in the plots are separated by 15 mm on the abscissa for a better visualisation. Compared are for both energies simulations performed with QGSP-BERT-HP, FTFP and LHEP-BIC-HP physics lists from Geant4 and FLUKA (courtesy of R. Bruce). All results are produced with the black-hole-method, except for Geant4, LHEP-BIC-HP for which the combined-simulation method was utilised.

The detector numbers are counted with increasing distance from the impact point of the primary protons, from 1 to 6 and are indicated as boxes. The errors are the statistical errors from the simulation. At 39 GeV all simulations, except FTFP, agree roughly within 30%. Detector 2 has the highest signal as it is closest to the shower maximum. The FLUKA simulations show at most detector positions the highest response followed by Geant4, QGSP-BERT-HP. The response for

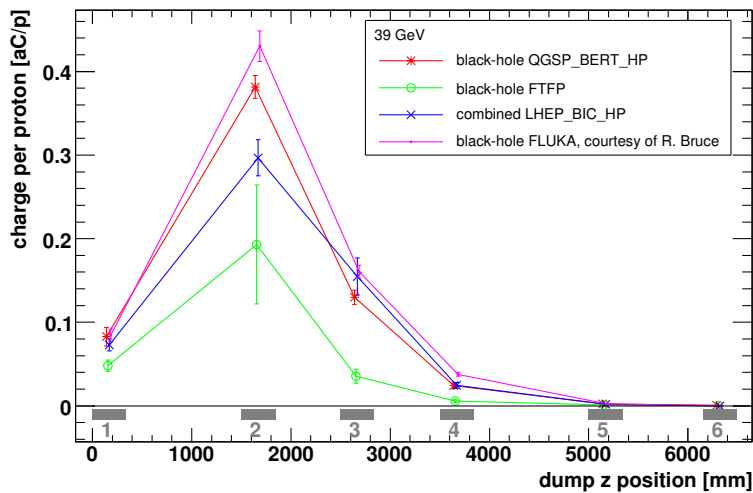


Figure 6.23: Comparison of the simulated detector signals at different detector positions (QGSP-BERT-HP, FTFP, LHEP-BIC-HP and FLUKA) at 39 GeV.

LHEP-BIC-HP is at detector 2 below FLUKA and QGSP-BERT-HP, but at the other positions close to these. In the discussion of the Geant4 particle fluence spectra, FTFP showed already a lower number of secondaries, which results in the observed lower detector response for the first four detectors. At detectors 5 and 6 the results for all simulations are about the same and are within the statistical errors. For the simulations produced at 39 GeV no significant difference between Geant4 QGSP-BERT-HP and FLUKA is observed.

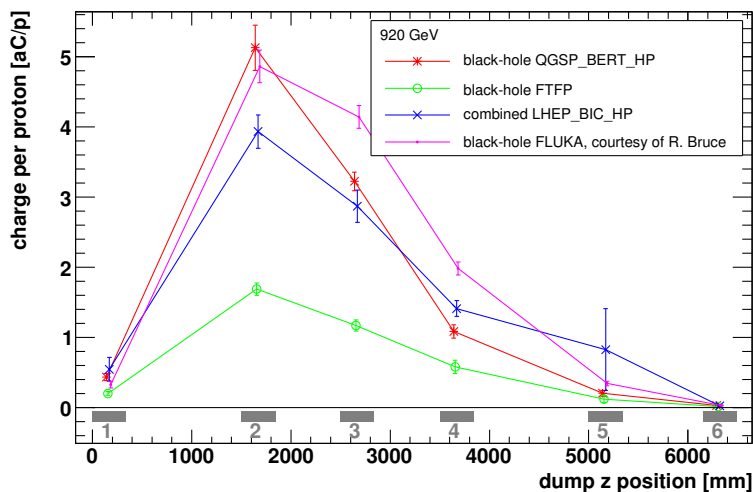


Figure 6.24: Comparison of the simulated detector signals at different detector positions (QGSP-BERT-HP, FTFP, LHEP-BIC-HP and FLUKA) at 920 GeV.

The simulation results for a primary proton energy of 920 GeV, plotted in Figure 6.24, show a larger variation between the different models as at 39 GeV. Geant4 QGSP-BERT-HP and LHEP-BIC-HP and FLUKA have at all detector positions roughly the same results but Geant4 FTFP is more than a factor of two lower. Other differences are observed for LHEP-BIC-HP at detector 2 and for FLUKA at detector position 3 and 4. LHEP-BIC-HP seems to underestimate at detector 2 the detector response which was seen as well for the low energy results in Figure 6.23. In the

FLUKA results for detector 3 and 4 a higher signal compared to QGSP-BERT-HP is observed which indicates that FLUKA generated a broader shower.

Table 6.8: Ratios between the two proton impact points on the dump. The high position refers to $y = -6\text{ mm}$ and the low position to $y = -61.0\text{ mm}$, relative to the centre of the carbon filling piece.

QGSP-BERT-HP						
39 GeV						
	high impact position		low impact position		high/low	
detector	signal [aC/p]	error	signal [aC/p]	error	ratio	error
1	0.083	0.011	0.069	0.015	1.195	0.302
2	0.382	0.014	0.322	0.016	1.185	0.072
3	0.130	0.009	0.082	0.005	1.574	0.144
4	0.024	0.003	0.033	0.018	0.743	0.407
5	2.4e-3	7.1e-4	1.5e-3	4.5e-4	1.636	0.706
6	7.4e-4	4.4e-4	9.5e-5	9.5e-5	7.754	9.025
920 GeV						
	high impact position		low impact position		high/low	
detector	signal [aC/p]	error	signal [aC/p]	error	ratio	error
1	0.434	0.050	0.366	0.067	1.184	0.256
2	5.128	0.324	4.387	0.505	1.169	0.153
3	3.222	0.133	2.477	0.170	1.301	0.104
4	1.082	0.094	0.930	0.129	1.164	0.191
5	0.203	0.043	0.095	0.020	2.148	0.639
6	0.029	0.008	0.006	0.003	4.767	2.826

In the experiment the proton beam is swept over a defined area on the dump which is described in section 6.3.1. An estimate of the uncertainties due to the sweep is performed. Two separated simulations with a beam impinging at the extreme positions of the sweep area were conducted (with QGSP-BERT-HP). The beam is impacting relative to the inner core centre at $y = -6\text{ mm}$ and $y = -61.0\text{ mm}$. A comparison of the results is shown in Table 6.8. The simulations were performed for both energies, 39 GeV and 920 GeV, with about $8 \cdot 10^5$ and $9 \cdot 10^4$ primary protons respectively. At detector 1 the difference in amount of material the shower particles have to traverse is 5.5 cm in Carbon which is about $0.14 \lambda_0$. At detectors 1 and 2 the difference in signal between the two impacting points is less 20%. Detector 3 shows at 39 GeV a difference of 57% and at 920 GeV a difference of 30%. At detector 4 the signals from the lower impact position (39 GeV) shows a higher signal probably due to statistical fluctuations. An average difference of 20% for the first four detectors is estimated.

In the experiment, the mean impact position of the proton beam is close to the centre of the sweep area. The presented simulation results in this chapter are performed at the upper beam impact position ($y = -6\text{ mm}$ relative to the centre of the inner core). Therefore, an estimated systematic uncertainty of 10% is taken into account.

The statistical errors are about 8%. Different systematic errors in the simulations are estimated and shown in table 6.9. The contribution of particles, reflected or created at the tunnel walls to the signal is estimated to 5%. The detector response functions and therefore the detector signal simulations have a systematic error of 17%. By neglecting the beam sweep on the dump a systematic error of 10% is introduced. From the different results obtained with Geant4's QGSP-

BERT-HP physics list and FLUKA a systematic error in the shower simulations from the different tracking codes is estimated to 20%. This estimate is from the largest differences found between the Geant4 and FLUKA results for the first four detectors, which is about 40% and is considered as two sigma. A totalised systematic error on the simulation results is 29%, which is applied to the final results for the comparison to the measurements.

Table 6.9: Systematic errors estimated for the HERA dump simulation.

systematic error	
tunnel walls	5%
detector signal simulation	17%
simplified beam position	10%
simulation model	20%
totalised systematic error	29%

6.4.7 Validation with the Combined-Simulation

A validation for the black-hole-method, which is the main method to generate the detector signal, is introduced by the combined-simulation method, which is equivalent. The cross-check is performed with the QGSP-BERT-HP and the FTFP physics list of Geant4.

The results for the two approaches are shown in Figure 6.25. The left plot corresponds to 39 GeV and right plot to 920 GeV. It is shown that the two methods produce results within the statistical uncertainties. The only difference was found at 920 GeV at detector 2 with FTFP.

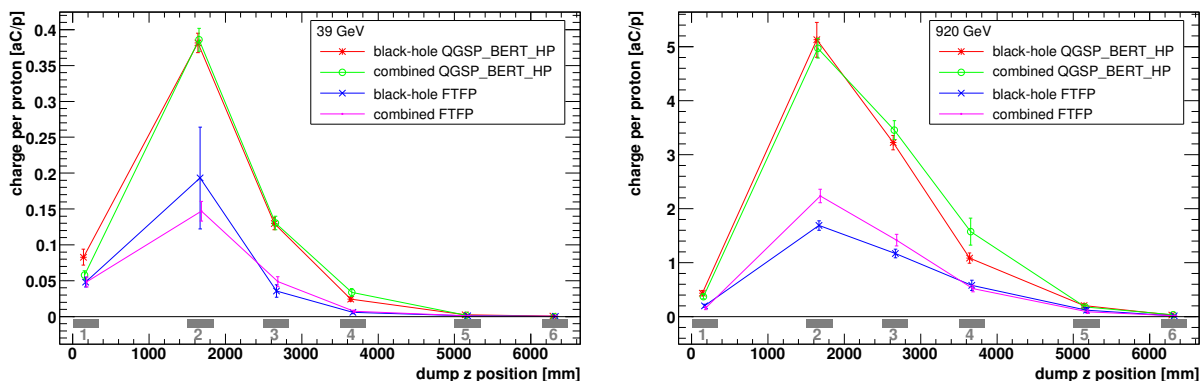


Figure 6.25: Comparison between the results from the black-hole-method and the combined-simulation. Left: 39 GeV. Right: 920 GeV.

6.4.8 Validation with Folding-Method

In chapter 5 detector response functions are presented. With these response functions the particle fluence spectra derived in the black-hole-method are convolved to derive the detector signal. Any detector position in the scoring range (longitudinal distance) of the spectra is possible, which provides a simple and fast way to generate the detector signal.

Table 6.10: Comparison of the generated detector signals for the black-hole-method and the Folding-Method at 39 GeV.

QGSP-BERT-HP [aC/p] at 39 GeV						
detector	simulated	error	folded	error	ratio	error
1	8.28e-2	1.12e-2	8.03e-2	3.57e-3	1.03	0.15
2	3.82e-1	1.35e-2	4.17e-1	1.22e-2	0.92	0.04
3	1.30e-1	8.66e-3	1.29e-1	7.10e-3	1.00	0.09
4	2.44e-2	2.98e-3	2.35e-2	2.83e-3	1.04	0.18
5	2.39e-3	7.11e-4	1.47e-3	4.42e-4	1.63	0.69
6	7.38e-4	4.39e-4	1.94e-4	1.94e-4	3.81	4.43
FTFP [aC/p] at 39 GeV						
detector	simulated	error	folded	error	ratio	error
1	4.82e-2	6.82e-3	4.20e-2	2.18e-3	1.15	0.17
2	1.93e-1	7.10e-2	1.15e-1	5.81e-3	1.68	0.62
3	3.56e-2	8.57e-3	2.83e-2	3.23e-3	1.26	0.34
4	5.74e-3	1.66e-3	5.13e-3	1.36e-3	1.12	0.44
5	9.74e-4	4.60e-4	1.83e-4	1.83e-4	5.32	5.88
6	4.23e-4	3.22e-4	1.12e-4	1.12e-4	3.78	4.76

The pre-simulated detector response functions are put into a logarithmically binned histogram. As not all energy steps were simulated the empty bins are filled by linear interpolation. The detector response function simulations were performed for particles impinging uniformly and parallel to each other under different angles on the detector cross section. In section 6.4.4 an investigation on the escape angle of the particles from the top of the dump was conducted. An average angle of 65° was derived. Out of the pre-simulated response functions the one conducted with an impact angle of the particles of 60° fits the requirements best. The particle fluence spectra are binned with the same bin size, which allows a bin multiplication of the two histograms for each particle type. Only the part of the particles in the spectra which are recorded at the location of the projected detector surface are taken into account. The projected surface of the detector is a 34 cm long and 12 cm wide strip which is derived from the detector height of 12 cm times the cosine of the mean impact angle of 60° plus the detector length of 28 cm. The total detector signal is derived by integrating over all energy bins and particle types.

The results of the Folding-Method and the cross-check with the results derived with the black-hole-method are presented in Table 6.10 for 39 GeV and in Table 6.11 for 920 GeV. Both methods utilise the same spectra derived from the black-hole-method with either QGSP-BERT-HP or FTFP corresponding to the primary proton energy. The errors include the statistical error on the detector response functions and the statistical errors in the particle fluence spectra. An error of 100% is utilised for the results of the Folding-Method at 39 GeV with the QGSP-BERT-HP physics list at detector 6 and for the FTFP physics list at detector 5 and 6.

A systematic uncertainty for the Folding-Method is estimated from the comparison of the results from the first four detectors generated with QGSP-BERT-HP. The largest total error was obtained at detectors position 4 at low energy, which is 4% with an error of 17%, which results in a total error of 18%.

The most interesting detector positions for the LHC BLM thresholds are between detector 1

Table 6.11: Comparison of the generated detector signals for the black-hole-method and the Folding-Method at 920 GeV.

QGSP-BERT-HP [aC/p] at 920 GeV						
detector	simulated	error	folded	error	ratio	error
1	0.43	0.05	0.41	0.02	1.05	0.13
2	5.13	0.32	5.16	0.11	0.99	0.07
3	3.22	0.13	3.08	0.09	1.04	0.05
4	1.08	0.09	1.12	0.05	0.96	0.10
5	0.20	0.04	0.17	0.02	1.23	0.31
6	0.03	0.01	0.02	0.004	1.71	0.60
FTFP [aC/p] at 920 GeV						
detector	simulated	error	folded	error	ratio	error
1	0.20	0.03	0.17	0.01	1.16	0.18
2	1.69	0.09	1.79	0.07	0.94	0.06
3	1.17	0.08	1.13	0.05	1.04	0.08
4	0.58	0.09	0.37	0.02	1.58	0.28
5	0.12	0.05	0.05	0.01	2.22	0.98
6	0.01	0.01	0.01	4.19e-7	2.29	0.89

and 4 which corresponds to a range in distance of $z=0$ to $z=3.5$ m after the impact point of the protons. The results for the QGSP-BERT-HP particle spectra show in this range an agreement better than 10% at low and high energy. This shows the good agreement between the two methods in the interesting range.

The results derived for the FTFP generated spectra show at low energy for detectors 1, 3 and 4 a good agreement, which is within 26%, only detector 2 shows a difference of 68%. At 920 GeV the difference between the two methods at the first three detectors is within 16%. Detector 4 shows for this case a difference of 58%.

For both energies and both Geant4 physics lists the results for detector 5 and 6 have large statistical uncertainties. This is due to the few particles depositing energy in the detectors. Within these large errors the agreement is satisfactory.

In conclusion, the two equivalent methods to derive the detector signal, black-hole-method and Folding-Method, show similar results for QGSP-BERT-HP generated particle spectra. Each of the two can be utilised to calculate LHC BLM detector thresholds.

6.5 Comparison of Measurements and Simulations

In this section the HERA proton beam dump measurements are compared to simulations performed with Geant4 and FLUKA. The measured signals are converted with the calibration factors from the electronics and the space charge effect correction is applied. The final measurement results are derived by calculating the average between the normalised signal maximum and the normalised signal minimum in the beam intensity range from $1.2 \cdot 10^{12}$ to the maximum number of protons. For the same beam intensity range the error on the results is calculated. The difference

between the maximum and the minimum relative response is considered to be four sigma. The final errors shown in the results comprises additionally systematic uncertainties which are, less than 0.1% from remanent radiation, 2% from the proton beam intensity measurements, 10% from the electronics calibration and between 1% to 10% from detector misalignment (see section 6.3.7).

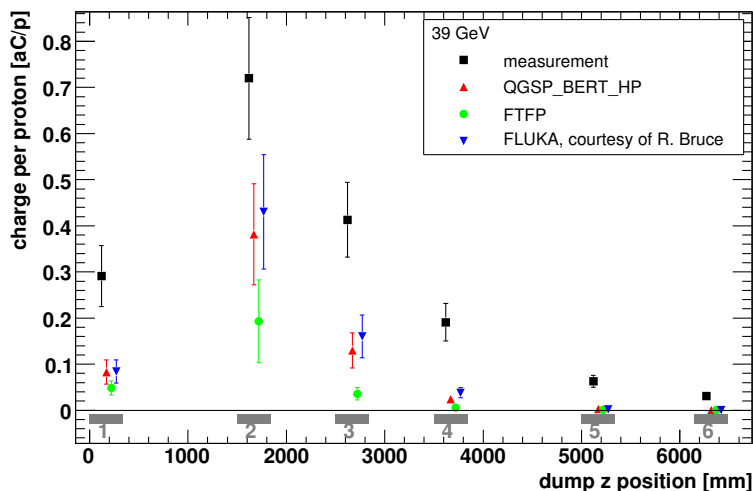


Figure 6.26: Comparison between the space charge corrected measurements and the simulations performed with different Monte Carlo codes, at 39 GeV. A systematic error of 10% is included in the simulation results.

The simulation results utilised for the comparison are obtained with the QGSP-BERT-HP and FTFP physics lists from Geant4 and the FLUKA simulation results [50]. The errors on the simulation results shown include the statistical errors (below 13%) and different systematic errors (see section 6.4.6).

Table 6.12: Relative differences between the simulations at injection energy and the space-charge-effect corrected measurements. The relative residuals are calculated as (measurement - simulation)/measurement.

39 GeV detector	QGSP-BERT-HP	error	FTFP	error	FLUKA	error
1	0.72	0.29	0.83	0.30	0.71	0.29
2	0.47	0.25	0.73	0.26	0.40	0.26
3	0.69	0.25	0.91	0.27	0.61	0.25
4	0.87	0.29	0.97	0.30	0.80	0.28
5	0.96	0.28	0.98	0.29	0.96	0.28
6	0.98	0.27	0.99	0.27	0.99	0.27

In the experiment the beam is swept over the dump, a fact neglected in the simulation. Instead, the extreme positions of the beam sweep were simulated. The difference in detector signal (see Table 6.8) between the furthest position and the closest position in respect to the detector locations was about 20%. The simulation results for the closer position are utilised in the comparison with the measurements with an error of 10%. Additional systematic uncertainties are, less than 5% from reflected or created particles at the tunnel walls, 17% systematic uncertainty for the detector response functions and 20% systematic uncertainty between the utilised simulation codes.

The total systematic error on the simulation results is 29%. The statistical errors are below 13% for the first four detectors in the simulation with QGSP-BERT-HP.

Figure 6.26 shows the results at the injection energy of 39 GeV. The corresponding relative differences are printed in Table 6.12. The relative differences are calculated as the difference between measurement results and simulation results divided by the measurement. All simulations show an overall lower signal than the measurements. In absolute numbers the simulations results from FLUKA are closest to the measurements, followed by QGSP-BERT-HP. The difference at detector 2 is about 40% for FLUKA and 46% for QGSP-BERT-HP. FTFP shows a difference of 73% from the measurements at detector 2. For detectors 1 and 3 the results between measurement and the simulations with FLUKA and QGSP-BERT-HP are still within 70%. The results for the other detectors agree less. All simulations at 39 GeV do not reproduce the tail of the showers very well.

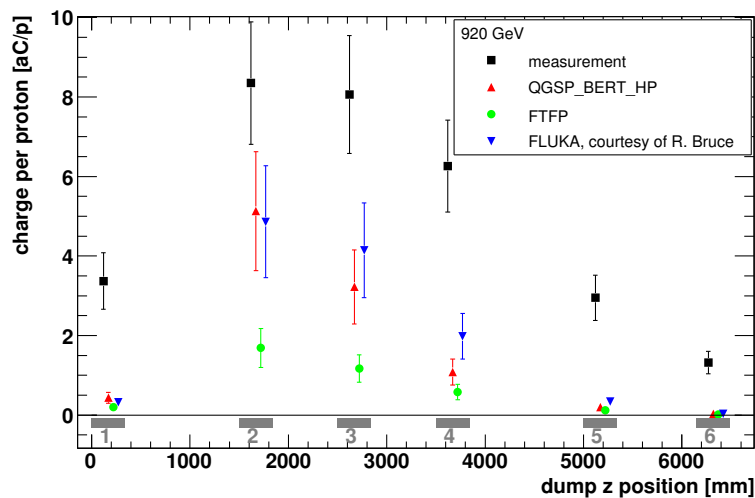


Figure 6.27: Comparison between the space charge corrected measurements and the simulations performed with different Monte Carlo codes, at 920 GeV. A systematic error of 10% is added in the simulation results.

Table 6.13: Relative differences between the simulations at high energy and the space-charge-effect corrected measurements. The relative residuals are calculated as (measurement - simulation)/measurement.

920 GeV detector	QGSP-BERT-HP	error	FTFP	error	FLUKA	error
1	0.87	0.28	0.94	0.29	0.90	0.29
2	0.39	0.27	0.80	0.24	0.42	0.26
3	0.60	0.24	0.86	0.25	0.49	0.25
4	0.83	0.24	0.91	0.25	0.68	0.24
5	0.93	0.27	0.96	0.27	0.88	0.26
6	0.98	0.30	0.99	0.30	0.98	0.30

The results for high energy (920 GeV) are shown in Figure 6.27 and the corresponding relative differences in Table 6.13. Again, all simulated results are lower than the measurements for each detector. At detector 2 all simulations show the highest signal and the smallest relative difference

to the measurement. Here, QGSP-BERT-HP and FLUKA agree with the measurements to within 40%, FTFP is only within 80%. At detector position 1 all simulations show a difference of about 90% to the measurements. This behaviour is not understood. FLUKA shows for detector 3 and 4 still a good agreement. In absolute numbers FLUKA describes the measurement results best.

The simulation results generated with QGSP-BERT-HP for low and high energy and the comparison to the measurements are summarised in Table 6.14.

Table 6.14: Comparison of the simulation results to the measurement results at 39 GeV and 920 GeV. The simulations are performed with QGSP-BERT-HP. The measurements are space charge effect corrected.

39 GeV						
	signal [aC/p]				sim/meas	
detector	simulated	error	measured	error	ratio	error
1	0.083	0.026	0.291	0.066	0.284	0.110
2	0.382	0.110	0.720	0.132	0.530	0.181
3	0.130	0.038	0.413	0.081	0.314	0.111
4	0.024	0.008	0.191	0.041	0.128	0.048
5	2.39e-3	9.84e-4	0.063	0.013	0.038	0.017
6	7.38e-4	4.87e-4	0.031	0.006	0.024	0.016
920 GeV						
	signal [aC/p]				sim/meas	
detector	simulated	error	measured	error	ratio	error
1	0.434	0.133	3.370	0.712	0.129	0.048
2	5.128	1.498	8.350	1.538	0.614	0.212
3	3.222	0.929	8.060	1.483	0.400	0.137
4	1.082	0.323	6.260	1.153	0.173	0.061
5	0.203	0.072	2.950	0.570	0.069	0.028
6	0.029	0.012	1.320	0.285	0.022	0.010

At the LHC the beam loss monitors are mounted in a range of about $z=0.5$ m to $z=3.5$ m after the impact point of the lost protons. QGSP-BERT-HP and FLUKA show for the HERA dump experiment similar results in this range. In terms of nuclear interaction length the HERA proton beam dump compared to an LHC magnet provides an upper limit. For a detector position closer to the shower core the simulation results are expected to have a better agreement with the experiments. A maximum of 50% of systematic errors for the $z=0$ m to $z=3.5$ m range is expected. The QGSP-BERT-HP physics list of Geant4 and FLUKA are proposed for the LHC BLM threshold simulations.

6.6 Summary

Measurements and simulations with the LHC BLM system were carried out at DESY's HERA proton beam dump to estimate the uncertainties between hadronic shower simulations and measurements.

In the measurements on the dump the ionisation detector showed a non-linear behaviour in

respect to the beam intensity. The linearity of the detector signal was considerably improved by applying a simplified space-charge-effect correction derived from previously published formulae. Thereby, a detector charge collection efficiency of only about 20% was found. The highest energy deposition of about 0.5 Gy resulted after space-charge-effect correction in approximately 2.5 Gy. For the LHC BLM detectors space-charge-effect is not an issue, as their operational range is a factor 2.5 below the ionisation rate at which space charge effects start to apply.

The detector signals were simulated with Geant4 and simulation data from FLUKA were provided for comparison. The detector signals were derived by three similar methods, which provided a consistent check for the simplified Folding-Method, which is utilised for the LHC BLM detector threshold generation.

In the comparison between simulation and measurement showed QGSP-BERT-HP (Geant4) and FLUKA similar results and describe the measurements more precisely than FTFP (Geant4). The simulated detector signal for detector 2 was within 50% to the measurements for QGSP-BERT-HP and FLUKA. Monte Carlo particle shower simulations describe the inner core of the shower more precisely as the shower tail. The detector positions in the tails of hadronic showers at the HERA proton beam dump are compared to positions at an LHC magnet further away from the core of the shower. This and the observed space charge effects are the main factors for the limited accuracy of the results.

The Geant4 physics list QGSP-BERT-HP and FLUKA are recommended for the LHC BLM detector threshold simulations.

For a typical mounting position of an LHC BLM detector which is at about $z=0.5$ m to $z=3.5$ m after the impact point of the lost protons a systematic uncertainty of 47% is estimated as follows.

The projected particle path length between impact point and detector location at the LHC magnet is about $10 \lambda_0$ (nuclear interaction lengths). The copper rod in the mixed radiation field measurement is in projected particle path length about $3 \lambda_0$ and the dump in the HERA experiment is about $16 \lambda_0$. The results from the four validation measurements described in chapter 5 were all within approximately 20%. At the HERA beam dump experiment the first 4 detectors were within 70% when comparing the simulations and measurements. Scaling these uncertainties with the projected particle path length results in an estimated uncertainty of 47% for the simulated LHC BLM detector thresholds.

This error estimate is valid for the whole operational range of the LHC BLM detectors, which is limited by the ionisation rate at which space charge effects start to apply.

Chapter 7

Estimation of an LHC BLM Detector Threshold

The initial systematic error of the whole acquisition chain of the LHC BLM system should be smaller than 5. Previously, to achieve this initial accuracy different simulations, including the detector response estimations and hadronic shower simulations, have been carried out [16]. These previous investigations focused on LHC arc cells including main dipoles and quadrupole magnets. The hadronic showers throughout the magnets were mainly simulated for point losses, with the Monte Carlo code Geant3 (predecessor of Geant4). The particles escaping from the cryostat were recorded in two strips, which were placed at the level of the beam pipe on each side of the magnet. Utilised were energy cut offs for electrons and positrons at 0.3 MeV and for charged hadrons and muons at 3.0 MeV. Each recorded particle was treated as minimum ionising particle. At the point in time of these investigations the detector type for the LHC BLM system was not defined. These investigations were performed for pin diodes, which are counting particles. The later values referred to as minimum and maximum value are results from these previously performed investigations and are compared to the values which are derived in the following.

Within this work the SPS BLM detector and finally also the LHC BLM detector response functions were simulated with the particle tracking code Geant4. This includes for a set of nine particle types (p, n, e^- , e^+ , γ , μ^+ , μ^- , π^+ , π^-) at energies in the range of keV to TeV their individual detector response. The simulation details and the verification measurements performed are described in chapter 5. A systematic error of 17% for the response functions in the utilised operation range of the detector was derived. Measurements and simulations for the HERA proton beam dump experiment were performed to estimate the uncertainties of hadronic shower measurements compared to Monte Carlo simulations. The measurements were performed with the LHC BLM system. A systematic error of 47% between the simulations and the measurements was estimated. In chapter 6 the comparison between different simulation codes and the measurements are discussed and a simplified method, referred to as Folding-Method, is presented which is utilised to perform the following estimation of LHC BLM detector thresholds.

To estimate an LHC BLM detector threshold several information from different sources are needed. The loss locations of the protons are determined by tracking studies of the circulating beam particles up to the position at which the particles hit an aperture limit. For this estimation of a detector threshold a localised proton impact at the beginning of a long straight section magnet (MQY) is assumed. Another important quantity is the quench limit of the mag-

net. The quench limits are derived from calculations of the heat transfer in the magnet. These information are input to the following estimation of the LHC BLM detector thresholds.

The energy deposition and the BLM detector signal are obtained by hadronic shower simulations initiated at the determined loss location. The number of lost beam protons which deposit as much energy in the coil as the predicted quench limit, is calculated from the quench limit and the maximum energy deposition in a cell of the coil. The magnet simulation provides in addition to the energy deposition the particle fluence spectrum outside of the magnet. This particle fluence spectrum is recorded in a strip along the magnet. The detector response is obtained by the convolution of the pre-simulated detector response functions with the part of the particle fluence spectra at the actual detector location. The signal corresponding to the LHC BLM detector threshold is derived by multiplying the obtained detector response with the calculated number of lost protons.

This estimates of the LHC BLM detector thresholds are finally compared to previously calculated thresholds.

7.1 Long Straight Section Magnet Simulation

Members of the LHC BLM team have been simulating parts of LHC components to calculate the thresholds for all the 4000 monitors installed around the ring [53]. A simulation of an MQY LHC magnet in Geant4 is reused to estimate a detector threshold. An MQY magnet has a larger diameter compared to a dipole magnet and is more similar to the HERA dump in terms of nuclear interaction lengths (see Table 6.1). The physical properties (dimensions and corresponding density) of the whole magnet and the 3.4 m long superconducting coil are entered into the simulation. The simulation records the deposited energy in the coil and the particle spectrum outside the magnet. The coil is split into a grid of cells. In the longitudinal direction the coil is split into 300 ($\Delta z = 1.13$ cm) steps, in radial direction into 20 steps ($\Delta r = 0.187$ cm) and the polar angle into 60 steps ($\Delta\varphi = 6^\circ$). Into each of these cells the accumulated energy deposition per volume is recorded. The volumes range from $7.98 \cdot 10^{-2}$ cm³ to $1.59 \cdot 10^{-1}$ cm³.

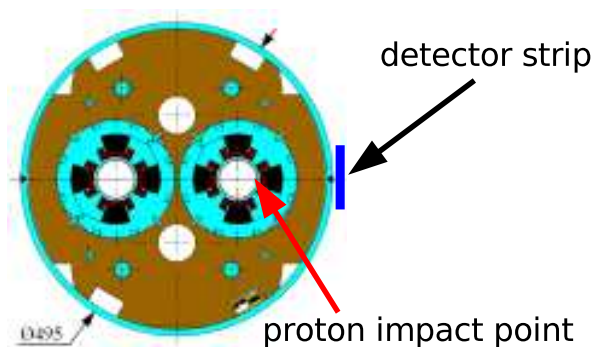


Figure 7.1: Cross section of an MQY magnet. Indicated are the proton impact position and the detector placement [46].

The particle fluence spectrum is recorded with a detector in the form of a 340 cm long and 10 cm wide strip. The strip is placed outside of the magnet's cryostat and centred in the horizontal position with respect to the plane of the beam pipe which is the standard mounting position for an LHC BLM detector (see chapter 2). The layout of the simulation is shown in Figure 7.1. All necessary particle properties are recorded (type, position, momentum and energy). In total 786

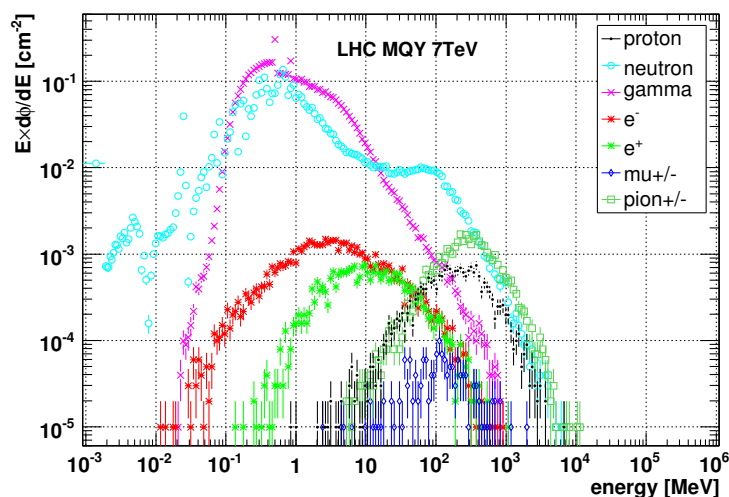


Figure 7.2: Secondary particle fluence spectrum outside of an MQY LHC quadrupole magnet recorded in a 3.4 m long strip (lethargy representation). QGSP-BERT-HP, 7 TeV.

protons at 7 TeV were initialised in the Geant4 simulation. The primary proton beam impacts at the inside of the beam pipe on the beam screen at an angle of 0.24 mrad. The impact point is in the horizontal plane with respect to the middle of the beam pipe onto the beam screen, which is shown in Figure 7.1. In the longitudinal direction the protons impact at 1.7 m from the magnets centre.

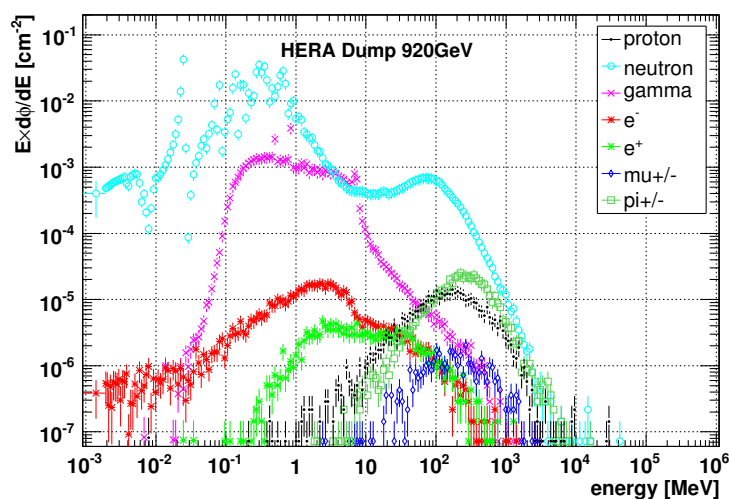


Figure 7.3: Secondary particle fluence spectrum on top of the HERA proton dump recorded in a 3.4 m long strip (lethargy representation). QGSP-BERT-HP, 920 GeV.

In Figure 7.2 the simulated particle fluence spectrum outside of an MQY magnet is plotted. In Figure 7.3 the particle fluence spectra on top of the HERA proton dump is shown. The spectra are normalised to the beam intensity and shown in lethargy representation. The HERA dump particle fluence spectrum is recorded in a 6.5 m long and 12 cm wide detector. In Figure 7.3 only the part of the spectrum from the first 3.4 m relative to the impact point of the protons on the dump is shown. The MQY particle fluence spectrum is dominated by gammas in the energy range of 100 keV to 20 MeV. The neutrons dominate the spectrum between 20 MeV to 300 MeV. Above

300 MeV up to a maximum particle energy of 5 GeV pions dominate. In the HERA dump particle fluence spectrum the neutrons dominate throughout the energy range from keV to 10 GeV. The comparison of the MQY particle fluence spectrum to the HERA beam dump particle fluence spectrum shows differences in the spectrum's particle composition. Calculating the ratio between the two spectra for the peak of the particle distribution shows for protons a factor of 60, for neutrons 4, for gammas 130, for electrons 65, for positrons 150, for muons 30 and for pions 65. These large ratios highlight the shorter distance the particles travel through the material in the MQY magnet and the higher primary energy of 7 TeV compared to the 920 GeV utilised in the HERA dump simulation.

The results from these simulations are utilised to perform an estimation of an LHC BLM threshold. By the convolution of the simulated particle fluence spectrum from the outside of the MQY magnet with the pre-simulated detector response functions the detector signal is derived. A detailed description of the detector signal simulation and the generation of the detector response functions is presented in chapter 5. A description of the black-hole-method, the Folding-Method and a cross check of these methods to derive the detector signal, can be found in chapter 6.

7.2 Detector Response Generation

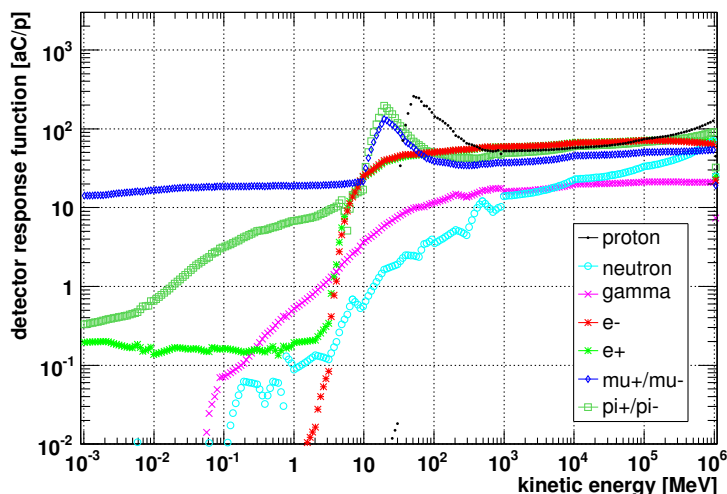


Figure 7.4: LHC BLM detector response functions for different particle types simulated with Geant4, QGSP-BERT-HP physics list. Impact angle of the particles relative to the detector axis is 60° .

To derive the detector signal a part of the spectrum is convoluted with the simulated response functions (see chapter 5). A typical LHC BLM detector mounting position is between $z=0$ and $z=3$ m after the proton impact position outside the cryostat. To illustrate the procedure of generating a BLM detector threshold a beam loss monitor is placed $z=1.5$ m after the impacting point of the lost protons on the outside of the MQY magnet. This position corresponds to detector 2 in the HERA beam dump experiment (see chapter 6). For the HERA proton beam dump simulation a significant mean angle of 65° of the escaping shower particles was obtained (see section 6.4.4). A similar escape angle of the particles leaving the MQY magnet is assumed. Therefore, the available pre-simulated detector response function of 60° is utilised for the Folding-Method. These response functions are shown in Figure 7.4 which were simulated with Geant4, QGSP-BERT-HP for the LHC BLM detector. The LHC BLM detector is about 49 cm long and

has a diameter of 9 cm which has a projected length of about 54 cm considering 60° crossing angle. The section of the secondary particle spectrum arriving at the distance of $z=1.5$ m to $z=2.04$ m relative to the impact point of the protons was considered in the Folding-Method.

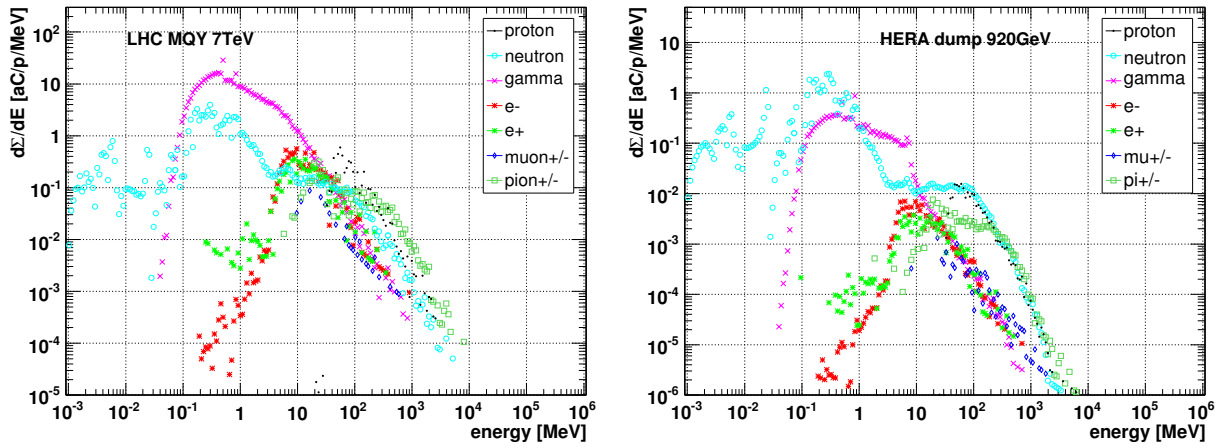


Figure 7.5: Detector signal (Σ) generated by convolving the particle fluence spectra with detector response functions. The detector is placed $z=1.5$ m after the proton impacting point. Left: MQY magnet, 7 TeV. Right: HERA dump, 920 GeV.

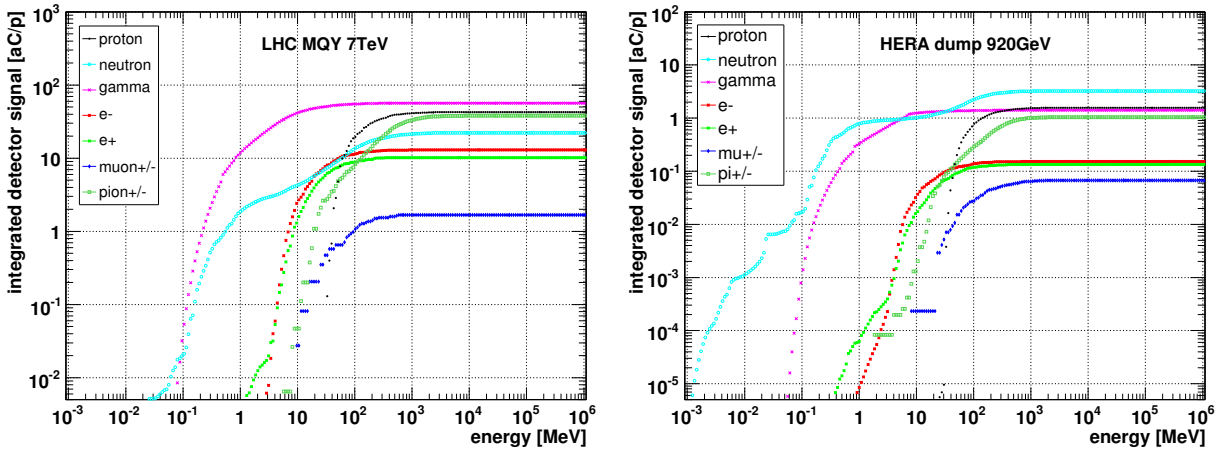


Figure 7.6: Detector signal integrated over particle energy for a detector placed $z=1.5$ m from the impacting point of the protons. Left: MQY magnet (7 TeV). Right: HERA dump (920 GeV). QGSP-BERT-HP physics list is utilised for both simulations.

The generated detector signal Σ per MeV is shown in Figure 7.5. The left plot shows the results for the MQY quadrupole magnet and the right plot refers to the HERA proton dump. The signal for the LHC magnet is dominated by gammas up to 20 MeV, at higher energies pions and protons contribute most. The signal for the HERA dump is dominated by neutrons. The final detector signal is calculated by integrating over all energy bins and particle types.

To illustrate the importance of the different particle types for the detector signal, the integral representation of the detector signal for each particle type is plotted in Figure 7.6. The Σ per MeV from Figure 7.5 is integrated over energy and shown per energy. The left plot refers to the signal of a detector outside of an MQY magnet and the right one to detector 2 at the HERA dump experiment. The integrated numbers in the last bin represent the signal contribution of

Table 7.1: Contribution from the different particle types to the signal. Compared are the signals for a LHC MQY BLM detector and detector 2 at the HERA dump experiment.

	LHC MQY	HERA dump
e+/-	12.6%	3.8%
gamma	30.7%	18.5%
mu+/-	0.9%	0.9%
neutron	12.1%	42.6%
pi+/-	20.6%	13.6%
proton	23.1%	20.6%
total signal [aC/p]	184.14	7.61

the respective particle type. It is shown that in the two cases different particle types dominate the signal level. The detector signal at the MQY magnet is determined to comprise of 31% from gammas, 21% from pions and 23% from protons. At the HERA dump the main contribution is from neutrons with 43% followed by gammas with almost 20%. The exact numbers are given in Table 7.1. The final detector signal per primary proton is calculated and amounts to 184.14 aC/p for the detector at the MQY quadrupole and 7.61 aC/p for detector 2 at the HERA dump. The systematic errors on these results are 17%, which was derived for the detector response functions and 18% due to the utilised Folding-Method. Therefore, a total error of 25% has to be taken into account on the relative detector responses. The ratio of 24 between the two signals is partially due to the 7.6 times higher energy of the primary protons for the magnet simulation and half the thickness in relative nuclear interaction length comparing the magnet to the dump, shown in Table 6.1.

7.3 Quench Limits

Particles lost from the beam generate particle showers in the magnet. These particles deposit energy also in the superconducting coil of the magnet. The limit of the energy deposition at which the superconducting coil undergoes a transition from the superconducting to the normal conducting state is referred to as quench limit. In the LHC magnets the cables of the superconducting coil are made from NbTi embedded in a copper matrix. In Figure 7.7 the phase diagram of NbTi is shown. The indicated surface is referred to as critical surface. NbTi is superconducting if its state is below the critical surface. The state depends on the absolute temperature T [K], the effective magnetic flux density B [T] and the current density J [kA m⁻³]. Without current in the coil the NbTi cables will quench at 9.2 K.

The temperature rise in the superconducting coil of a magnet is not only dependent on the energy of the lost beam particles but also on the loss duration. In Figure 7.8 the quench limits of an LHC dipole magnet are shown at injection energy and at high energy [9]. Indicated are the heat transfer mechanisms for different loss durations. For transient or instantaneous losses the deposited energy is not dissipated. Only the heat capacity of the cable is relevant for these fast losses. Transient losses are loss durations shorter than 100 μ s. For loss durations in the order of milliseconds the heat flow in the cable and through the helium has to be taken into account. For steady state losses, in the order of seconds, the quench limit is determined by the continuous heat flow into the cryogenic system. Considering all these scenarios the calculation of the quench

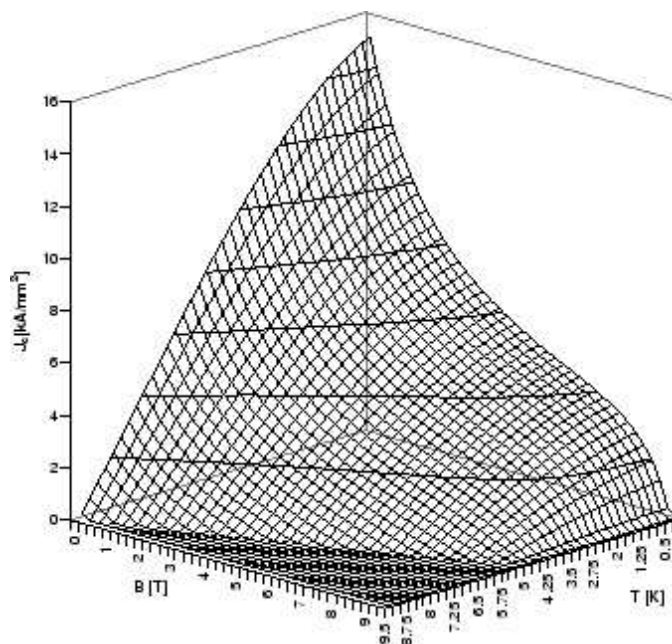


Figure 7.7: The critical surface for the NbTi superconductor [54].

limits leads to the shown values in Figure 7.8.

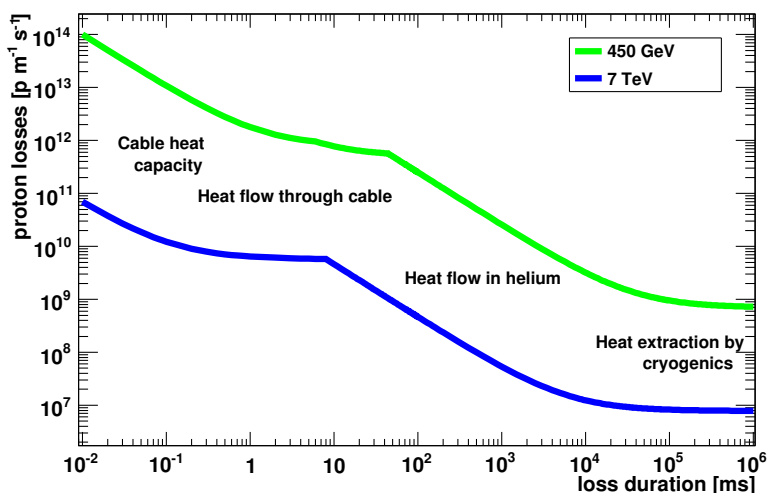


Figure 7.8: Quench limits for the LHC dipole magnets as function of loss duration. Indicated are the different heat distribution mechanisms [9].

There are several types of LHC magnets. For each type the quench limits are calculated depending on the geometry and operation parameters. An LHC MQY quadrupole magnet has for transient losses a quench limit of 5.0 mJ/cm^3 [55][9]. For steady state losses a quench limit of 5.29 mW/cm^3 for the same MQY magnet is obtained [56][57] (see Table 7.3). These quench limits are valid, for a beam energy of 7 TeV which determines the current and respectively the magnetic field strength in the magnet for a temperature of 4.5 Kelvin of the superconducting coil. The MQY magnets are located in Long Straight Sections (LSS) of the LHC. For comparison, arc magnets of the LHC are cooled down to 1.9 K.

7.4 Calculation of the Detector Threshold

For a certain number of lost protons the energy deposition in the coil of the magnet will reach the limit at which a quench occurs. This number can be calculated from energy deposition simulations in the coil and the corresponding quench limit. Utilising this number of protons the previously derived detector response is scaled to generate the detector signal. A detector signal derived for the limit of the energy deposition in the coil is referred here to as quench level. The following estimation of a BLM detector signal is performed for a loss duration of $40 \mu\text{s}$ with the corresponding quench limit of $5.0 \text{ mJ}/\text{cm}^3$ and for a loss duration of 100 s with a corresponding quench limit of $5.29 \text{ mW}/\text{cm}^3$. The shortest period of time the LHC BLM system analyses data is $40 \mu\text{s}$, therefore the choice.

The simulated energy deposition in the MQY magnet and in the HERA dump is normalised to the corresponding cell volume and to the number of primary protons. A maximum energy deposition density of $3.34 \cdot 10^{-10} \text{ J}/(\text{cm}^3 \cdot \text{proton})$ is derived for the MQY magnet. For comparison, at the HERA proton dump a maximum energy deposition density of $3.5 \cdot 10^{-11} \text{ J}/(\text{cm}^3 \cdot \text{proton})$ with the QGSP-BERT-HP physics list was calculated.

Table 7.2: Material properties for carbon and iron [7].

material	radiation length	nuclear interaction length
carbon	18.85 cm	38.1 cm
iron	1.76 cm	16.76 cm

The lower maximum energy deposition density in the HERA proton dump is determined by the different materials utilised in the dump and in the magnet. The core of the beam dump is made from carbon, the magnet is for the purpose of this estimation, within this paragraph assumed to be made from iron. Carbon has 10.7 times larger radiation length and 2.3 times larger nuclear interaction length compared to iron (Table 7.2). Therefore, the depth of the maximum energy deposited in one cell per primary proton is different. In the HERA dump the maximum is at a depth of 160 cm (920 GeV) and in the MQY magnet the maximum energy deposition is at a depth of about 30 cm (7 TeV). In the dump the energy is distributed over a larger volume, which is shown in the lower maximum energy deposition per cell volume.

The number of lost beam protons, which deposit sufficient energy in the coil to achieve the quench limit is calculated as follows.

One divides the corresponding quench limit by the simulated maximum energy deposition density in the coil. For the loss duration of $40 \mu\text{s}$ the number of protons calculated is $1.50 \cdot 10^7$ per $40 \mu\text{s}$, determined by the quench limit of $5.0 \text{ mJ}/\text{cm}^3$ divided by $3.34 \cdot 10^{-10} \text{ J}/(\text{cm}^3 \cdot \text{proton})$. The number of protons calculated for a loss duration of 100 s , amounts to $1.58 \cdot 10^9$ per 100 s , at the corresponding quench limit of $5.29 \text{ mW}/\text{cm}^3$.

In the previous section the normalised detector signal per primary proton for a detector placed at a chosen position of 1.5 m from the impact point of the protons (7 TeV) on an MQY magnet was derived to be 184.14 aC/p. By multiplying this detector response with the number of derived protons the LHC BLM thresholds are calculated. For transient losses the detector signal is estimated to be $6.89 \cdot 10^{-5} \text{ A}$. For steady state losses the detector signal is estimated to be $2.92 \cdot 10^{-9} \text{ A}$. The results are plotted in Table 7.3 and are shown in Figure 7.8.

Table 7.3: Loss duration dependent quench limits for the MQY magnet [58]. Previously calculated minimum and maximum BLM signals [59][60] for LHC arc magnets in comparison to the estimated BLM detector signal derived within this work.

loss duration	quench limit	detector current [A]			
		min	max	this work	error
$<100 \mu\text{s}$	$5 \text{ mJ}/\text{cm}^3$	$3.05\text{e-}07$	$1.83\text{e-}05$	$6.89\text{e-}05$	$3.65\text{e-}05$
$100 \text{ s}<$	$5.29 \text{ mW}/\text{cm}^3$	$4.17\text{e-}10$	$2.50\text{e-}08$	$2.92\text{e-}09$	$1.55\text{e-}09$

A comparison of the derived results for steady state losses to previously calculated detector signals [59][60] for LHC arc magnets was performed. It was shown that the estimated signal is within the minimum and maximum of the previously calculated signal levels which can be seen in Figure 7.8. The minimum and the maximum detector current, utilised in the comparison, are derived from the investigation mentioned in the introduction to this chapter. Thereby, the number of secondary particles derived outside of the magnet was scaled with $1.01 \cdot 10^{-15}$ to obtain the shown detector current. The result for transient losses exceeds the previously calculated maximum signal level for LHC arc magnet BLM detectors by a factor of 3.8. This shows that the different groups of magnets with their corresponding detectors need appropriate considerations. The estimated signal levels are well within the specifications of the LHC BLM electronics which has an acquisition range of 2.5 pA to 1 mA.

Systematic uncertainties of these results are derived from the detector response simulations to 17%, from the Folding-Method to 18%, which includes also the statistical errors and from the comparison of hadronic shower simulations to measurements to 47%. These uncertainties result in a total uncertainty of 53%, which is applied to the estimated results (this work) in Table 7.3 and in Figure 7.8.

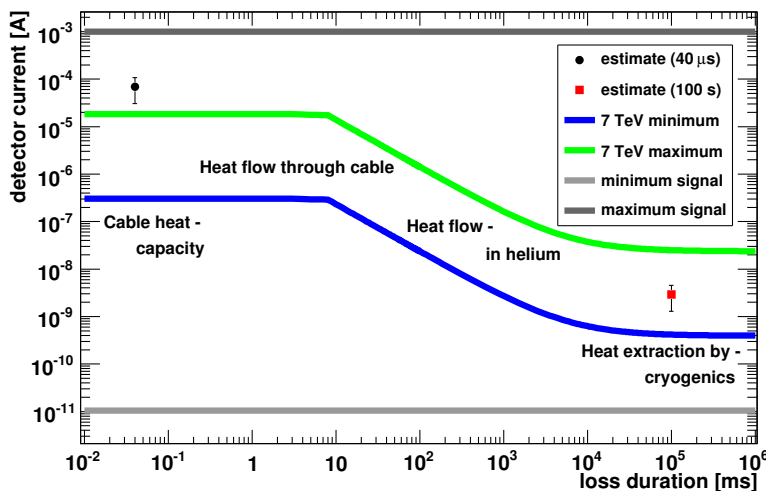


Figure 7.9: LHC BLM detector signals as function of loss duration for LHC arc dipole magnets [16] which are compared to the estimated detector signals derived within this work for an MQY LSS quadrupole magnet.

In the case of a transient loss the LHC BLM system has to send a dump request if the detector signal exceeds in the $40 \mu\text{s}$ acquisition time window, a specified fraction (in the order of 30% to

70%) of $68.9 \mu\text{A}$ which corresponds to about 13 CFC counts. In case of the steady state beam loss the LHC BLM system will trigger a beam dump if the detector signal exceeds a specified fraction of 2.92 nA (about 1450 CFC counts) for the 100 s acquisition time window [12].

7.5 Summary

In this chapter, LHC BLM detector thresholds for steady state and transient losses were estimated by utilising several information from different sources which are the quench limits and the hadronic shower simulation for the utilised LHC long straight section quadrupole magnet. The particles fluence spectrum outside the magnet was convoluted in the Folding-Method with the detector response functions to derive the detector signals. A comparison to previously calculated detector thresholds was performed. The derived estimate of a detector signal for steady state losses on an MQY magnet is within the existing calculated detector signals for LHC reference arc magnets. The estimated detector signal for transient losses exceeds the existing calculated signal by a factor of 3.8, but it is still within the design parameters of the LHC BLM electronics.

Chapter 8

Conclusions

The initial requested systematic error of the LHC BLM system should be smaller than 5 for the whole acquisition chain. To achieve this initial accuracy different simulations have been carried out. These simulations include the detector response function simulations and the hadronic shower simulations.

During this work the LHC BLM detector has been designed and built. Therefore, the investigations performed and described within this work were conducted with the existing SPS BLM detector, which is similar in design when compared to the LHC BLM detector. No fundamental differences between the behaviour of the two detectors are expected.

To simulate the detector signal, the LHC BLM detector and the SPS BLM detector geometry were modelled in Geant4. For the purpose of this simulation all main detector parts, except the small components (e.g. screws) had to be modelled.

The statistical and systematic uncertainties in the simulated signal generation were investigated by geometry, range cut-off value, impact angle variations and different physics lists have been utilised.

- Previously, only the energy deposited in the volume between the electrodes was considered to contribute to the signal. By simulating the electric field in the detector a larger sensitive volume is obtained. The 4% increase in sensitive volume, from this new approach, increased the accuracy of the simulated signal compared to that from geometric modelling.
- The standard Geant4 range cut-off value is 1 mm. However, this value is larger than the thickness of the electrodes, preventing the production of particles in it that can deposit energy within the gas. By reducing the cut-off value to 0.01 mm an increase in the detector signal of 13% has been found. This new production cut-off value is a appropriate compromise between required simulation time and accuracy and gave results with a systematic uncertainty of only 3.3%.
- An investigation into the effect of impact angle of the particles showed a maximum variation of 40% in the detector response for protons.
- Geant4 provides several physics lists; a comparison of the energy deposition produced with LHEP and QGSP physics lists showed at low proton energies no differences. At a higher energy of 1 TeV a difference of 40% has been observed.

Utilising the results from the detector signal investigations the detector response functions were simulated with the QGSP-BERT-HP physics list of Geant4. The SPS BLM detector response functions for different particle types at various kinetic energies in the range of 10 keV to 1 TeV have been generated for transverse and longitudinal impact of the particles.

Validation calculations of the energy cut-off for protons, electrons and gammas agreed with the simulation. The energy deposition for 1 MeV muons derived with Bethe-Bloch agreed within 5% to the simulated detector signal.

The LHC BLM detector and the SPS BLM detector were calibrated and the detector response functions validated for several irradiation scenarios, particle types and at various energies at four different irradiation facilities. An overview of the calibration measurements described in this thesis is shown in table 8.1.

- Proton measurements at 400 GeV from the SPS T2 extraction line were compared to the simulation. The unknown beam position relative to the inner structure (parallel electrodes), led to a systematic uncertainty of the simulation of 11%. The measurements and the simulations agree within 13%.
- Gamma ray measurements with Cs137 at 662 keV from the SC-RP Calibration Laboratory for Radiation Protection Instruments (CERN) were compared to the simulation. The detector showed a linear behaviour over two orders of magnitude in the dose rate ($30 \mu\text{Sv/h}$ to 3mSv/h). The relative difference between the detector response simulation and the measurement was 14% with an uncertainty of 12%. This deviation stems mainly from the uncertainties arising from the simplified geometry in the simulation and from the dose to fluence conversion factors utilised.
- Neutron measurements at the peak neutron energy of 174 MeV have been performed at the Svedberg Laboratory, Uppsala University (Sweden). The contribution of photons to the measured signal was estimated to be 15%. The relative differences between the simulations and the corrected measurements were $13\% \pm 11.4\%$ and $37\% \pm 13.9\%$ for longitudinal and transverse impact, respectively.
- Mixed Radiation Field Measurements at the CERF (CERN-EU High Energy Reference Field Facility) have been performed. A copper target has been placed in a secondary beam of 120 GeV/c hadrons. Five ionisation chambers have been positioned around the copper target so that they have been exposed to different radiation fields varying in particle composition and energy. FLUKA simulated spectra have been utilised as the input to simulate the detector response with Geant4. A comparison of the Geant4 simulation to the BLM detector measurement has shown a relative difference of 12%, except at detector position 1. There, a difference of 21% has been observed. The detector specific energy cut-off and the shift of the particle spectrum utilised in the simulation to lower energies, (below 1 GeV) statistically lead to a lower number of particles that contribute to the detector signal. The detectors showed a linear behaviour throughout one order of magnitude of beam intensity. These results provide evidence that the detector response for a given particle fluence spectrum can be simulated with Geant4 to within 20% accuracy. Additionally it can be concluded that the simulations work properly for the different particle types of the mixed radiation fields.

The results from the 3 direct irradiation experiments of the detector; the proton experiment, the gamma-ray experiment and the neutron experiment are all within approximately 15% of the

Table 8.1: Comparison of measured and simulated BLM detector response at various irradiation facilities. Relative differences are calculated as (simulation-measurement)/measurement.

		rel. diff. [%]	error [%]
proton experiment		13.1	11.4
gamma experiment		-14.3	12.1
neutron experiment	long.	-12.6	11.4
	trans.	-37.4	13.9
CERF experiment	detector		
	1	-21.0	14.1
	2	—	—
	3	5.0	10.9
	4	12.5	11.4
	5	11.7	10.8
	6	-8.4	15.5

simulation results. The mixed radiation field measurements and simulations for the first detector agree within 20%, for the other detectors the agreement was better than 12%.

To estimate the uncertainties of hadronic shower simulations, tests have been carried out at DESY's HERA proton beam dump. Measurements in the tails of hadronic showers have been performed and compared to the simulations. A systematic error of 10% from the HERA bunch-filling pattern has been identified in these measurements.

These parasitic measurements have been performed nearly continuously over a two-year period with the LHC BLM electronics. This led to improvements of the equipment and to software upgrades during this long-term system test.

The ionisation detector measurements on the dump showed a non-linear response versus the beam intensity. A simplified space-charge-effect correction derived from previously published formulae has been applied to the measurements, which considerably improved the linearity of the response. It was found that the charge collection efficiency of the detectors is only about 20% at the highest energy deposition of about 0.5 Gy which after space-charge-effect correction is approximately 2.5 Gy.

At low beam intensities the corrected measurements from these tests remain non-linear and show different behaviour between each of the detectors. This provides evidence that at low intensities additional effects were influencing the measurements, which are in the order of 40%. The origin of these effects could not be determined. Further investigations into these effects are currently being performed.

The spectra obtained from the simulations in the mixed field experiment for detector position 2, 3 and 4 are similar to the spectra obtained outside of an LHC quadrupole magnet. The largest total uncertainty of 17% has been found at detector 4. This uncertainty is utilised as a systematic uncertainty on the final detector response functions up to the operational limit at which space

charge effects start to apply. This has been demonstrated at the HERA dump experiment where for space charge effect was corrected. The limit corresponds to a calculated ionisation rate of $4.16 \cdot 10^7$ [ions/cm³μs]. The operational range of the LHC BLM detector is a factor 2.5 below the ionisation rate at which space charge effects start to apply.

The detector signals have been simulated with Geant4 and simulation data from FLUKA has been provided for comparison.

Three similar methods have been utilised to derive the detector signal and provided a consistent check. These validations show good agreement, providing verification of the simplified Folding-Method which is utilised for the LHC BLM detector threshold generation.

To identify differences between the simulations obtained with the various Monte Carlo codes the particle spectra derived for the different detector locations were compared. QGSP-BERT-HP and FLUKA showed similar spectra. FTFP showed fewer neutrons at lower particle energies which is probably due to the missing -HP model extension.

To estimate the uncertainties for the dump experiment a comparison of the simulation results against the measurements has been performed. The simulated detector signals from QGSP-BERT-HP and FLUKA were similar and describe the measurements more precisely than FTFP. The best agreement has been found for detector 2 which is close to the shower maximum. Here, the detector signal simulated with QGSP-BERT-HP and FLUKA is approximately 50% lower than the measurements. Therefore, the QGSP-BERT-HP physics list of Geant4 or FLUKA are proposed for the LHC BLM threshold simulations. The Geant4 development team also considers that QGSP-BERT-HP is the most reliable physics list for this type of application.

The specification for the initial accuracy of the entire LHC BLM acquisition chain is that it should be within a factor of 5. Contributions to these uncertainties are the simulation of the hadronic shower and the detector signal generation. To give an error estimation for the LHC BLM system a detector, placed outside of an LHC magnet cryostat between $z=0.5$ m and $z=3.5$ m after the impact point of the protons, was assumed. The projected particle path length between impact point and detector location at the LHC magnet is about $10 \lambda_0$ (nuclear interaction lengths). The copper rod in the mixed radiation field measurement is in projected particle path length about $3 \lambda_0$ and the dump in the HERA experiment is about $16 \lambda_0$. The results from the four validation measurements described earlier were all within approximately 20%. At the HERA beam dump experiment the first 4 detectors were within 70% when comparing the simulations and measurements. Scaling these uncertainties with the projected particle path length results in an estimated uncertainty of 47% for the simulated LHC BLM detector thresholds.

Finally, the Folding-Method has been utilised for the estimation of an LHC BLM detector threshold. The estimated detector signal for steady state losses on an MQY magnet is within existing calculated detector signals for LHC reference arc magnets. For transient losses the estimated detector signal exceeds the existing calculated signal by a factor of 3.8, but it is still within the design parameters of the LHC BLM electronics.

Bibliography

- [1] DSU Communication Group. CERN's public website. <http://public.web.cern.ch/public/>, viewed August 2007.
- [2] O.S. Brüning, P. Collier, P. Lebrun, S. Myers, R. Ostojic, J. Poole, and P. Proudlock. *LHC Design Report, v.1: the LHC Main Ring*. Number CERN-2004-003-V-1. CERN, Geneva, 2004.
- [3] *ATLAS: Technical Proposal for a general-purpose pp experiment at the Large Hadron Collider at CERN*. Number CERN-LHCC-94-43 ; LHCC-P-2 in LHC Tech. Proposal. CERN, Geneva, 1994.
- [4] *CMS: Technical Proposal*. Number CERN-LHCC-94-38 ; LHCC-P-1 in LHC Tech. Proposal. CERN, Geneva, 1994. Cover title : CMS, the Compact Muon Solenoid: technical proposal.
- [5] *ALICE: Technical Proposal for a Large Ion collider Experiment at the CERN LHC*. Number CERN LHCC-95-71, LHCC-P-3 in LHC Tech. Proposal. CERN, Geneva, 1995.
- [6] *LHCb: Technical Proposal*. Number CERN LHCC-98-04, LHCC-P-4 in Tech. Proposal. CERN, Geneva, 1998.
- [7] W.-M. Yao et al. Review of Particle Physics. *Journal of Physics G*, 33:1+, 2006.
- [8] R Schmidt, R W Assmann, E Carlier, B Dehning, R Denz, B Goddard, E B Holzer, V Kain, B Puccio, B Todd, J Uythoven, J Wenninge, and M Zerlauth. Protection of the CERN large hadron collider. *New J. Phys.*, 8:290. 31 p, 2006.
- [9] J.B. Jeanneret, D. Leroy, L. Oberli, and T. Trenkler. Quench levels and transient beam losses in LHC magnets. Technical Report LHC Project Report 44, CERN, 1996.
- [10] F. Bordry, R. Denz, K-H. Mess, B. Puccio, F. Rodriguez-Mateos, and R. Schmidt. Machine protection for the LHC: Architecture of the beam and powering interlock systems. Technical Report LHC Project Report 521, CERN, 2001.
- [11] R. Schmidt, R.W. Assmann, H. Burkhardt, E. Carlier, B. Dehning, B. Goddard, J.B. Jeanneret, V. Kain, B. Puccio, and J. Wenninger. Beam loss scenarios and strategies for machine protection at the LHC. *AIP Conf. Proc.*, 693(LHC-Project-Report-665. CERN-LHC-Project-Report-665):184–187. 5 p, Aug 2003. revised version number 1 submitted on 2003-08-25 11:18:46.
- [12] E.B. Holzer, B. Dehning, E. Effinger, J. Emery, G. Ferioli, J.L. Gonzalez, E. Gschwendtner, G. Guaglio, M. Hodgson, D. Kramer, R. Leitner, L. Ponce, V. Prieto, M. Stockner, and C. Zamantzas. Beam loss monitoring system for the LHC. In *Nuclear Science Symposium Conference Record, 2005 IEEE*, volume 2, pages 1052–1056, 23-29 Oct. 2005.

- [13] W. Friesenbichler. Development of the readout electronics for the beam loss monitors of the LHC. Master's thesis, Fachhochschule Wr. Neustadt, 2002. CERN-THESIS-2002-028.
- [14] C. Zamantzas. *The Real-Time Data Analysis and Decision System for Particle Flux Detection in the LHC Accelerator at CERN*. PhD thesis, School of Engineering and Design Brunel University, 2006.
- [15] D. Kramer, B. Dehning, E.B. Holzer, G. Ferioli, and M. Stockner. Simulations and measurements of secondary electron emission beam loss monitors for LHC. *Nuclear Physics B (Proc. Suppl.)*, 172:246–249, 2007.
- [16] A. Arauzo and C. Bovet. Beam loss detection system in the arcs of the LHC. Technical Report CERN-SL-2000-052 BI, CERN - SL DIVISION, 2000.
- [17] C. Zamantzas, B. Dehning, E. Effinger, J. Emery, and G. Ferioli. An FPGA based implementation for real-time processing of the LHC beam loss monitoring system's data. In *IEEE NSS-MIC '06, San Diego, IEEE Trans. Nucl. Sci., submitted for publication*, 2006.
- [18] G.F. Knoll. *Radiation Detection and Measurement - Third Edition*. Number ISBN 0-471-07338-5. John Wiley & Sons, 2000.
- [19] International Commission on Radiation Units and Measurements. Average energy required to produce an ion pair. Technical report, ICRU Report 31, Washington D.C., 1979.
- [20] S. Agostinelli et al. Geant4—a simulation toolkit. *Nuclear Instruments and Methods in Physics Research Section A: Accelerators, Spectrometers, Detectors and Associated Equipment*, Volume 506, Issue 3:250–303, 1 July 2003.
- [21] J. Allison et al. Geant4 Developments and Applications. *IEEE Transactions on Nuclear Science*, Volume 53, Issue 1, Part 2:270– 278, 2006.
- [22] Geant4 world-wide collaboration. Geant4. <http://geant4.web.cern.ch/geant4/>, viewed July 2006.
- [23] Geant4 team. Physics Reference Manual. <http://geant4/support/userdocuments.shtml>, viewed 07/2007.
- [24] J. Apostolakis, G. Folger, V. Grichine, A. Howard, V. Ivanchenko, M. Kossov, and A. Ribbon. Hadronic shower shape studies in Geant4. Technical Report CERN-LCGAPP-2007-02, CERN, March 2007. version 1.1.
- [25] V. Grichine. Private communication (CERN).
- [26] R. Brun and F. Rademakers. ROOT - an object-oriented data analysis framework. <http://root.cern.ch/>, viewed March 2006.
- [27] L.D. Landau. On the energy loss of fast particles by ionisation. *J. Exp. Phys. (USSR)*, 8:201, 1944.
- [28] W.R. Leo. *Techniques for Nuclear and Particle Physics Experiments: A how to approach*. Berlin, Germany: Springer, 1987.
- [29] K. Halbach and R.F. Holsinger. SUPERFISH - a computer program for evaluation of RF cavities with cylindrical symmetry. *Particle Accelerators* 7, pages 213–222, 1976.
- [30] National institute of standard and technology (NIST). <http://physics.nist.gov/>, viewed August 2007.

- [31] M.J. Berger, J.S. Coursey, M.A. Zucker, and J. Chang. Stopping-power and range tables for electrons, protons, and helium ions. <http://physics.nist.gov/PhysRefData/Sar/Text/contents.html>, viewed March 2006.
- [32] M.J. Berger, J.H. Hubbell, S.M. Seltzer, J. Chang, J.S. Coursey, R. Sukumar, and D.S. Zucker. XCOM: photon cross sections database. <http://physics.nist.gov/PhysRefData/Xcom/Text/XCOM.html>, viewed March 2007.
- [33] M. Hodgson. Beam loss monitor design investigations for particle accelerators. Master's thesis, University of Surrey, England, 2005.
- [34] International Commission on Radiological Protection. Conversion coefficients for use in radiological protection against external radiation. *Annals of the ICRP*, 26(3-4):1–205, 1996.
- [35] A.V. Prokofiev, O. Bystrm, C. Ekstrm, V. Ziemann, J. Blomgren, S. Pomp, M. Oesterlund, and U. Tippawan. A new neutron beam facility at TSL. *International Workshop on Fast Neutron Detectors and Applications, University of Cape Town, South Africa*, (FNDA2006 016), 2006.
- [36] A.V. Prokofiev, A.N. Smirnova, and P-U. Renberg. A monitor of intermediate-energy neutrons based on thin film breakdown counters. Technical Report TSL/ISV-99-0203, The Svedberg Laboratory, 1999.
- [37] T. Wijnands, C. Pignard, and R. Tesarek. On-line radiation monitoring for the LHC machine and experimental caverns. Technical report, CERN, Oct 2006.
- [38] A.V. Prokofiev, M. Chadwick, S. Mashnik, N. Olsson, and L. Waters. Development and validation of the ${}^7\text{Li}(p,n){}^7\text{Be}$ nuclear data library and its application in monitoring of intermediate energy neutrons. *Journal of NUCLEAR SCIENCE and TECHNOLOGY*, supplement 2:112–115, 2002.
- [39] A.V. Prokofiev. Private communication (Svedberg Laboratory).
- [40] A. Mitaroff and M. Silari. The CERN-EU high-energy reference field (CERF) facility for dosimetry at commercial flight altitudes and in space. *Radiat. Prot. Dosim.*, 102(1):7–22, 2002.
- [41] A. Fassò, A. Ferrari, J. Ranft, and P.R. Sala. FLUKA: A multi-particle transport code. Technical report, CERN, SLAC, 2005.
- [42] A. Fassò, A. Ferrari, S. Roesler, P.R. Sala, G. Battistoni, F. Cerutti, E. Gadioli, M.V. Garzelli, F. Ballarini, A. Ottolenghi, A. Empl, and J. Ranft. The physics models of FLUKA status and recent developments. In *Computing in High Energy and Nuclear Physics 2003 Conference (CHEP2003)*, La Jolla, CA, USA, March 24-28 2003.
- [43] H. Vincke, N. Aguilar, D. Forkel-Wirth, M. Pangallo, D. Perin, M. Renou, and C. Theis. Measurements and simulations of the PMI chamber response to the radiation field inside the CERF target area. Technical Report CERN-SC-2004-025-RP-TN, CERN EDMS No.: 457013, 2004.
- [44] M. Schmitz. Die HERA-p Beam-Dump-Anlage. Technical Report DESY HERA 92-18, Deutsches Elektronen Synchrotron DESY, Hamburg, Germany, August 1992.
- [45] M. Schmitz. Aenderungen des HERA-p Beam-Dump-Systems ab 1996. Technical Report Add-on to DESY HERA 92-18, Deutsches Elektronen Synchrotron DESY, Hamburg, Germany, May 1996.

- [46] The LHC design, beam performance, and machine parameters & layouts. <http://lhc.web.cern.ch/lhc>, viewed July 2007.
- [47] B. Holzer. Private communication (DESY).
- [48] J. Dutton. A survey of electron swarm data. *Journal of Physical and Chemical Reference Data*, 4, Issue 3:577–856, 1975.
- [49] R.M. Zwaska. *Accelerator Systems and Instrumentation for the NuMI Neutrino Beam*. PhD thesis, University of Texas at Austin, December 2005.
- [50] R. Bruce. Private communication (CERN).
- [51] G. Folger and A. Howard. Private communication (CERN).
- [52] CERN batch services. <http://batch.web.cern.ch/batch/>, viewed August 2007.
- [53] M. Sapinski. Private communication (CERN).
- [54] F. Sonneman. The critical surface. <http://quench-analysis.web.cern.ch/>, viewed September 2007.
- [55] P. P. Granieri, M. Calvi, B. Baudouy, D. Bocian, L. Bottura, M. Breschi, A. Siemko, and P. Xydi. Stability analysis of the LHC cables for transient heat depositions. Technical report, CERN, to be published in 2007.
- [56] D. Bocian, B. Dehning, and A. Siemko. Modelling of quench limit for steady state heat deposits in LHC magnets. In *MT 20 - 20th International Conference on Magnet Technology*, number MT20-1K06, August 27 - 31, 2007.
- [57] D. Bocian and A. Siemko. A steady-state beam loss studies in the LHC superconducting magnets. Technical report, CERN, to be published in 2007.
- [58] D. Bocian, M. Calvi, and R. Siemko. Entalpy limit calculations for transient perturbations in LHC magnets. Technical Report AT-MTM-IN-2006-021, EDMS: 750204, CERN, AT-MTM and AB-BI, 2006.
- [59] A. Arauzo Garcia and Bovet C. Computer simulation of beam loss detection in the arcs of the LHC. Technical Report LHC Project Note 213, CERN, 2000.
- [60] E. Gschwendner, B. Dehning, G. Ferioli, W. Friesenbichler, and V. Kain. The beam loss detection system of the LHC ring. In *EPAC-02, Particle Accelerator Conference*, 2002.
- [61] Compendium of neutron spectra and detector responses for radiation protection purposes. Supplement to Technical Reports Series No. 318 Technical Reports Series No. 403, International Atomic Energy Agency, 2001.

Appendix A

Explanatory Notes

A.1 (Nuclear) Interaction Length

The collision length, which is also known as the nuclear collision length is the mean free path of a particle before undergoing a nuclear reaction. This mean free path is determined for a given particle in a given medium. The collision length is derived from the total nuclear cross-section σ_T by

$$\lambda_T = A/(\sigma_T N_A \rho) \quad (\text{A.1})$$

with $N_A = \text{Avogadro's number } (6.022 \cdot 10^{23}/\text{mole})$ $A = \text{atomic weight [g/mole]}$ and $\rho = \text{density [g/cm}^3\text{]}$.

The (nuclear) interaction length is the mean free path of a particle before undergoing an interaction that is neither elastic nor quasi-elastic (diffractive), in a given medium. Usually it is denoted by λ_I . It is obtained by the same formula A.1 as σ_T by utilising the relevant cross-section which is given by

$$\sigma_{inelastic} = \sigma_{total} - \sigma_{elastic} - \sigma_{quasielastic}$$

Some numerical values for λ_T and λ_I are quoted in Table A.1 and apply to the high energy range, where the energy dependence is weak [7].

Table A.1: Examples for (nuclear) collision length and (nuclear) interaction length of different materials [7].

Material	λ_T [cm]	λ_I [cm]	$\rho\lambda_T$ [g/cm ²]	$\rho\lambda_I$ [g/cm ²]	ρ [g/cm ³]
Fe	10.52	16.76	82.80	131.90	7.87
Al	26.15	39.41	70.60	106.40	2.70
Cu	9.55	15.06	85.60	134.90	8.96
Pb	10.24	17.09	116.20	194.00	11.35
Concrete	26.96	39.96	67.40	99.90	2.50

A.2 SPS Electronics - Charge Integrator

The so-called SPS electronics is a charge integrator with adjustable gain. Several measurement campaigns were performed with this electronics. In figure A.1 a schematic of the electronics is shown. Only the important parts are drawn to give a basic understanding.

The ionisation chamber (detector) is connected by filters to one of the operation amplifiers (OP_1 , OP_2 , ... OP_{16}), which are charge integrators. Available are up to 16 channels. With S_2 a capacitor is selected to collect the charge. This capacitor determines the first gain. The integration is triggered either by a timing signal or by pressing a key. By opening the switch S_1 the integration starts. After a certain time (triggered or constant) the charge collected in the capacitor is measured. A multiplexer (M_1) sweeps through the channels. With switch S_3 the second gain factor is chosen by selecting one of the resistors (R_1 to R_3) for measuring the voltage on the capacitors. Finally the voltage is measured by an ADC (analog digital converter) and recorded.

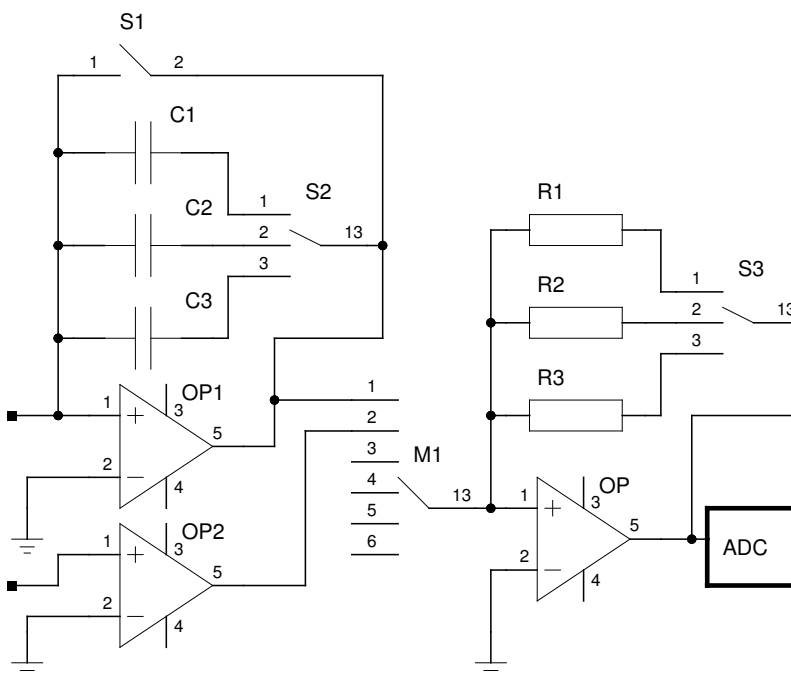


Figure A.1: Diagram of the SPS charge integrating electronics.

A.3 Dose Rate to Fluence Conversion

The conversion from ambient dose equivalent ($H^*(10)$) to fluence (ϕ) can be performed with an intermediate step to KERMA in air (K_a) and subsequently by a final conversion step to fluence. The unit of the ambient dose equivalent is joule per kilogram (J/kg) or sievert (Sv). The conversion as well as the needed conversion factors are in detail described and printed in the ICRP report 74 ([34]). A copy of the conversion factor tables can be found in Table A.2 and Table A.3. The coefficients are tabulated to a photon energy of 10 MeV.

Table A.1. Conversion coefficients^a for air kerma per unit fluence, K_a/Φ , of monoenergetic photons

Photon energy (MeV)	K_a/ϕ (pGy cm ²)
0.010	7.43
0.015	3.12
0.020	1.68
0.030	0.721
0.040	0.429
0.050	0.323
0.060	0.289
0.080	0.307
0.100	0.371
0.150	0.599
0.200	0.856
0.300	1.38
0.400	1.89
0.500	2.38
0.600	2.84
0.800	3.69
1.000	4.47
1.500	6.14
2.000	7.55
3.000	9.96
4.000	12.1
5.000	14.1
6.000	16.1
8.000	20.1
10.000	24.0

^aData from *ICRU Report 47* (ICRU, 1992a) using data from Hubbell (1982).

Figure A.2: Conversion coefficients from KERMA to fluence from ICRP report 74, table A.1 [34].

Table A.21. Conversion coefficients^a for the ambient dose equivalent, $H^*(10)$, and directional dose equivalent, $H'(0.07,0^\circ)$, from photon fluence and air kerma free-in-air

Photon energy (MeV)	$H^*(10)/K_a$ (Sv/Gy)	$H'(0.07,0^\circ)/K_a$ (Sv/Gy)	K_a/Φ (pGy cm ²)	$H^*(10)/\Phi$ (pSv cm ²)	$H'(0.07,0^\circ)/\Phi$ (pSv cm ²)
0.010	0.008	0.95	7.60	0.061	7.20
0.015	0.26	0.99	3.21	0.83	3.19
0.020	0.61	1.05	1.73	1.05	1.81
0.030	1.10	1.22	0.739	0.81	0.90
0.040	1.47	1.41	0.438	0.64	0.62
0.050	1.67	1.53	0.328	0.55	0.50
0.060	1.74	1.59	0.292	0.51	0.47
0.080	1.72	1.61	0.308	0.53	0.49
0.100	1.65	1.55	0.372	0.61	0.58
0.150	1.49	1.42	0.600	0.89	0.85
0.200	1.40	1.34	0.856	1.20	1.15
0.300	1.31	1.31	1.38	1.80	1.80
0.400	1.26	1.26	1.89	2.38	2.38
0.500	1.23	1.23	2.38	2.93	2.93
0.600	1.21	1.21	2.84	3.44	3.44
0.800	1.19	1.19	3.69	4.38	4.38
1	1.17	1.17	4.47	5.20	5.20
1.5	1.15	1.15	6.12	6.90	6.90
2	1.14	1.14	7.51	8.60	8.60
3	1.13	1.13	9.89	11.1	11.1
4	1.12	1.12	12.0	13.4	13.4
5	1.11	1.11	13.9	15.5	15.5
6	1.11	1.11	15.8	17.6	17.6
8	1.11	1.11	19.5	21.6	21.6
10	1.10	1.10	23.2	25.6	25.6

^aData compiled from *ICRU Report 47* (1992a) using Hubbell and Seltzer (1995). The K_a/Φ data are slightly different from those used for the protection quantities (see Table A.1) which used earlier data from Hubbell (1982).

Figure A.3: Conversion coefficients from $H^*(10)$ to K_a from ICRP report 74, table A.21 [34].

A.4 Binning of a Spectrum

Spectra are in most cases originally obtained as fluence in energy bins. The fluence in the i th energy bin is given by

$$\varphi_i = \int_{E_i}^{E_{i+1}} dE \Phi_E(E) \quad (\text{A.2})$$

where $\Phi_E(E) = d\phi/dE$ is in units of [$\text{cm}^{-2} \cdot \text{GeV}^{-1}$] (for linear and logarithmic binning).

For graphical presentation often the logarithm of the particle (neutron) energy is used as the abscissa. In this case the adequate way to show the spectra is fluence per lethargy [61]. A lethargy interval is defined for each bin as $\ln(E_{i+1}) - \ln(E_i)$, where E_i is the lower bin edge and E_{i+1} the upper bin edge, respectively. Substituting $\ln(E)$ for E in equation A.2, one obtains by using the mean value theorem,

$$\varphi_i = \int_{\ln E_i}^{\ln E_{i+1}} d \ln E E \Phi_E(E) = E'_i \Phi_{E'}(E') (\ln E'_{i+1} - \ln E'_i). \quad (\text{A.3})$$

In this case the ordinate is labelled with $E \times d\phi/dE$ which also can be expressed as $d\phi/d\ln(E)$. The associated unit to lethargy representation is [cm^{-2}]. The energy unit is not visible as it cancels out [$GeV \cdot GeV^{-1}$].

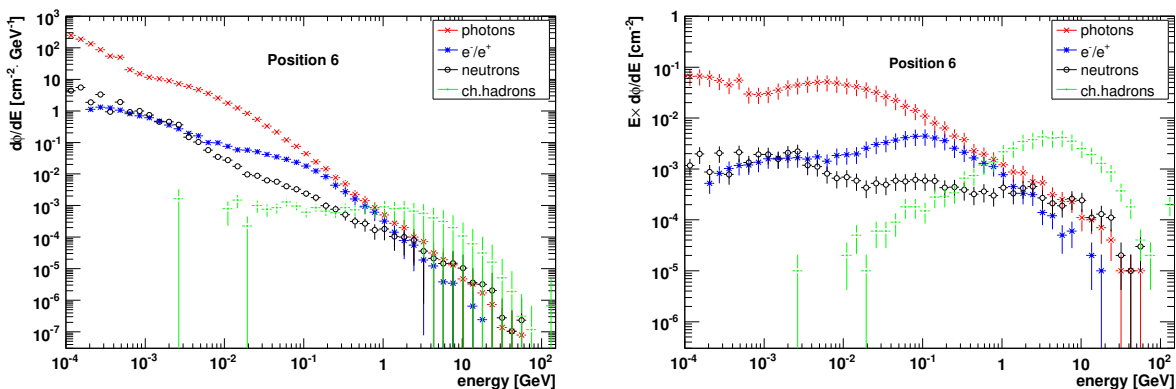


Figure A.4: Left: Arbitrary spectra with a logarithmic energy abscissa in group fluence [$cm^{-2} GeV^{-1}$]. Right: Arbitrary spectra with a logarithmic energy abscissa in group fluence per lethargy [cm^{-2}].

A.5 Numbers and Conversion Factors for the SPS BLM Detector

$$V_{SPS} = 1.2 \cdot 10^{-3} \text{ m}^3 \equiv 1.2 \text{ L (sensitive volume)}$$

$$\rho_{N_2} = 1.281 \text{ kg/m}^3 \text{ (for 1.1 bar, 20}^\circ\text{C)}$$

$$[\text{eV}] \longrightarrow [\text{J}] \quad 1.602 \cdot 10^{-19} \left[\frac{\text{J}}{\text{eV}} \right]$$

$$[\text{eV}] \longrightarrow [\text{Gy}] \quad \frac{1.602 \cdot 10^{-19}}{1.537 \cdot 10^{-3}} \left[\frac{\text{Gy}}{\text{eV}} \right]$$

$$[\text{eV}] \longrightarrow [\text{Gy}] \quad 104.229 \left[\frac{\text{aGy}}{\text{eV}} \right]$$

$$[\text{C}] \longrightarrow [\text{Gy}] \quad \frac{W_{N_2}}{m} \rightarrow \frac{34.8}{1.537 \cdot 10^{-3}} \left[\frac{\text{Gy}}{\text{C}} \right]$$

$$[\text{eV}] \longrightarrow [\text{aC}] \quad \frac{1.602}{348} \left[\frac{\text{aC}}{\text{eV}} \right]$$

A.6 Simulated HERA Dump Spectra

The main method in the HERA proton dump simulation is the black-hole-method. In a first part of the simulation spectra of particles escaping from the top of the dump are generated. Different physics lists of Geant4 and FLUKA were utilised to perform this simulations. At each detector

position the particles, which enter the detector are recorded. Plotted are the particles, which enter the bottom surface of the detector volume. A comparison of the particle fluence spectra derived with different models and Monte Carlo codes is shown in the figures A.5, A.6 and A.7 for 920 GeV primary protons and in figures A.8, A.9 and A.10. The spectra are plotted in fluence per lethargy [cm^2].

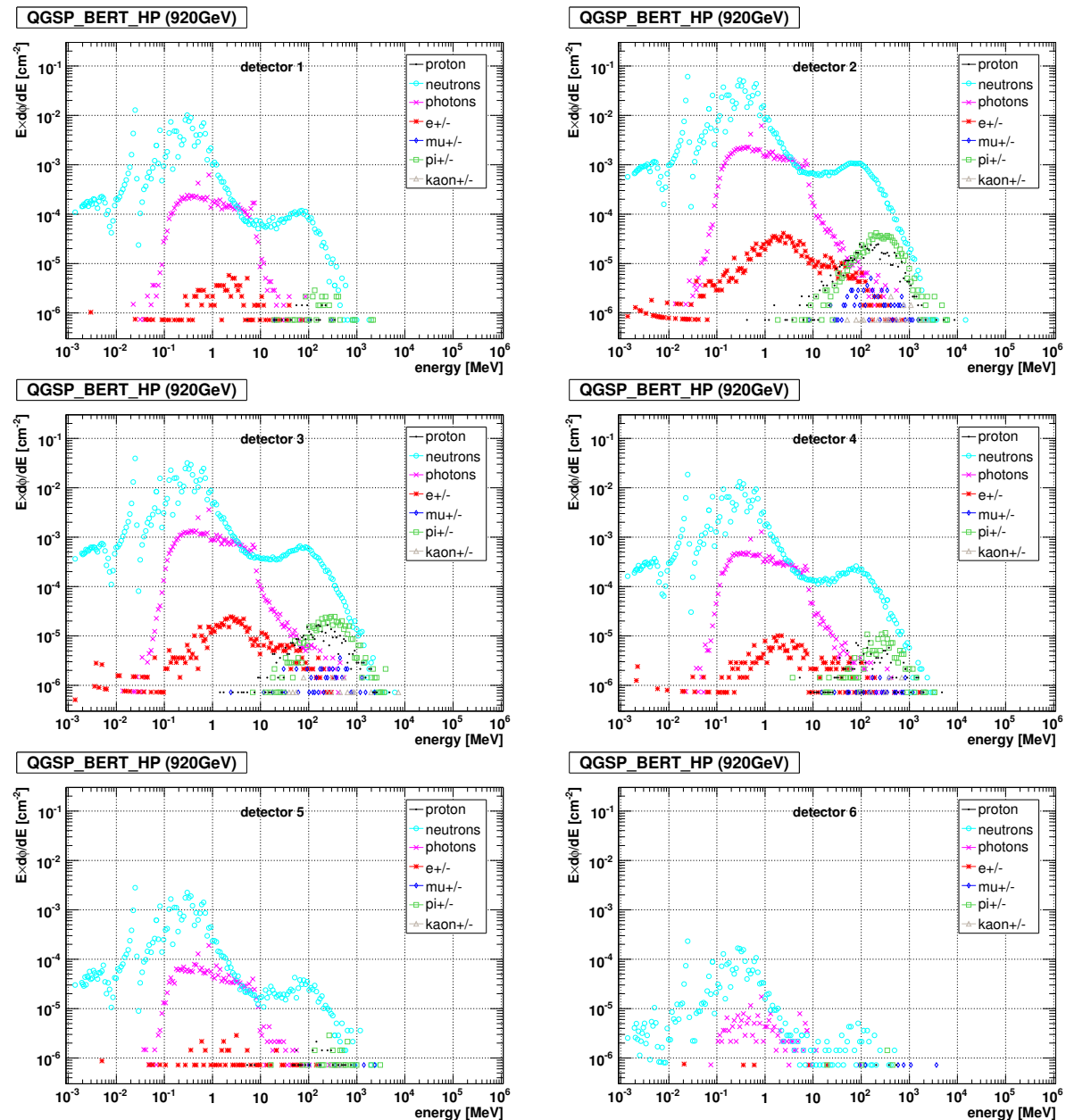


Figure A.5: Lethargy plot per cm^2 and per primary particle. The fluence spectra [particles/ cm^2 /primary/Lethargy] at different detector positions for 920 GeV proton energy was simulated with QGSP-BERT-HP physics list of Geant4.

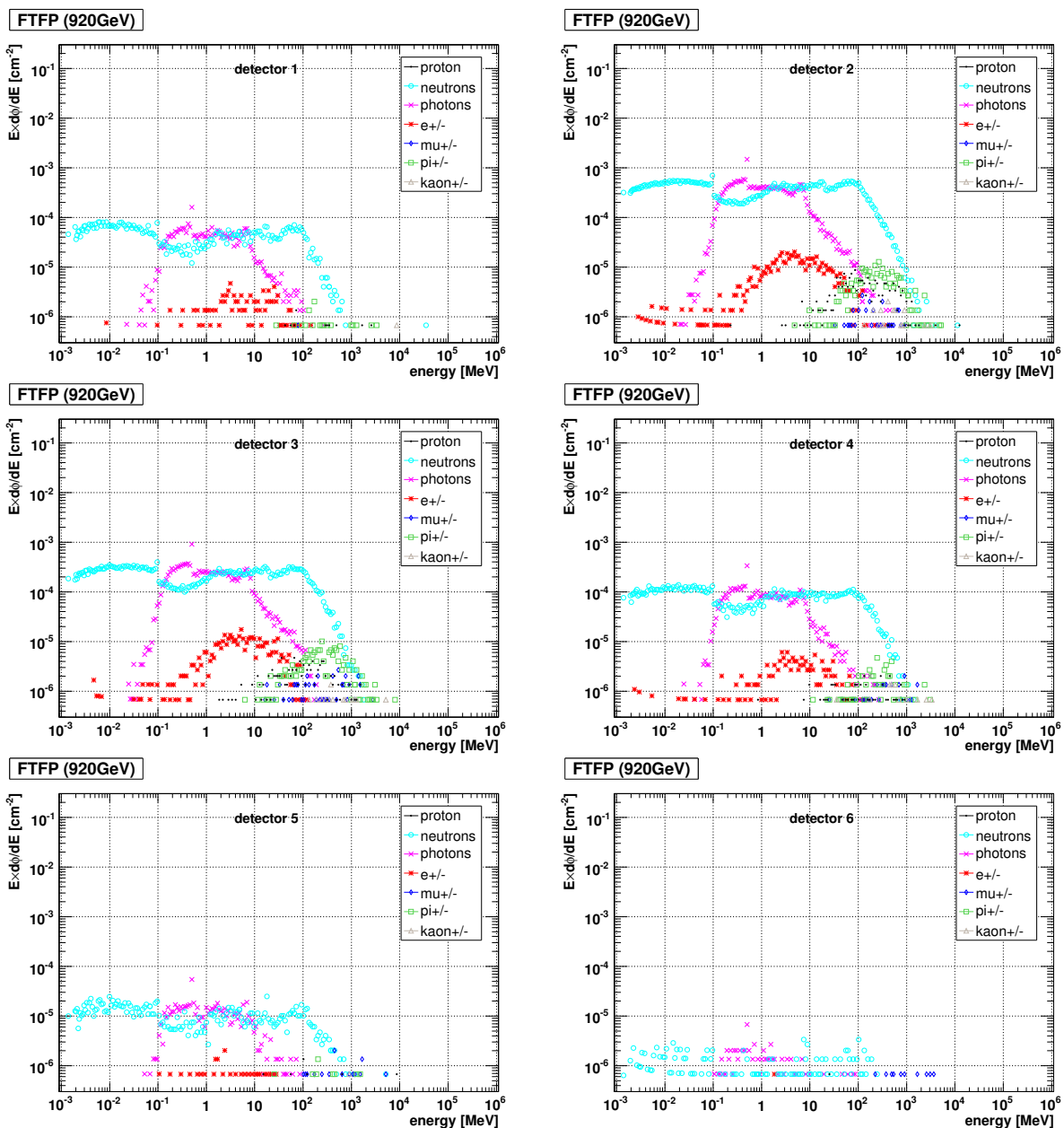


Figure A.6: The fluence spectra [particles/cm²/primary/Lethargy] at different detector positions for 920 GeV proton energy was simulated with the physics list FTFP (Geant4).

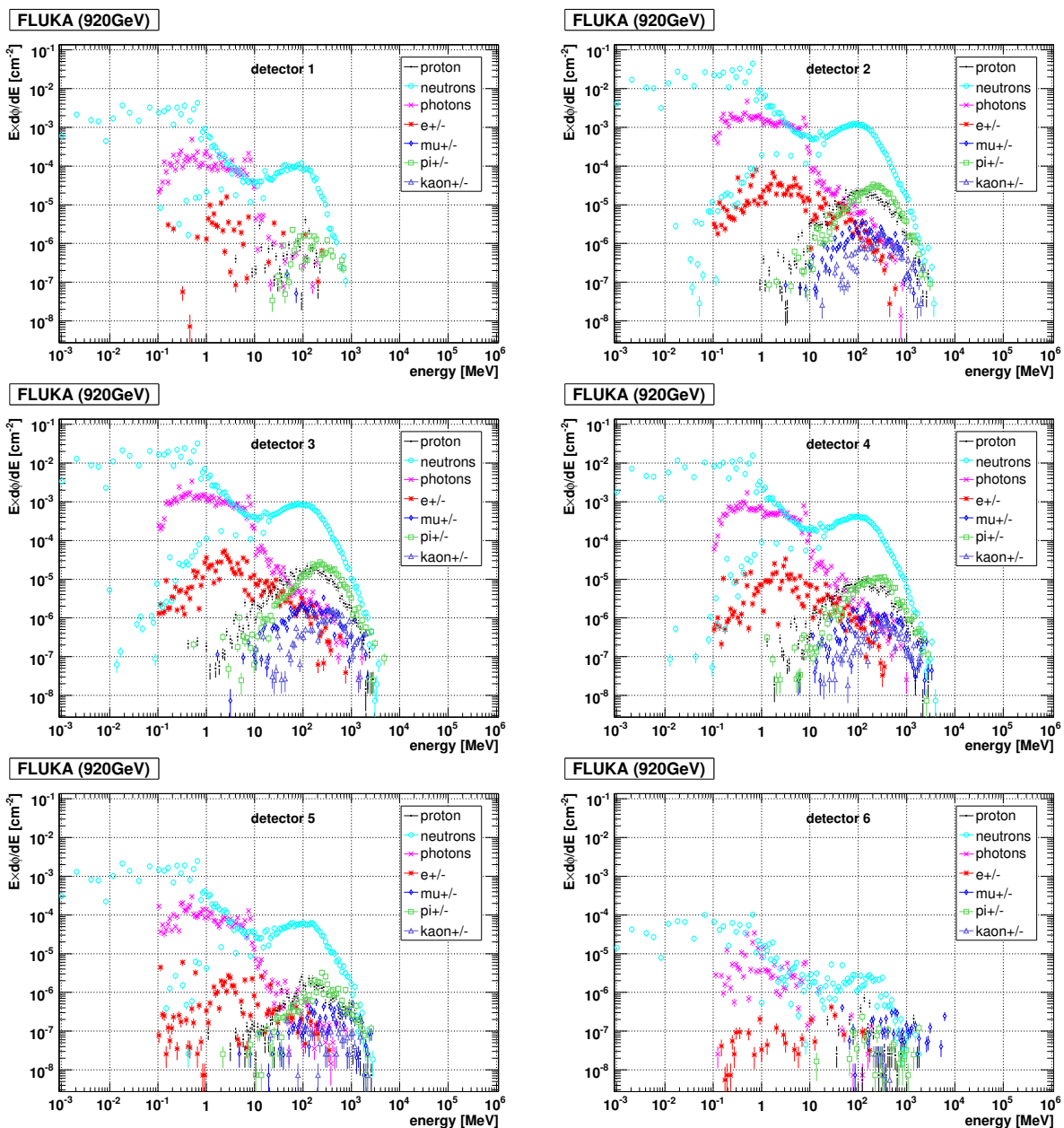


Figure A.7: The fluence spectra [particles/cm²/primary/Lethargy] at different detector positions for 920 GeV proton energy was simulated with FLUKA (courtesy of R. Bruce).

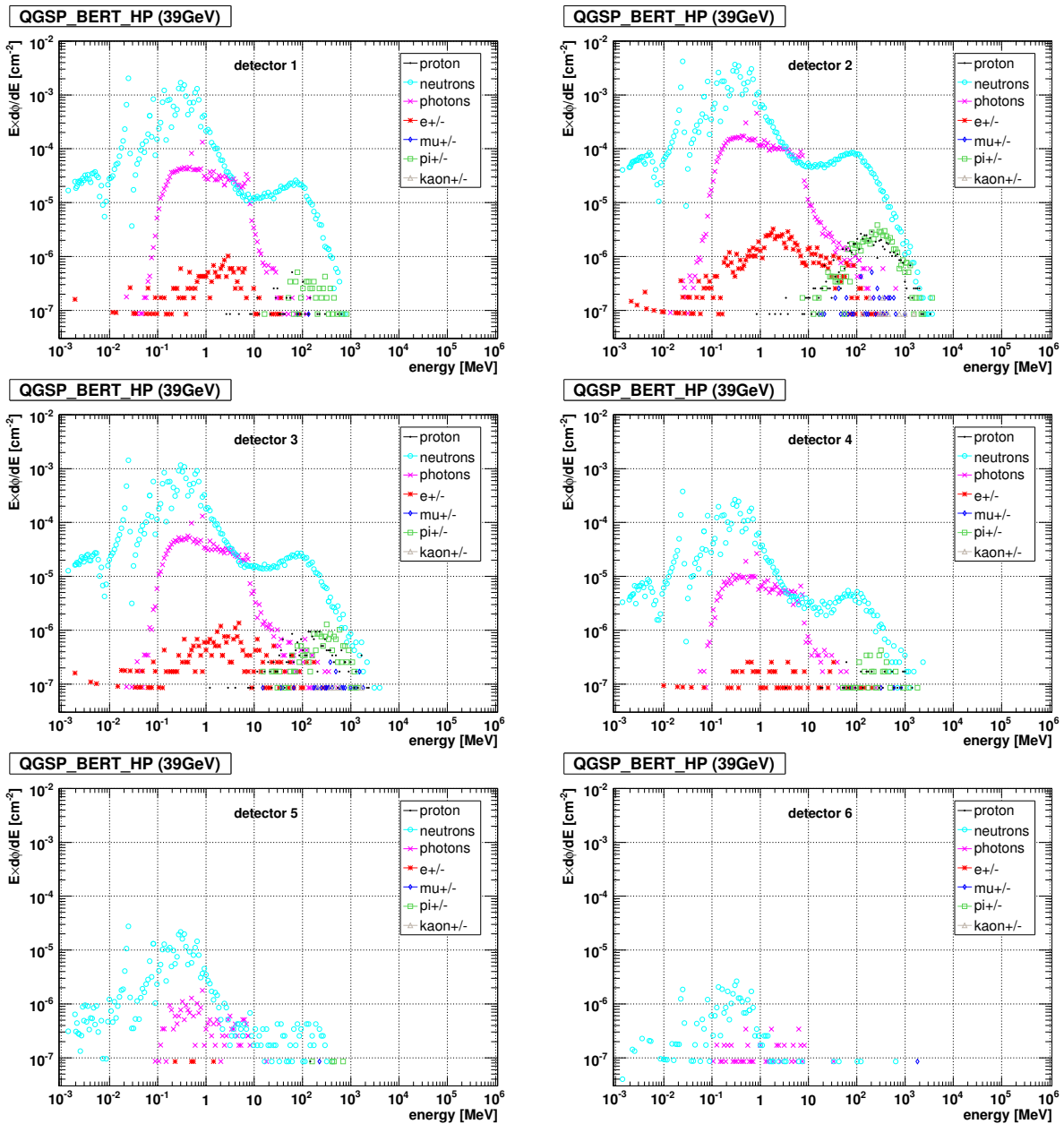


Figure A.8: The fluence spectra [particles/cm²/primary/Lethargy] at different detector positions was simulated with the physics list QGSP-BERT-HP (Geant4) at a beam energy of 39 GeV.

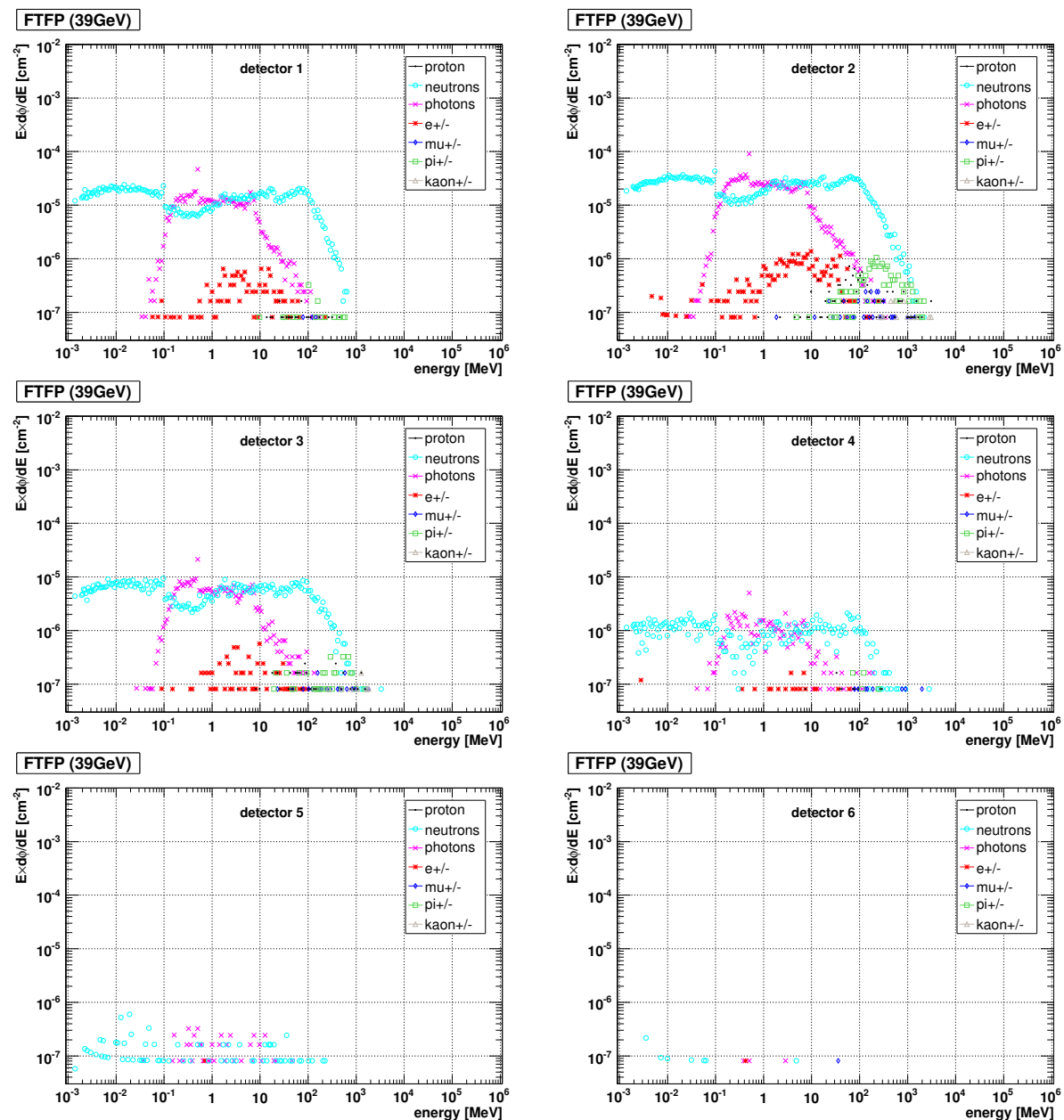


Figure A.9: The fluence spectra [particles/cm²/primary/Lethargy] at different detector positions was simulated with the physics list FTFP (Geant4) at a beam energy of 39 GeV.

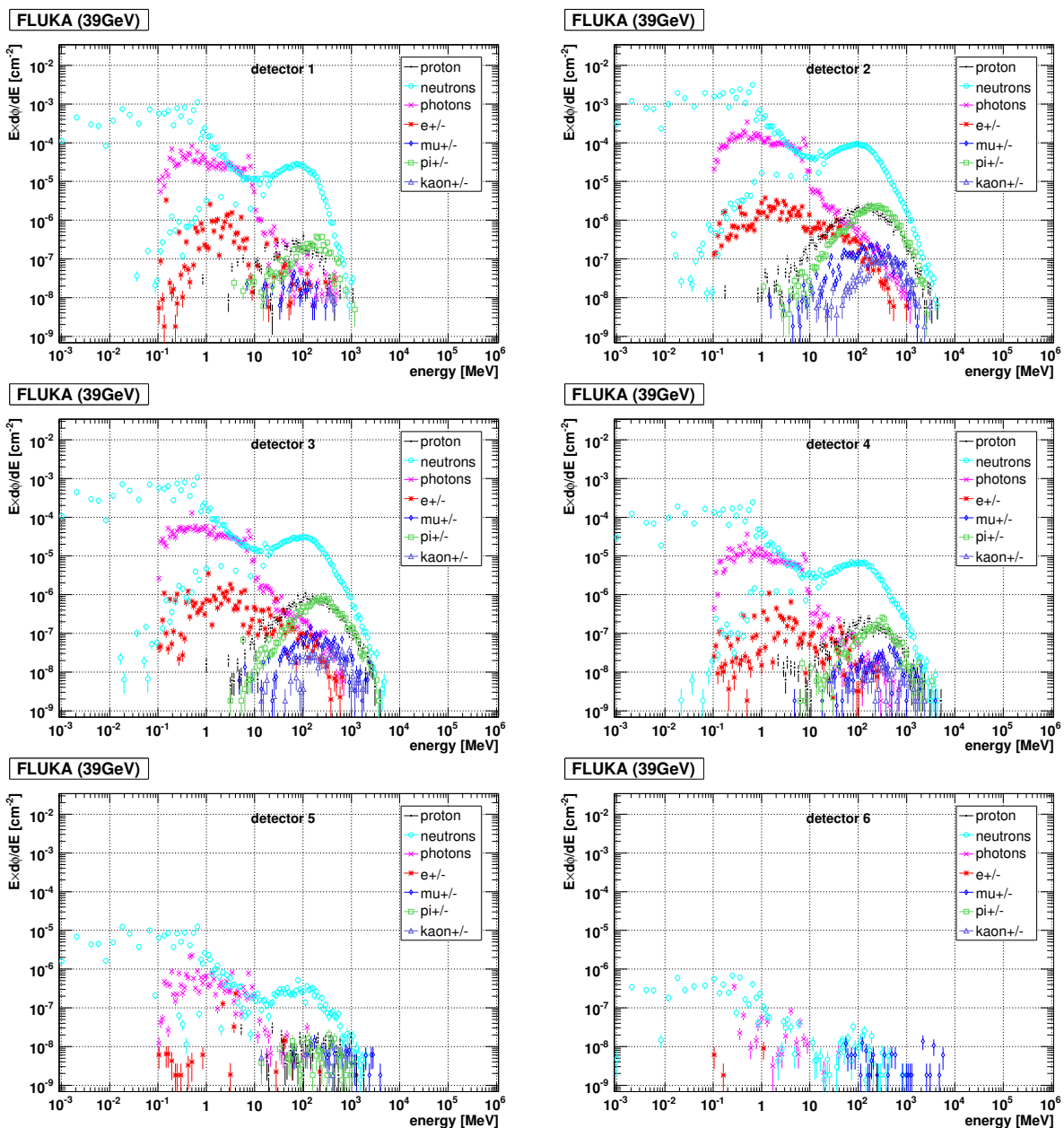


Figure A.10: The Fluence spectra [particles/cm²/primary/Lethargy] at different detector positions was simulated with FLUKA at a beam energy of 39 GeV (courtesy of R. Bruce).

Appendix B

Statistics and the Treatment of Experimental Data

Random processes are described by a probability density function, which gives the expected frequency of occurrence for each possible outcome of such a processes. More formally, the outcome of a random process is represented by a random variable x , which ranges over all admissible values in the process. Depending on the process, a random variable may be continuous or discrete. In the first case, it may take on a continuous range of values, while in the second only a finite number of values is allowed. If x is discrete, the frequency at each point is then given by $P(x_i)$. If x is continuous, this interpretation is not possible and only probabilities of finding x in finite intervals have meaning. The probability of finding x between the interval x and $x + dx$ is then $P(x)dx$, where the distribution $P(x)$ is a continuous density [28].

B.1 Distribution Moments. The Mean and Variance

A probability distribution may be characterised by its moments. In practice, only the first two moments are of importance.

The most important is the first moment about zero, which is defined as,

$$\mu = E[x] = \int xP(x)dx. \quad (\text{B.1})$$

This can be recognised as simply the mean or average of x . It is very important here to distinguish the mean as defined in (B.1) from the mean which one calculates from a set of repeated measurements. The first refers to the theoretical mean, as calculated from the theoretical distribution, while the latter is an experimental mean taken from a sample.

The second characteristic quantity is the second moment about the mean,

$$\sigma^2 = E[(x - \mu)^2] = \int (x - \mu)^2 P(x)dx. \quad (\text{B.2})$$

σ^2 is commonly called the variance. The square root of the variance is known as the standard

deviation. The standard deviation, σ , measures the dispersion or width of the distribution and gives an idea of how much the random variable x fluctuates about its mean. The theoretical variance should also be distinguished from the sample variance.

B.2 Measurement Errors: Systematic and Random Errors

Any kind of measurement, in any experiment, is afflicted with uncertainties or errors, as they are more often called. A measurement process is, in fact, a random process described by an abstract probability distribution whose parameters contain the desired information. The results of a measurement are then a sample from this distribution, which allow an estimate of the theoretical parameters. So measurement errors can be seen as sampling errors.

It has to be distinguished between two types of error: systematic and random.

B.2.1 Systematic Errors

Systematic errors are uncertainties in the bias of the data. An important point to be clear about is that a systematic error implies that all measurements in a set of data taken with the same instrument have an uncertainty in the same direction by the same amount. This is in contrast to random errors where each individual measurement fluctuates independently of the others. There is no “standard“ method for treating or analysing systematic errors. Each experiment must be considered individually and it is often very difficult just to identify the possible sources and to estimate the magnitude of the error.

B.2.2 Random Error

Random errors are in contrast to systematic errors. They may be handled by the theory of statistics. These uncertainties may arise from instrumental imprecision, and/or, from the inherent statistical nature of the phenomena being observed. Statistically, both are treated in the same manner as uncertainties arising from the finite sampling of an infinite population of events. The measurement process, as suggested, is a sampling process. The true parameters of a population or distribution too large to measure in its entirety are estimated by the sample parameters of a taken random sample of finite size. Since the sample is finite, there is an uncertainty on the estimate and this represents the measurement error.

The measurement of a fixed quantity, involves taking a sample from an abstract, theoretical distribution determined by the imprecision of the instrument. In almost all cases of instrumental errors the distribution is Gaussian. Assuming no systematic error, the mean of the Gaussian should then be equal to the true value of the quantity being measured and the standard deviation proportional to the precision of the instrument.

B.3 Sampling

To obtain information about the parameters of an unknown distribution the experimental method of sampling is used. There by the best value, which minimises the variance between the estimate and the true value is determined. In statistics, this is known as estimation.

B.3.1 Sample Moments

Let $x_1, x_2, x_3, \dots, x_n$ be a sample of size n from an distribution whose theoretical mean is μ and variance σ^2 . This is known as the sample population. The sample mean, \bar{x} , is then defined as

$$\bar{x} = \frac{1}{n} \sum_{i=1}^n x_i, \quad (\text{B.3})$$

which is just the arithmetic average of the sample. In the limit $n \rightarrow \infty$, this can be shown to approach the theoretical mean,

$$\mu = \lim_{n \rightarrow \infty} \frac{1}{n} \sum_{i=1}^n x_i. \quad (\text{B.4})$$

Similarly, the sample variance, which we denote by s^2 is

$$s^2 = \frac{1}{n} \sum_{i=1}^n (x_i - \bar{x})^2, \quad (\text{B.5})$$

which is the average of the squared deviations. In the limit $n \rightarrow \infty$, this also approaches the theoretical variance σ^2 .

From deriving the estimator of the Poisson distribution with the maximum likelihood method it can be found that,

$$\hat{\mu} = \frac{1}{n} \sum x_i = \bar{x}, \quad (\text{B.6})$$

what is of course just the sample mean. But this confirms the often unconscious use of (B.6).

A really general result can be derived without referencing to the Poisson distribution by this method that is,

$$\sigma^2(\bar{x}) = \frac{\sigma^2}{n}, \quad (\text{B.7})$$

the variance of the sample mean is given by the variance of the parent distribution, whatever it may be, divided by the sample size.

For the Gaussian distribution also (B.6) and (B.7) can be found. The square root of equation (B.7) is usually, in this context, referred to as the standard error of the mean. For a measurement device, σ thus represents the precision of the instrument. The estimator for σ^2 of a Gaussian distribution is then,

$$\hat{\sigma}^2 = \frac{1}{n} \sum (x_i - \mu)^2 \simeq \frac{1}{n} \sum (x_i - \bar{x})^2 = s^2, \quad (\text{B.8})$$

where μ is replaced by (B.6). This is the sample variance.

For finite values of n , the sample variance turns out to be a biased estimator, that is the expectation value of s^2 does not equal the true value, but is offset from it by a constant factor.

For principal use the recommended formula for estimating the variance (unbiased) is,

$$\hat{\sigma}^2 = \frac{\sum (x_i - \bar{x})^2}{n - 1}, \quad (\text{B.9})$$

what provides a good estimate.

The standard deviation of $\hat{\sigma}$ is,

$$\sigma(\hat{\sigma}) = \frac{\sigma}{\sqrt{2(n-1)}} \simeq \frac{\hat{\sigma}}{\sqrt{2(n-1)}}. \quad (\text{B.10})$$

Appendix C

LHC BLM Detector Layout

Appendix D

SPS BLM Detector Layout

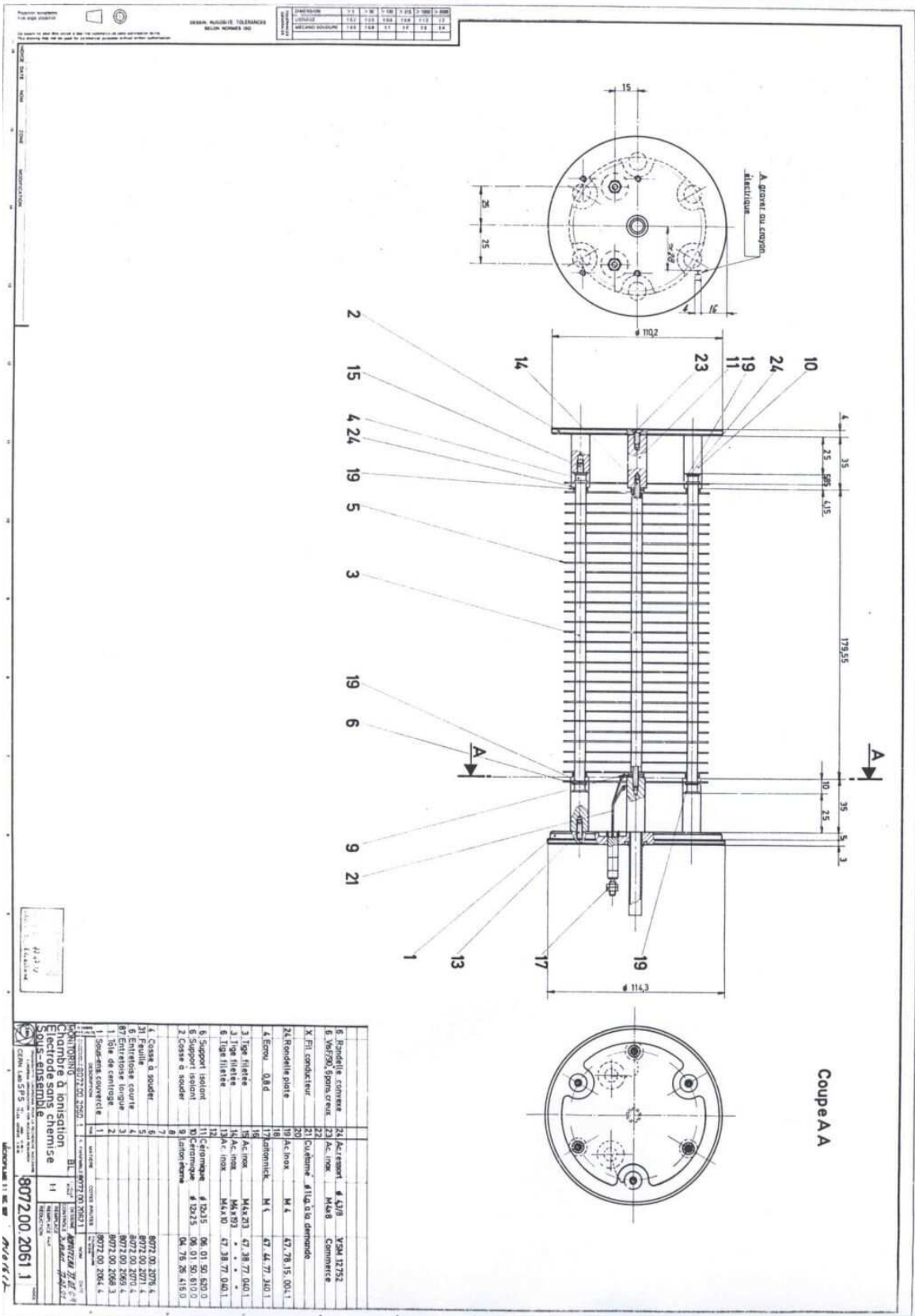


Figure D.1: SPS BLM detector layout.